Author contributions:
Amit Jairaman: Conceptualization; Formal analysis; Validation; Investigation; Visualization; Methodology; Writing - original draft; Writing - review and editing Amanda McQuade: Conceptualization; Formal analysis; Funding acquisition; Validation; Investigation; Visualization; Methodology; Writing - original draft; Writing - review and editing Alberto Granzotto: Formal analysis; Investigation; Methodology; Writing - review and editing You Kang: Formal analysis; Investigation; Methodology; Writing - review and editing Jean Chadarevian: Investigation; Methodology Sunil Gandhi: Resources; Supervision; Funding acquisition; Writing - review and editing Ian Parker: Resources; Methodology; Writing - review and editing Ian Smith: Formal analysis; Investigation; Writing - review and editing Hansang Cho: Resources; Formal analysis; Supervision; Funding acquisition; Investigation; Methodology; Writing - review and editing Stefano Sensi: Resources; Supervision; Funding acquisition; Methodology Shivashankar Othy: Conceptualization; Resources; Formal analysis; Supervision; Funding acquisition; Investigation; Methodology; Writing - original draft; Project administration; Writing - review and editing Mathew Blurton-Jones: Conceptualization; Resources; Supervision; Funding acquisition; Investigation; Methodology; Writing - original draft; Project administration; Writing - review and editing Michael Cahalan: Conceptualization; Resources; Supervision; Funding acquisition; Methodology; Writing - original draft; Project administration; Writing - review and editing

Funding:
HHS | National Institutes of Health (NIH): Michael D Cahalan, R01 NS14609; HHS | National Institutes of Health (NIH): Michael D Cahalan, R01 AI121945; HHS | National Institutes of Health (NIH): Mathew Blurton-Jones, R01 AG048099; HHS | National Institutes of Health (NIH): Mathew Blurton-Jones, R01 AG056303; HHS | National Institutes of Health (NIH): Mathew Blurton-Jones, R01 AG055524; HHS | National Institutes of Health (NIH): Mathew Blurton-Jones, core AG066519; HHS | National Institutes of Health (NIH): Shivashankar Othy, U01 AI160397; HHS | National Institutes of Health (NIH): Amanda McQuade, T32 NS082174; HHS | National Institutes of Health (NIH): Sunil Gandhi, RF1DA048813 The funders had no role in study design, data collection and interpretation, or the decision to submit the work for publication.

Data Availability:
RNA sequencing data referenced in Figure 1- figure supplement 2 is available through Gene Expression Omnibus: GSE157652.
N/A

Ethics:
Human Subjects: Yes Ethics Statement: Human iPSC lines were generated by the University of California Alzheimer's Disease Research Center (UCI ADRC) stem cell core. Subject fibroblasts were collected under approved Institutional Review Boards (IRB) and human Stem Cell Research Oversight (hSCRO) committee protocols. Informed consent was received for all participants. Clinical Trial: No Animal Subjects: No

TREM2 regulates purinergic receptor-mediated calcium signaling and motility in human iPSC-derived microglia

Amit Jairaman[1]†, Amanda McQuade[2,3,4]†, Alberto Granzotto[2,5,6], You Jung Kang[7], Jean Paul Chadarevian[2], Sunil Gandhi[2], Ian Parker[1,2], Ian Smith[2], Hansang Cho[8], Stefano L. Sensi[5,6], Shivashankar Othy[1,9], Mathew Blurton-Jones[2,3,4,9]*, Michael Cahalan[1,9]*

Affiliations:

[1] Department of Physiology & Biophysics, University of California, Irvine, CA 92697-4561, USA

[2] Department of Neurobiology & Behavior, University of California, Irvine, CA 92697, USA

[3] Sue and Bill Gross Stem Cell Research Center, University of California, Irvine, CA 92697, USA

[4] UCI Institute for Memory Impairments and Neurological Disorders, University of California, Irvine, CA 92697, USA

[5] Center for Advanced Sciences and Technology (CAST), University "G. d'Annunzio" of Chieti-Pescara, Chieti 66100, Italy

[6] Department of Neuroscience, Imaging, and Clinical Sciences (DNISC), University "G. d'Annunzio" of Chieti-Pescara, Chieti 66100, Italy

[7] Department of Mechanical Engineering and Engineering Science, Center for Biomedical Engineering and Science, University of North Carolina, Charlotte, NC 28223, USA

[8] Institute of Quantum Biophysics, Department of Biophysics, Sungkyunkwan University, 2066 Seobu-ro, Jangan-gu, Suwon-si, Gyeonggi-do 16419, Korea

[9] Institute for Immunology, University of California, Irvine, CA 92697, USA

† Equal contributions

* Co-corresponding authors: Michael D. Cahalan (mcahalan@uci.edu), Mathew Blurton-Jones (mblurton@uci.edu)

Key Words: microglia, motility, Alzheimer's disease, P2Y receptor, Ca^{2+} signaling, store-operated Ca^{2+} entry (SOCE), genetically encoded Ca^{2+} indicator, TREM2

Abstract

The membrane protein TREM2 (Triggering Receptor Expressed on Myeloid cells 2) regulates key microglial functions including phagocytosis and chemotaxis. Loss-of-function variants of TREM2 are associated with increased risk of Alzheimer's disease (AD). Because abnormalities in Ca^{2+} signaling have been observed in several AD models, we investigated TREM2 regulation of Ca^{2+} signaling in human induced pluripotent stem cell-derived microglia (iPSC-microglia) with genetic deletion of TREM2. We found that iPSC-microglia lacking TREM2 (TREM2 KO) show exaggerated Ca^{2+} signals in response to purinergic agonists, such as ADP, that shape microglial injury responses. This ADP hypersensitivity, driven by increased expression of $P2Y_{12}$ and $P2Y_{13}$ receptors, results in greater release of Ca^{2+} from the endoplasmic reticulum (ER) stores, which triggers sustained Ca^{2+} influx through Orai channels and alters cell motility in TREM2 KO microglia. Using iPSC-microglia expressing the genetically encoded Ca^{2+} probe, Salsa6f, we found that cytosolic Ca^{2+} tunes motility to a greater extent in TREM2 KO microglia. Despite showing greater overall displacement, TREM2 KO microglia exhibit reduced directional chemotaxis along ADP gradients. Accordingly, the chemotactic defect in TREM2 KO microglia was rescued by reducing cytosolic Ca^{2+} using a $P2Y_{12}$ receptor antagonist. Our results show that loss of TREM2 confers a defect in microglial Ca^{2+} response to purinergic signals, suggesting a window of Ca^{2+} signaling for optimal microglial motility.

Main Text

Introduction

As the primary immune cells of the central nervous system, microglia survey their local environment to maintain homeostasis and respond to local brain injury or abnormal neuronal activity. Microglia are strongly implicated in several neurodevelopmental and neurodegenerative diseases[1–7], warranting further study of human microglial dynamics. Purinergic metabolites (ATP, ADP, UTP, UDP) in the brain constitute key signals driving microglial activation and chemotaxis, and are detected by microglial cells over concentrations ranging from hundreds of nM to μM [8–13]. ATP released from both homeostatic and damaged cells is hydrolyzed locally by nucleosidases such as the ectonucleotidase NTPDase1 (CD39) or pyrophosphatase NPP1 to produce ADP[14–16]. ADP is then detected by P2Y purinergic receptors on microglia, causing IP_3-dependent Ca^{2+} release from the endoplasmic reticulum (ER) lumen. Ca^{2+} depletion from the ER in turn activates ER STIM1 proteins to translocate proximally to puncta where closely apposed plasma membrane (PM) Orai1 channels are activated. This mechanism underlies store-operated Ca^{2+} entry (SOCE) in many cell types [17], including microglia[18–20].

Purinergic signaling is central to microglial communication with other brain cell types and has been negatively correlated with the onset of Disease-Associated Microglia (DAM) transcriptional states [21–25]. $P2Y_{12}$ and $P2Y_{13}$ receptors are highly expressed by microglia and are activated predominantly by ADP [16,26]. $P2Y_{12}$ receptors are essential for microglial chemotaxis and have been implicated in the microglial response to cortical injury[12,27], NLRP3 inflammasome activation[28,29], neuronal hyperactivity and protection[27,30], and blood brain barrier

maintenance[31,32]. While purinergic receptors have been broadly identified as markers of microglial homeostasis[23,26], mechanisms by which receptor expression may drive or maintain homeostatic microglial states remain incompletely understood.

Neuroinflammatory pathologies are often associated with altered Ca^{2+} signaling[33]. Microglia, in particular, show altered Ca^{2+} responses in mouse models of Alzheimer's Disease (AD) by mechanisms that are not fully understood[34–36]. Ca^{2+} responses to purinergic metabolites have been extensively studied in cultured murine microglia, acute brain slices, and more recently in anesthetized mice [8,10,34,37–39]. However, our understanding of how specific patterns of Ca^{2+} signals in microglia correlate with and tune downstream microglial responses such as cell motility or process extension remains incomplete. There is also a paucity of knowledge on how regulators of purinergic Ca^{2+} signals in microglia might play a role in the dysregulation of Ca^{2+} signaling associated with aging and neuroinflammation.

TREM2 encodes a cell surface receptor that binds a variety of ligands including various lipids, apolipoprotein E (ApoE), and amyloid-β peptides. Upon ligand binding, TREM2 signals through its adaptor protein DAP12 to activate a host of downstream pathways[23,40–42]. Loss of TREM2 function is thought to promote a more homeostatic-like state[23,43,44]. Indeed, microglia lacking TREM2 expression exhibit greatly diminished activation against disease pathology, correlating with increased risk of AD[23,41,45]. Purinergic receptor hyperexpression has been reported at the transcriptome level across multiple TREM2 loss of function models including human patient mutations [21–23,25,41,46]. For example, $P2Y_{12}$ receptor protein expression was found to be elevated in the cortical microglia of *Trem2*$^{-/-}$ mice and in a preclinical mouse model of

AD[47,48], although the mechanistic link between purinergic receptor expression and TREM2 function remains poorly understood.

We previously developed methods to generate human induced pluripotent stem cell-derived microglia (iPSC-microglia)[49–51], which can be used to model human microglial behavior. While iPSC-microglia are proving increasingly useful to investigate neurodegenerative disorders[41,52–56], Ca^{2+} signaling has not yet been extensively profiled in these models. In this study, we compared purinergic Ca^{2+} signaling and motility characteristics in WT and TREM2 KO human iPSC-microglia, and examined the mechanisms that underlie enhanced purinergic Ca^{2+} signaling in microglia lacking TREM2. We find that motility is differentially tuned by Ca^{2+} in TREM2 KO cells with consequences for chemotaxis.

Results

Purinergic receptor Ca^{2+} signaling is enhanced in TREM2-knockout human iPSC-microglia

To determine if TREM2 plays a role in microglial Ca^{2+} signaling, we compared cytosolic Ca^{2+} responses to the purinergic agonist ADP in isogenic, CRISPR-modified wild type (WT) and TREM2-knockout (TREM2 KO) human iPSC-microglia. ADP stimulation induced a biphasic Ca^{2+} response – a rapid initial peak followed by a secondary phase of sustained Ca^{2+} elevation lasting several minutes, in line with previous observations in mouse microglia [57,58]. Both phases of the Ca^{2+} response were significantly elevated in TREM2 KO microglia, raising the possibility that augmentation of the initial Ca^{2+} response to ADP in TREM2 KO microglia may be coupled to a larger sustained component of Ca^{2+} entry (**Figure 1A, B**). These results were corroborated in iPSC-derived microglia cell line expressing the genetically-encoded Ca^{2+} indicator Salsa6f[59,60] (**Figure 1C, D**). The Salsa6f probe showed the expected increase in the GCaMP6f fluorescence in response to Ca^{2+} elevation without any change in the tdTomato signal, and it did not perturb microglial activation and function (**Figure 1-figure supplement 1A-G**). TREM2 KO microglia also showed exaggerated Ca^{2+} responses to the purinergic agonists ATP and UTP at similar low μM concentrations, although the secondary Ca^{2+} elevations were not as long-lasting as with ADP (**Figure 1E, F and Figure 1-figure supplement 2**).

Increased $P2Y_{12}$ and $P2Y_{13}$ receptor expression drives increased peak Ca^{2+} in TREM2-KO microglia

Given the critical importance of ADP signaling in several aspects of microglial function, we investigated the mechanisms driving higher ADP-evoked Ca^{2+} signals in TREM2 KO microglia by

focusing on specific steps in the purinergic Ca^{2+} signaling pathway (**Figure 2A**). The initial Ca^{2+} response to P2Y receptor engagement results from G protein-coupled phospholipase C activation, and IP_3-mediated ER Ca^{2+} store-release. To test this, we treated cells with ADP in Ca^{2+}-free solution buffered with the Ca^{2+} chelator EGTA to isolate Ca^{2+} signals from store-release and eliminate Ca^{2+} influx across the PM. Both WT and TREM2 KO cells exhibited a single Ca^{2+} peak, with TREM2 KO cells showing significantly higher peak Ca^{2+} response to ADP (**Figure 2B and Figure 2-figure supplement 1A, B**). Moreover, the amplitude of the Ca^{2+} peak was not significantly different in the presence or absence of external Ca^{2+}, strongly suggesting that it is driven primarily by release of Ca^{2+} from intracellular stores even when external Ca^{2+} is present (**Figure 2-figure supplement 1C**). Dose-response curves for the peak Ca^{2+} response showed a steep leftward shift in TREM2 KO cells (**Figure 2C**). The EC_{50} value for WT microglia was 650 nM, whereas TREM2 KO microglia reached their EC_{50} by 15 nM. This stark difference was driven at least in part by a diminished percentage of WT cells responding to ADP at low μM doses (**Figure 2D**). However, limiting the analysis to cells that showed a Ca^{2+} rise revealed that "responding" TREM2 KO cells still exhibited higher Ca^{2+} responses to ADP than "responding" WT cells (**Figure 2E**). TREM2 KO microglia are thus significantly more sensitive to ADP than WT cells which may be critical in sensing ADP and in detecting ADP gradients.

RNA-sequencing revealed significantly increased transcripts for $P2Y_{12}$ and $P2Y_{13}$ receptors, the main P2Y receptor subtypes in microglia that bind ADP, in TREM2 KO microglia[49,50] (**Figure 2F**). In comparison, relative mRNA levels of common mediators of Ca^{2+} signaling – including predominant isoforms of IP_3 receptors, SOCE mediators Orai and STIM proteins, and SERCA and PMCA Ca^{2+} pumps – were either similar or modestly reduced in TREM2

KO in comparison with WT iPSC-microglia (**Figure 2-figure supplement 1D, E**). We therefore considered the possibility that signal amplification in microglia lacking TREM2 results primarily from increased expression of $P2Y_{12}$ and $P2Y_{13}$ receptors. Consistent with this, expression of $P2Y_{12}$ receptors in the plasma membrane was significantly increased in TREM2 KO cells (**Figure 2G**). Furthermore, Ca^{2+} responses to ADP in Ca^{2+}-free medium were completely abolished following treatment with a combination of $P2Y_{12}$ and $P2Y_{13}$ receptor antagonists (PSB 0739 and MRS 2211 respectively) in both WT and TREM2 KO microglia (**Figure 2H**). Treatment of cells with $P2Y_{12}$ and $P2Y_{13}$ receptor antagonists separately produced partial inhibition of peak ADP-mediated Ca^{2+} signals, implicating involvement of both receptor subtypes (**Figure 2-figure supplement 1F, G**). In summary, deletion of TREM2 results in a larger cytosolic Ca^{2+} peak in response to ADP due to increased expression of $P2Y_{12}$ and $P2Y_{13}$ receptors.

SOCE through Orai channels mediates the sustained phase of ADP-evoked Ca^{2+} elevation

To probe the basis for the increased sustained component of ADP-evoked Ca^{2+} signal in TREM2 KO microglia, we examined SOCE using pharmacological and genetic approaches. Synta66, a reasonably specific inhibitor of Orai channels, significantly reduced the rate of SOCE following Ca^{2+} re-addition after ER store-depletion by the sarco-endoplasmic reticulum Ca^{2+} ATPase (SERCA pump) inhibitor, thapsigargin (TG) in both WT and TREM2 KO microglia (**Figure 3A and Figure 3-figure supplement 1A**). Using a similar Ca^{2+} re-addition protocol with ADP, we found significant inhibition of ADP-induced SOCE by Synta66 in both WT and TREM2 KO cells (**Figure 3B and Figure 3-figure supplement 1B**). The ADP-evoked sustained Ca^{2+} phase in TREM2 KO iPSC-microglia was also blocked by less specific Orai channel inhibitors, Gd^{3+} and 2-APB (**Figure**

3-figure supplement 1C, D). To further confirm the specific role of Orai1 channels in mediating SOCE, we generated an Orai1 CRISPR-knockout iPSC line. Deletion of Orai1 abrogated SOCE and significantly reduced the sustained Ca^{2+} response to ADP (**Figure 3-figure supplement 1E, F**). These results confirm that Orai1 plays an important role in mediating SOCE and ADP-evoked Ca^{2+} signals in iPSC-microglia.

To determine if SOCE is increased in TREM2 KO microglia and contributing to the higher sustained Ca^{2+} response to ADP, we compared the rate of store-operated Ca^{2+} influx after store-depletion with TG, and found that both the rate and amplitude of SOCE were modestly reduced in TREM2 KO cells (**Figure 3C**). In keeping with this, RNA sequencing revealed a modest reduction in STIM1 mRNA expression in TREM2 KO cells, although Orai1 mRNA was similar in WT and TREM2 KO microglia (**Figure 2-figure supplement 1C, D**). We further conclude that the elevated secondary phase of ADP-driven Ca^{2+} signals in TREM2 KO microglia is not primarily due to differences in the expression of STIM and Orai.

ADP depletes ER Ca^{2+} stores to a greater extent in TREM2 KO microglia leading to greater SOCE activation

We hypothesized that the exaggerated secondary Ca^{2+} phase in response to ADP in TREM2 KO microglia may be driven by increased ER Ca^{2+} store-release leading to greater SOCE activation. Consistent with this possibility, peak cytosolic Ca^{2+} in response to partial store-depletion with ADP, and after Ca^{2+} re-addition was elevated in TREM2 KO microglia (**Figure 3D**). To examine if the higher magnitude of SOCE in TREM2 KO cells is due to depletion of ER Ca^{2+} stores by ADP, we sequentially treated cells with ADP followed by ionomycin to completely release stores in

Ca^{2+} free buffer. While TREM2 KO cells showed greater peak Ca^{2+} with ADP as expected, the ionomycin Ca^{2+} peak – which reflects the residual ER Ca^{2+} pool – was significantly reduced indicating that ADP depletes ER Ca^{2+} stores to a greater extent in TREM2 KO cells (**Figure 3E**). Similar results were obtained when residual ER store-content was depleted using TG instead of ionomycin (**Figure3- figure supplement 2A, B**). We plotted cytosolic Ca^{2+} levels 5 minutes after addition of varying doses of ADP to indicate the degree of SOCE, as a function of the initial peak Ca^{2+}, a readout of ER store-release (**Figure 3- figure supplement 2C, D**). Both WT and TREM2 KO microglia showed similar linear relationships between SOCE and store-release, further suggesting that SOCE is activated by similar mechanisms in the two cell lines, but is recruited to a greater extent in TREM2 KO cells due to increased ER store-release. We also note that increased sustained Ca^{2+} in TREM2 KO cells is unlikely to be due to differences in Ca^{2+} pump activity based on similar Ca^{2+} clearance rates (**Figure 3- figure supplement 2E, F**), consistent with comparable transcriptomic expression of major SERCA and plasma membrane Ca^{2+} ATPase (PMCA) isoforms in WT and TREM2 KO cells (**Figure 2- figure supplement 1C, D**).

Finally, quantification of cumulative cytosolic Ca^{2+} increases after maximally depleting ER stores with ionomycin alone suggested that overall ER store-content is not altered in microglia lacking TREM2 (**Figure 3F**). Comparison of Ca^{2+} responses to IP_3 uncaging also ruled out major differences in the pool of functional IP_3 receptors between WT and TREM2 KO cells (**Figure 3G**), as further substantiated by similar transcriptomic expression of IP_3 receptor type 2 (the major IP_3R subtype expressed in iPSC-microglia) in WT and TREM2 KO cells (**Figure 2-figure supplement 1C, D**)[41,49]. In summary, deletion of TREM2 in iPSC-derived microglia leads to upregulation of $P2Y_{12}$ and $P2Y_{13}$ receptors and renders the cells hypersensitive to ADP signaling,

consequently leading to greater IP_3-mediated ER store-depletion and increased coupling to SOCE in response to purinergic metabolites.

ADP potentiates cell motility and process extension in human WT iPSC-microglia

ADP is a potent chemoattractant for microglia[10]. Analogous to a previous study in fibroblasts[61], we found that ADP treatment alters cell motility and leads to increased rates of scratch wound closure in WT iPSC-microglia (**Figure 4A**). To investigate the cellular mechanism of accelerated wound closure, we used time-lapse imaging to track open-field microglial cell motility (**Figure 4B**). Mean cell track speed and track displacement (defined as the overall change in position from the origin at a given time) were both increased after application of ADP. On the other hand, average track straightness, an indicator of how frequently cells change direction, was unaltered by ADP (**Figure 4C**). These data suggest that ADP-driven changes in motility in WT iPSC-microglia primarily arise from increases in microglial speed, and not altered turning behavior. ADP-dependent increases in speed were reversed in the presence of $P2Y_{12}$ (PSB 0739) and $P2Y_{13}$ (MRS 2211) receptor antagonists, confirming the role of these two purinergic receptors in ADP enhancement of microglial motility (**Figure 4D**). To determine if Ca^{2+} influx regulates ADP-mediated increases in motility, we measured cell migration with ADP in Ca^{2+}-free medium and found that removing extracellular Ca^{2+} significantly decreased cell speed, displacement, and track straightness, suggesting that sustained Ca^{2+} signals are required for maximal increase in motility in response to ADP (**Figure 4E**).

In addition, some microglia responded to ADP by extending processes and altering their morphology rather than increasing motility (**Figure 4-figure supplement 1**). Microglia have

been observed to extend processes in response to injury and purinergic stimulation in brain slices[8,12]. Therefore, we compared process complexity before and 30 min after ADP exposure in WT microglia and observed significant increases in both the number of branches per process and total length of these processes (**Figure 4F**). Similar to effects on cell motility, ADP-mediated process extension was inhibited by $P2Y_{12}$ and $P2Y_{13}$ receptor antagonists (PSB 0739 and MRS 2211 respectively). Furthermore, even before process extension was activated with ADP, cells treated with P2Y antagonists showed significantly fewer and shorter processes, suggesting that baseline purinergic signaling may regulate resting microglial process dynamics. Altogether, these results demonstrate that activation of purinergic signaling through $P2Y_{12}$ and $P2Y_{13}$ receptors is required for ADP-driven microglial process extension and motility.

ADP-evoked changes in cell motility and process extension are enhanced in TREM2-KO microglia

To characterize differences in motility characteristics between WT and TREM2 KO microglia responding to ADP, we plotted mean squared displacement (MSD) vs time and compared cell track overlays (flower plots) which showed that ADP enhances motility in TREM2 KO cells to a greater extent than in WT microglia (**Figure 5A, B**). Baseline motility characteristics in unstimulated cells, however, were similar in WT and TREM2 KO cells (**Figure 5-figure supplement 1A, B**). To further understand the basis of differences in ADP-induced motility between WT and TREM2 KO cells, we analyzed mean track speed, track displacement, and track straightness. Although mean track speeds were similar, TREM2 KO microglia showed greater displacement than WT cells (**Figure 5C, D**), raising the possibility that TREM2 KO cells may turn

with lower frequency. Consistent with this, analysis of track straightness revealed that TREM2 KO microglia move farther from their origin for the same total distance traveled (**Figure 5E**). Vector autocorrelation, an analysis of directional persistence[62], further confirmed that WT cells turn more frequently than TREM2 KO microglia in response to ADP (**Figure 5-figure supplement 1C, D**). To assess if these differences in TREM2 KO cells require sustained Ca^{2+} influx, we analyzed microglial motility in response to ADP stimulation in the absence of extracellular Ca^{2+} (**Figure 5F-J**). Mean-squared displacement (MSD) and cell-track overlay plots showed that motility is constrained when Ca^{2+} is removed from the external bath in both WT and TREM2 KO cells (**Figure 5A, B vs. F, G**). In the absence of extracellular Ca^{2+}, TREM2 KO microglia showed similar mean speed, displacement, and track-straightness as WT cells (**Figure 5C-E vs H-J**). We conclude that increases in microglial motility (mean speed, displacement, and straightness) require sustained Ca^{2+} influx, and that deletion of TREM2 reduces microglial turning in response to ADP.

We next analyzed the effects of TREM2 deletion on process-extension in microglia. Treatment with ADP induced a dramatic increase in the number of branches and length of processes extended in both WT and TREM2 KO microglia (**Figure 5K, L**). Comparison of the absolute number of branches and process length after ADP treatment, as well as the relative fold-increase in these parameters from baseline indicated that process extension is not affected in TREM2 KO microglia (**Figure 5K-M, figure 5-figure supplement 2A, B**). We note that the greater fold-change in process extension in TREM2 KO cells can be attributed to the reduced morphological complexity of these cells prior to stimulation. Finally, ADP stimulation in Ca^{2+}-free medium did not induce process extension in WT cells, and only a modest increase in

277 TREM2 KO cells (**Figure 5-figure supplement 2A and B vs C and D**). Together, these results
278 indicate that sustained Ca^{2+} entry across the PM is required for optimal microglial process
279 extension in both WT and TREM2 KO microglia.
280
281 **Cytosolic Ca^{2+} levels tune motility in TREM2 KO iPSC-microglia**
282 To further characterize the effects of sustained Ca^{2+} signals on microglial motility, we used
283 Salsa6f-expressing iPSC WT and TREM2 KO reporter lines to monitor cytosolic Ca^{2+} and motility
284 simultaneously in individual cells (**Figure 6-figure supplement 1**). To isolate the effects of
285 sustained Ca^{2+} elevations on microglia motility, and eliminate any contribution from Ca^{2+}
286 independent signaling pathways, we used a protocol that relies on triggering SOCE and varying
287 external Ca^{2+} to maintain cytosolic Ca^{2+} at "low" or "high" levels in the Salsa6f reporter line
288 (**Figure 6A-C**), similar to our previous study in T lymphocytes[63]. In WT cells, lowering
289 extracellular Ca^{2+} from 2 to 0.2 mM predictably decreased the G/R ratio but did not influence
290 mean track speed, 10-minute track displacement, or track straightness (**Figure 6C, D top**).
291 However, in TREM2 KO microglia, reducing Ca^{2+} to a lower level significantly increased speed,
292 displacement, and track straightness (**Figure 6C, D bottom**). These data suggest that motility
293 characteristics of TREM2 KO microglia are more sensitive to changes in cytoplasmic Ca^{2+} levels
294 than in WT cells. Similar results were obtained upon addition of ADP in this paradigm,
295 suggesting that long-lasting Ca^{2+} elevations may override effects of Ca^{2+}-independent ADP
296 signaling on cell motility (**Figure 6-figure supplement 2A**).
297 To further analyze the Ca^{2+} dependence of microglial motility, we plotted Salsa6f G/R
298 Ca^{2+} ratios for each individual cell at every time point against the instantaneous speeds of that

cell (**Figure 6E**). These data revealed a stronger dependence of instantaneous speed on Ca^{2+} levels in TREM2 KO microglia (**Figure 6F**). Furthermore, when stratifying cell speed arbitrarily as "fast" (> 10 μm/min) or "slow" (< 10 μm/min), we observe a marked reduction in the percentage of "fast" cells when Ca^{2+} levels are high in TREM2 KO microglia (**Figure 6G**). Interestingly, frame-to-frame cell displacement correlated with cytosolic Ca^{2+} to the same degree in both WT and KO cells (**Figure 6-figure supplement 2B, C**). Together, TREM2 KO human microglia are more sensitive to tuning of motility by cytosolic Ca^{2+} than WT cells.

Chemotactic defects in TREM2 KO microglia are rescued by dampening purinergic receptor activity

To assess the physiological significance of TREM2 deletion on microglial motility over longer time scales, we performed a scratch wound assay. At baseline, both WT and TREM2 KO microglia migrated into the cell free area at similar rates, consistent with our previous findings[41] (**Figure 7- figure supplement 1**). Addition of ADP to this system accelerated the scratch wound closure rates to the same extent in WT and TREM2 KO. *In vivo,* directed migration of microglia is often driven by gradients of ADP from dying or injured cells[12,30]. Because no chemical gradient is formed in the scratch wound assay[64], we studied microglial chemotaxis toward ADP over a stable gradient using two-chamber microfluidic devices. Consistent with previous findings, WT iPSC-microglia directionally migrated up the concentration gradient of ADP resulting in higher numbers of cells within the central chamber[41,65]. In the absence of a chemotactic cue, this directional migration was lost (**Figure 7A**). This assay revealed a deficit of chemotaxis in TREM2 KO microglia (**Figure 7A**), mirroring reports that TREM2 KO microglia are unable to migrate

toward amyloid plaques in AD[40,41,66]. Given that ADP hypersensitivity in TREM2 KO cells is driven by increased expression of P2Y receptors, we examined the effects of dampening P2Y signaling to WT levels. Treatment with the $P2Y_{12}$ receptor antagonist, PSB 0739, reduced Ca^{2+} responses in TREM2 KO cells and rescued the migration deficit in the chemotaxis assay (**Figure 7B-C)**. These results link the increased Ca^{2+} signals and altered motility characteristics evoked by ADP in TREM2 KO cells to microglial chemotaxis toward areas of tissue damage, a vital functional response in microglia.

Discussion

This study focuses on two aims: understanding the roles of purinergic signaling in regulating human microglial motility behavior; and elucidating the impact of TREM2 loss of function on this Ca^{2+} signaling pathway. We find that sustained Ca^{2+} influx in response to ADP regulates microglial process extension, motility speed, and turning behavior. A key observation in our study is that microglia lacking TREM2 are highly sensitive to ADP-mediated signaling and show exaggerated cytoplasmic Ca^{2+} responses. Using novel iPSC-microglia lines that express a ratiometric, genetically encoded Ca^{2+} probe, Salsa6f, we found that the motility characteristics of human wild-type and TREM2-knockout microglia are differentially tuned by Ca^{2+} signaling. Informed by these discoveries, we were able to rescue chemotactic deficiencies in TREM2-knockout microglia by dampening purinergic receptor signaling.

We provide several lines of evidence to show that hyper-responsiveness to purinergic ADP signaling in TREM2 KO microglia is driven primarily by increased purinergic $P2Y_{12}$ and $P2Y_{13}$ receptor expression: (1) Ca^{2+} response is completely abrogated in the presence of $P2Y_{12}$ and $P2Y_{13}$ receptor inhibitors; (2) RNA-sequencing data shows significant increase in expression of $P2Y_{12}$ and $P2Y_{13}$ receptor transcripts but minimal fold-change in other regulators of Ca^{2+} signaling (IP3R, STIM, Orai, SERCA and PMCA); and (3) labelling of surface $P2Y_{12}$ receptors shows greater PM expression in the TREM2 KOs. Furthermore, functional assays rule out any role for Ca^{2+} clearance mechanisms or any difference in maximal IP_3 and SOCE activity as a cause of increased sustained Ca^{2+} signal in TREM2 KO cells. Mechanistically, this increase in Ca^{2+} signals is driven by enhanced IP_3-mediated ER store-release coupled to SOCE. Indeed, based on the dose-response curves for peak ADP-Ca^{2+} responses in Ca^{2+} free buffer, TREM2 KO cells have

an EC_{50} at least 10-fold lower than WT cells. As a functional consequence, TREM2 KO microglia exhibit a defect in turning behavior, and show greater displacement over time despite moving with similar speeds as the WT cells. The increased frequency in turning in WT microglia (relative to TREM KO cells) reflects greater canceling of the velocity vectors, which take the direction of motility into account. This restricts cell motility to more confined regions, potentially allowing for more frequent path correction. It is important to note that these motility differences with ADP are observed after acute treatment and in the absence of any gradient.

Interestingly, deletion of TREM2 had no significant impact on scratch wound closure rates, over a time scale of 24 hours in the presence of a constant concentration of ADP[67]. However, we find in a directional chemotaxis assay towards a gradient of ADP concentration that TREM2 KO cells are unable to migrate as efficiently as WT cells, concordant with previous studies showing reduced migration of TREM2 KO cells towards Aβ plaques[41]. Enhanced ADP signaling likely abolishes the ability of TREM2 KO cells to distinguish gradations of the agonist, and this loss of gradient-sensing results in an inability to perform directed migration. We speculate that increased ADP Ca^{2+} signaling in TREM2 KO cells may result in Ca^{2+} signaling domains that are no longer restricted to the cell region near to the highest ADP concentrations, and disrupt the polarity of key signaling molecules that drive directed cell motility.

The amplitude and duration of Ca^{2+} signals shape specificity of downstream cellular responses. Our experiments with ADP in Ca^{2+} free medium revealed that a transient Ca^{2+} signal is insufficient to induce microglial motility in either WT or TREM2 KO cells. Previous studies have shown that mouse microglia with genetic deletion of STIM1 or Orai1 also show defects in cell migration to ATP[57,68], likely because diminished SOCE renders them unable to sustain Ca^{2+}

373 signals in response to ATP. The dependence of motility on prolonged purinergic Ca^{2+} signals
374 may thus be a general feature of microglia. In contrast, a Ca^{2+} transient can initiate some
375 process extension in TREM2 KO but not in WT microglia, suggesting a threshold for ADP
376 signaling that is reached in KO but not WT cells, and highlighting subtle differences in the Ca^{2+}
377 requirement for motility and process extension in TREM2 KO microglia.

378 To directly monitor Ca^{2+} signaling and motility simultaneously in individual cells, we
379 developed a novel iPSC-microglia cell-line expressing a genetically encoded, ratiometric Ca^{2+}
380 indicator Salsa6f, a GCaMP6f-tdTomato fusion protein. Because Salsa6f allows simultaneous
381 measurement of Ca^{2+} signal and tracking of processes, this Salsa6f iPSC line is likely to be a
382 useful tool to dissect the relationship between Ca^{2+} signaling and the function of various iPSC-
383 derived human cell types including neurons, astrocytes, and microglia. In addition, this line may
384 be readily xenotransplanted for use with human/microglia chimeric models to examine
385 functional Ca^{2+} responses to injury and pathology *in vivo*. Using Salsa6f-expressing microglia, we
386 uncovered critical differences in how Ca^{2+} levels tune motility in WT and TREM2 KO microglia.
387 By tracking instantaneous velocity at the same time as Salsa6f Ca^{2+} ratios in individual cells, we
388 found that TREM2 KO cell motility showed a greater sensitivity to changes in cytosolic Ca^{2+}
389 levels with significantly higher speeds than WT cells at lower Ca^{2+} and a more dramatic
390 reduction in cell speed at high Ca^{2+} levels. It is possible that high cytosolic Ca^{2+} serves as a
391 temporary STOP signal in microglia similar to its effects on T cells [63]; we further speculate that
392 TREM2 KO cells may be more subject to this effect with ADP, given the higher expression of
393 $P2RY_{12}$ and $P2Y_{13}$ receptors. Accordingly, reducing cytosolic Ca^{2+}, resulted in increased mean
394 speed, displacement, and straighter paths for TREM2 KO iPSC-microglia, but had no effect on

these motility metrics in WT cells suggesting that TREM2 KO cells may display a greater dynamic range in regulating their motility in response to sustained Ca^{2+} elevations. Consistent with this observation, chemotaxis in TREM2 KO cells was restored by partially inhibiting $P2Y_{12}$ receptors. In response to neurodegenerative disease, microglia down-regulate $P2Y_{12}$ receptors[23,25,31]. Active regulation of purinergic receptor expression is critical for sensing ADP gradients and decreasing motility near the chemotactic source. *In vivo* studies[21,23,41] suggest that TREM2 KO microglia are unable to down-regulate P2Y receptor expression upon activation, which may lead to the known chemotactic deficits in these cells.

The studies presented here provide evidence that reducing purinergic receptor activity may be clinically applicable in Alzheimer's patients with TREM2 loss of function mutations [40,55,69]. Pharmacologically targeting $P2Y_{12}$ receptors to dampen both the Ca^{2+} dependent (PLC) and independent (DAG) arms of the GPCR signaling pathway may be useful to control microglial activation and motility. However, our results suggest that altering downstream Ca^{2+} flux may be sufficient, and thus, CRAC (Orai1) channel blockers that would specifically inhibit the sustained Ca^{2+} signals without affecting the initial Ca^{2+} transient or the activation of DAG may provide a more targeted approach.

Currently, TREM2 activating antibodies are being examined in early stage clinical trials for Alzheimer's disease[70,71], making it critically important to understand the broad consequences of TREM2 signaling. Therefore, an understanding of how TREM2 influences responses to purinergic signals and regulates cytosolic Ca^{2+} in human iPSC-microglia is critical. Beyond TREM2, we have found that protective variants in MS4A6A and PLCG2 gene expression

also decrease $P2Y_{12}$ and $P2Y_{13}$ receptor expression (unpublished data), suggesting this mechanism of microglial activation could be common across several microglial AD risk loci.

In summary, deletion of TREM2 renders iPSC-microglia highly sensitive to ADP, leading to prolonged Ca^{2+} influx which increases cell displacement by decreasing cell turning. Despite this, TREM2 KO microglia show a defect in chemotaxis that is likely due to their inability to sense ADP gradients and make appropriate course corrections. Decreasing purinergic signaling in TREM2 KO microglia rescues directional chemotactic migration. We suggest that purinergic modulation or direct modulation of Ca^{2+} signaling could provide novel therapeutic strategies in many AD patient populations, not solely those with reduced TREM2 function.

Figure Legends

Figure 1: Microglia lacking TREM2 show exaggerated Ca^{2+} responses to purinergic stimulation. (**A**) Representative red-green channel overlay images of WT (top) and TREM2 KO (bottom) iPSC-microglia loaded with Fluo-4 (green) and Fura-red (red) showing resting cytosolic Ca^{2+} before ADP, and Ca^{2+} levels 15 sec and 5 min after ADP addition. Scale bar= 20 μm. (**B)** Average traces (left panels) showing changes in cytosolic Ca^{2+} in response to 2.5 μM ADP in 1 mM Ca^{2+} buffer (n=39-44 cells). Baseline-subtracted peak Ca^{2+} response and cytosolic Ca^{2+} levels 5 min after ADP shown on the right (n=250-274 cells, 5 experiments, Mann-Whitney test). (**C-D**) Cytosolic Ca^{2+} response to ADP as in **A** and **B** but in iPSC microglia expressing the GCaMP6f-tdTomato fusion Ca^{2+} probe Salsa6f (n=41-53 cells, 2 independent experiments, Mann-Whitney test). Images in (**C**) are overlay of GCaMP6f (green) and tdTomato (red) channel images. Scale bar= 20 μm. (**E**) Ca^{2+} responses to 2.5 μM ATP in WT and TREM2 KO iPSC-microglia. Average traces (left panel, n=63-71 cells) and bar-graph summary of peak cytosolic Ca^{2+} and Ca^{2+} after 5 min (right panel, 165-179 cells, 3 experiments, Mann-Whitney test). (**F**) Ca^{2+} responses to 10 μM UTP. Average traces (45-55 cells) and summary of peak cytosolic Ca^{2+} and Ca^{2+} after 5 min (175-269 cells, 3 experiments, Mann-Whitney test). Data shown as mean ± SEM for traces and bar-graphs. *P values* indicated by *** for $P < 0.001$, **** for $P < 0.0001$.

Figure 2: Higher sensitivity of TREM2 KO microglia to ADP is driven by increased purinergic receptor expression. (**A**) Schematic highlighting key downstream Ca^{2+} signaling events triggered by ADP. Cytosolic Ca^{2+} response to ADP is determined by functional expression and activity of $P2Y_{12}$ and $P2Y_{13}$ receptors, IP_3 receptors, ER-store Ca^{2+} content, and store-operated Ca^{2+} entry (SOCE) regulated by STIM and Orai proteins. (**B**) Representative images (left panel) showing overlay of Fluo-4 (green) and Fura-red (red) channels in WT (top) and TREM2 KO (bottom) iPSC-microglia before and peak Ca^{2+} response after ADP addition in Ca^{2+} free buffer. Scale bar= 20 μm. Average trace showing Ca^{2+} response to ADP in Ca^{2+}-free buffer (middle panel, 64-83 cells). Quantification of peak signal (right panel, n=264-289 cells, 4 experiments, Mann-Whitney test). (**C-E**) Dose-response curves showing baseline-subtracted peak Ca^{2+} responses to ADP in Ca^{2+}-

free buffer (**C**), percent of "responding" cells (**D**) and peak Ca^{2+} responses only in "responding" cells (**E**). N= 84-474 WT cells and 70-468 TREM2 KO cells, 2-5 experiments. (**F**) RNA normalized read counts of $P2Y_{12}$ and $P2Y_{13}$ receptor expression from bulk RNA-sequencing of WT and TREM2 KO iPSC-microglia (n=4, adjusted *P-values* from DESeq2). (**G**) Representative histogram (left panel) showing PM expression of $P2Y_{12}$ receptor in WT and TREM2 KO microglia. Cells were stained with BV421 labelled anti-human $P2Y_{12}$ receptor antibody. Isotype control is shown as dashed line. Right panel shows summary of median fluorescence intensity (MFI) of $P2Y_{12}$ receptor-labelled cells (n= 10 samples each, Students t- test). (**H**) Ca^{2+} traces (left panel) showing response to 1 μM ADP in Ca^{2+}-free buffer after 30 min pre-treatment with a combination of $P2Y_{12}$ receptor antagonist PSB 0739 (10 μM) and $P2Y_{13}$ receptor antagonist MRS 2211 (10 μM). Summary of the peak Ca^{2+} response (right panel, n=40-79 cells, 2 experiments, Mann-Whitney test). Data are mean ± SEM. *P values* indicated by **** for $P < 0.0001$.

Figure 3: Regulation of ADP-evoked SOCE in WT and TREM2 KO microglia. (**A**) SOCE in WT microglia triggered with thapsigargin (TG, 2 μM) in Ca^{2+}-free buffer followed by re-addition of 1 mM Ca^{2+} in the absence (control, grey trace) or presence (red trace) of the Orai channel inhibitor Synta66 (n=34-48 cells). Cells were pretreated with Synta66 (10 μM) for 30 min before imaging. Bar-graph summary of the rate of Ca^{2+} influx (n=80-137 cells, 2 experiments, Mann-Whitney test). (**B**) SOCE evoked by ADP (2.5 μM) in WT microglia (grey trace), using a similar Ca^{2+} addback protocol as in **A**. Red trace shows effect of Synta66 on ADP-evoked SOCE. Right panel shows bar-graph summary of the rate of ADP-triggered Ca^{2+} influx after re-addition of 1 mM Ca^{2+} (n=148-155 cells, 2 experiments, Mann-Whitney test). (**C**) Comparison of SOCE evoked with TG (2 μM) in WT and TREM2 KO cells (n=90-129 cells). Bar-graph summaries of ER store-release quantified as area under the curve, rate of SOCE, and peak SOCE (n=187-266 cells, 2 experiments, Mann-Whitney test). (**D**) Traces showing ADP-evoked SOCE in WT and TREM2 KO microglia after depleting stores with 100 nM ADP in Ca^{2+} free buffer and re-addition of 1 mM Ca^{2+} (left panel, n=97-114 cells). Comparison of ADP-evoked cytosolic Ca^{2+} peak, peak SOCE and SOCE rate (right panel, n=234-313 cells, 3 experiments, Mann-Whitney test). **(E)** Ionomycin-pulse experiment to measure residual ER Ca^{2+} pool in cells after initial treatment with ADP. WT

and TREM2 KO cells were pulsed sequentially with ADP first (200 nM) and subsequently treated with ionomycin (1 μM) to empty and measure the residual pool of ER Ca^{2+}. Imaging was done entirely in Ca^{2+}-free buffer to prevent Ca^{2+} influx across the PM. Average trace (left panel), Peak ADP Ca^{2+} response (middle panel) and peak ionomycin-induced Ca^{2+} response (right panel) (n=38-60 cells, 3-4 experiments, Mann-Whitney test). **(F)** Average trace (left, 71-117 cells) and summary of ER store-release after 2 μM ionomycin treatment in Ca^{2+} free buffer (right, 146-234 cells, 2 experiments; **ns,** *non-significant P > 0.05,* Mann-Whitney test). (**G**) Same as H but in response to UV IP_3 uncaging (167-200 cells, **ns***, non-significant P > 0.05,* nonparametric t-test). Data shown as mean ± SEM for traces and bar-graphs. Data are mean ± SEM. *P values* indicated by **ns** for non-significant, * for *P < 0.05* and **** for *P < 0.0001*.

Figure 4: Nondirectional ADP exposure increases WT microglial speed and process extension. (**A**) Average trace showing closure of scratch wound produced with IncuCyte S3 WoundMaker. iPSC-microglia imaged every 30 min after scratch wound with or without ADP stimulation (n=4 wells; 2 images per well). (**B**) Representative image of WT iPSC-microglia motility 30 min after ADP exposure with cell tracks overlain (left). Pseudocolored images (center) across time: 0 min (red), 4 min (orange), 8 min (yellow), 12 min (green), 16 min (cyan), 20 min (blue), 24 min (purple), 28 min (magenta). Scale bar= 100 μm. White boxes zoomed in at right to demonstrate motile (top) and non-motile (bottom) cells. (**C**) Representative color images (top left) and displacement vectors (bottom left) of WT iPSC-microglia at baseline (no ADP, grey) and 30 min after 2.5 μM ADP treatment (red). Summary of Mean Speed (μm/min), Displacement over 10 min (μm/10 min) and Track straightness (track length/track displacement) (414-602 cells, 2 experiments). (**D**) Representative images, displacement vectors, and quantification of WT iPSC-microglia motility for 20 min following ADP addition. Cells were pre-treated with vehicle (grey), MRS 2211 (10 μM, gold), or PBS 0739 (10 μM, blue) (180-187 cells, 2 experiments). (**E**) Representative images, displacement vectors, and quantification of WT iPSC-microglia motility after ADP in 1 mM Ca^{2+} (light grey) or Ca^{2+}-free buffer (dark grey) (401-602 cells, 3 experiments). (**F**) Representative images (left) and process extension (right) of iPSC-microglia (cytoplasmic GFP, grey) before or 30 min after ADP addition. Cells were pre-treated with vehicle

(grey), MRS 2211 (10 μM, gold), or PBS 0739 (10 μM, blue) (52-163 cells, 3-4 experiments). (**C-F**) One way ANOVA with Tukey post hoc test. Data shown as mean ± SEM (A, F) and as violin plots with mean, 25th and 75th percentile (C-E). *P values* indicated by **ns** for non-significant, * for *P < 0.05,* ** for *P < 0.01,* *** for *P < 0.001* and **** for *P < 0.0001*.

Figure 5: ADP-driven process extension and cell displacement are increased in TREM2 KO iPSC-microglia. (**A-E**) Motility of WT (grey) and TREM2 KO (green) iPSC-microglia over 20 min following ADP addition in 1 mM Ca^{2+}-containing buffer. (**A**) Plots of track displacement in μm centered from point of origin at (0,0). (**B**) Mean-squared displacement (MSD) vs time. Mean-cell track speeds (**C**), total track displacement in 10-min interval (**D**), and track straightness (**E**) for 130-327 cells, 7 experiments, student's t-test. (**F-J**). Same as (**A-F**) but in Ca^{2+}-free medium (125-279 cells, 2 experiments, student's t-test). (**K**) Representative images of GFP-expressing WT (top) and TREM2 KO (bottom) iPSC-microglia, before and 30 min after 2.5 μM ADP addition. (**L**) Quantification of total number of branches per cell before and after ADP treatment (left) and paired dot-plots showing fold change in branch number from pre-ADP levels (right). Each data-point represents an imaging field in the paired-plots. (**M**) Total process length before and after ADP treatment displayed as raw values per cell (left) and as fold change from baseline conditions per imaging field (right). For **L** and **M,** n=151-158 cells, WT; 133-167 cells, KO; 9-10 imaging fields, 3-4 experiments. One-way ANOVA with multiple comparisons for single-cell data, two-tailed paired t-test for the paired-plots. Data shown as mean ± SEM (B, G, L, M) and as violin plots with mean, 25th and 75th percentile (C- E, H-J). *P values* indicated by **ns** for non-significant, * for *P < 0.05,* ** for *P < 0.01* and **** for *P < 0.0001*.

Figure 6: Cytosolic Ca^{2+} levels tune microglial motility in TREM2 KO cells. (**A**) Schematic of traditional SOCE pathway with store-refilling (left) and protocol for sustaining cytoplasmic Ca^{2+} to "low" and "high" levels with 0.2 and 2mM extracellular Ca^{2+} and using TG to inhibit store-refilling (right). (**B**) Average SOCE traces in WT Salsa6f iPSC-microglia showing changes in cytoplasmic Ca^{2+} after addition of either 0.2 or 2 mM extracellular Ca^{2+}(n=78-110 cells). (**C**) Average change in cytoplasmic Ca^{2+} levels in WT and TREM2 KO microglia over 25 min after

SOCE activation. (**D**) Comparison of Ca^{2+} levels and microglia motility in WT (top) and TREM2 KO (bottom) microglia. Cytosolic Ca^{2+} levels indicated by instantaneous single-cell G/R Ratio (n=74-158 cells). Mean of instantaneous speeds, track displacement and track straightness calculated as before in Figures 3 and 4. Yellow (0.2 mM Ca, TG), green (2 mM Ca, TG). Students t-test **** $p < 0.0001$; ** $p = 0.0062$; * $p = 0.432$; ns > 0.9999. (**E**) Correlation of instantaneous Ca^{2+} and instantaneous speed in WT and KO cells. Red line denotes 10 μm/sec (cells above this threshold considered "fast-moving"). For WT: $p < 0.0001$; $r = -0.1316$; number pairs = 5850. For KO: $p < 0.0001$; $r = -0.1433$; number pairs = 6063 (Spearman's correlation). (**F**) Mean speed of cells binned by instantaneous G/R Ca^{2+} ratio (1-way ANOVA **** $p < 0.0001$). Each data point is calculated for a bin increment of 0.5 G/R ratio. (**G**) Percentage of fast-moving cells quantified as a function of G/R Ca^{2+} ratio. X-axis G/R ratios binned in increments of 0.5 as in **F**. In **E-G**, n=78-100 cells. Data shown as mean ± SEM (B, F) and as violin plots with mean, 25^{th} and 75^{th} percentile (D). *P values* indicated by **ns** for non-significant, * for *P < 0.05,* ** for *P < 0.01* and **** for *P < 0.0001*.

Figure 7: Migration deficits in TREM2 KO microglia are rescued by inhibition of purinergic signaling. (**A**) Migration towards ADP in a two-chamber microfluidic device. Representative images of RFP expressing microglia that migrated into the central chamber 3 days after 100 ng/mL ADP addition. Dotted circle delineates separation of inner and outer chamber. Scale bar = 500 μm. Quantification of microglial migration (right panel). Migrated cell counts are normalized to WT cells treated with ADP (n=3-4 experiments; One-way ANOVA with multiple comparisons). (**B**) Baseline subtracted peak ratiometric Ca^{2+} signal in response to 2.5 μM ADP in 1 mM extracellular Ca^{2+}, and in the presence or absence of 10 μM PSB 0739 (44 cells, WT; 39-43 cells, KO; representative of 3 independent experiments; One-way ANOVA with multiple comparisons). (**C**) Two-chamber migration to 100 ng/mL ADP with or without 10 μM PSB 0739. Values are normalized to WT cells with ADP (n=3-4 experiments; One-way ANOVA with multiple comparisons). Representative images shown on the left. Scale bar = 500 μm. Data shown as mean ± SEM. *P values* indicated by **ns** for non-significant, * for *P < 0.05,* ** for *P < 0.01* and **** for *P < 0.0001*.

573 **Supplementary Figure Legends**

574

575 **Figure 1-figure supplement 1: Validation of Salsa6f transgenic iPSC-microglia.** (**A**)
576 Representative bright field, green (GCaMP6f), red (tdTomato), and Green/Red channel overlay
577 images of transgenic Salsa6f expressing iPSC-microglia at low (top row) and high (bottom row)
578 cytosolic Ca^{2+} levels. Cells were treated with 2 μM thapsigargin (TG) to deplete stores and
579 evoke store-operated Ca^{2+} entry (SOCE). Images are shown at the end of TG treatment for low
580 Ca^{2+} and at the peak of SOCE for high Ca^{2+}. Scale bar = 20 μm. (**B**) Trace of average change in
581 fluorescence intensity of tdTomato (red) and GCamp6f (green) over time. Summary of GCaMP6f
582 and tdTomato intensities before and after invoking SOCE are shown on the right. (**C**)
583 Ratiometric GCaMP6f/ tdTomato signal (Green/ Red or G/R Ratio) over time calculated from
584 (**B**). Summary of G/R Ratio at low and high cytosolic Ca^{2+} (**B-C**, n=19 cells, Mann-Whitney test).
585 (**D**) Immunofluorescence images showing staining for the microglia-specific marker IBA1 in
586 either resting or activated WT or Salsa6f-transgenic iPSC-microglia (left). Right panel shows
587 quantification of IBA1 protein expression (n=4 wells, 2 independent images per well, t-test).
588 Cells were activated with 100 ng/mL LPS (lipopolysaccharide for 24 hours). (**E**) Microglia cell
589 counts at final day of differentiation (n=3 wells, t-test). (**F**) Phagocytosis of synaptosomes in WT
590 non-transgenic (open circle) and Salsa6f-expressing (closed circle) iPSC-microglia. Cytochalasin
591 D (grey, 10 μM) used as negative control to inhibit phagocytosis. Live cultures imaged on
592 IncuCyte S3 (n=4 wells; 4 images per well). (**G**) Phagocytic load at 24 hr for synaptosomes, beta-
593 amyloid, zymosan A, and *S. aureus* (n=4 wells; 4 images per well; one way ANOVA with Tukey
594 post-hoc test). Data shown as mean ± SEM for traces and bar-graphs. *P values* indicated by **ns**
595 for non-significant, **** for $P < 0.0001$.

596

597 **Figure 1-figure supplement 2: Comparison of cytosolic Ca^{2+} signal over time triggered by**
598 **various purinergic agonists.** (**A**) Representative trace showing changes in cytosolic Ca^{2+} in a
599 single cell to illustrate the scheme for measuring cytosolic Ca^{2+} level 5 min after agonist
600 application. (**B**) Bar-graph summary of cytosolic Ca^{2+} levels in WT and TREM2 KO iPSC-microglia
601 5 min after application of 2.5 μM ADP (blue), 2.5 μM ATP (red), and 10 μM UTP (yellow).

N=165-274 cells pooled from 2-3 experiments. One-way ANOVA with multiple comparisons. Data shown as mean ± SEM for the bar-graph. *P values* indicated by **** for *P < 0.0001.*

Figure 2-figure supplement 1: Role of $P2Y_{12}$ and $P2Y_{13}$ receptors in ADP-mediated augmentation of store-release in TREM2 KO microglia. (**A**) Representative green (GCaMP6f) and red (tdTomato) channel overlay images of WT (top) and TREM2 KO (bottom) iPSC-microglia before and peak Ca^{2+} response after ADP addition in Ca^{2+}-free buffer. Scale bar = 20 μm. (**B**) Average trace (left panel) showing Ca^{2+} response to 100 nM ADP in Ca^{2+}-free buffer. Quantification of peak signal (right panel, n=46-75 cells, 2 experiments, Mann-Whitney test). (**C**) Comparison of peak cytosolic Ca^{2+} in response to ADP (2.5 μM ADP) in 1 mM Ca^{2+} or Ca^{2+}-free buffer (n=38-96 cells, ordinary one-way ANOVA with multiple comparisons). (**D**) Volcano plot of differentially expressed genes from bulk RNA-sequencing of WT and TREM2 KO iPSC-microglia (n=4). Genes for IP3R, STIM1, and ORAI1 are highlighted. (**E**) RNA normalized read counts for IP_3 receptor type 2 (ITPR2), PMCA1 (ATP2B1), SERCA2 (ATP2A2), SERCA3 (ATP2A3), STIM1, and ORAI1 in WT and TREM2 KO iPSC-microglia. Isoforms expressed lower than 10 reads in any sample are not considered expressed and are not shown. Relative expression of $P2Y_{12}$ and $P2Y_{13}$ receptors are shown for comparison of the relative fold-change between WT and TREM2 KO cells. (**F-G**) Peak Ca^{2+} response in Ca^{2+} free buffer after treatment with 1 or 10 μM ADP in the presence of $P2Y_{12}$ receptor antagonist PSB 0739 (**F**) or $P2Y_{13}$ receptor antagonist MRS 2211 (**G**), respectively. Cells were pretreated with 10 μM of PSB 0739 or 10 μM MRS 2211 for 30 min before imaging. (72-128 cells, **F**; 83-117 cells, **G**; representative of 3 experiments, Mann-Whitney Test). Data shown as mean ± SEM for traces and bar-graphs. Data shown as mean ± SEM for traces and bar-graphs. *P values* indicated by **ns** for non-significant, ** for *P < 0.01,* *** for *P < 0.001,* **** for *P < 0.0001.*

Figure 3-figure supplement 1: Regulation of SOCE in iPSC-microglia. (**A**) Average trace showing SOCE triggered in TREM2 KO microglia via emptying ER Ca^{2+} stores with thapsigargin (TG, 2 μM) in Ca^{2+}-free buffer followed by re-addition of 1 mM Ca^{2+} in the absence (control, green trace) or presence (red trace) of the Orai channel inhibitor Synta66. Cells were pretreated with Synta66

(10 μM) for 30 min before experiment. Bar-graph summary of the rate of Ca^{2+} influx after re-addition of 1 mM Ca^{2+} (80-126 cells, Mann-Whitney test). (**B**) SOCE evoked by ADP (2.5 μM) in TREM2 KO microglia (green trace), using a similar Ca^{2+} addback protocol. Red trace shows effect of Synta66 on ADP-evoked SOCE. Right panel summarizes the rate of ADP-triggered Ca^{2+} influx after re-addition of 1 mM Ca^{2+} (n= 125- 154 cells, 2 experiments, Mann-Whitney test). (**C-D**) Cytosolic Ca^{2+} response to ADP in TREM2 KO iPSC-microglia pre-treated with 2-APB (50 μM) or Gd^{3+} (5 μM) to block store-operated Ca^{2+} entry (SOCE). Average traces (**C**), baseline- subtracted initial peak Ca^{2+} responses to ADP (**D**, left panel), and baseline-subtracted Ca^{2+} after 5 min of ADP addition (**D**, right panel) are shown (n= 41-74 cells, ordinary one-way ANOVA with multiple comparisons). (**E-F**) Role of Orai1 in TG- and ADP-evoked SOCE in iPSC-microglia. (**E**) Comparison of TG-evoked SOCE in WT and Orai1 KO cell showing average traces (left panel) and summary of SOCE rate (right panel; n= 42-54 cells, 3-4 experiments, Mann-Whitney test). (**F**) ADP-evoked SOCE in WT and Orai1 KO showing average traces (left panel) and summary of SOCE rate (right panel; n= 42-53 cells, 3-4 experiments, Mann-Whitney test). Data shown as mean ± SEM for traces and bar-graphs. *P values* indicated by **ns** for non-significant, **** for *P < 0.0001.*

Figure 3-figure supplement 2: ADP depletes ER Ca^{2+} stores to a greater extent in TREM2 KO microglia. (**A**) TG-pulse experiment to measure residual ER Ca^{2+} pool in cells after initial treatment with ADP (1 μM) and subsequent treatment with thapsigargin (2 μM). Imaging was done in Ca^{2+}-free buffer to prevent Ca^{2+} influx across the PM. Average trace (left panel), Peak ADP Ca^{2+} response (middle panel) and extent of TG-induced ER store-release measured as area under curve (AUC, right panel) (n=81-108 cells, Mann-Whitney test). (**B**) Control experiment comparing the ER-Ca^{2+} pool in WT and TREM2 KO microglia after store-depletion with TG, and without any pretreatment with ADP (n=29- 63 cells, Mann-Whitney test). (**C-D**) Relationship between ADP-induced store-release and SOCE in iPSC-microglia. (**C**) Representative single-cell trace of Ca^{2+} signal in response to ADP in 1 mM extracellular Ca^{2+} buffer showing the scheme for measuring ER store-release as the initial Ca^{2+} peak and SOCE as cytosolic Ca^{2+} level 5 min after ADP application. (**D**) Scatter-plot showing correlation of initial ADP-induced Ca^{2+} response (store-release) and cytoplasmic Ca^{2+} after 5 min (SOCE) in WT (grey) and KO (green) cells

(n=866-935 cells from multiple imaging runs with a range of ADP doses; in μM: 0.001, 0.1, 0.5, 1, 2, 2.5, 5, 10. Comparison of slopes between WT and TREM2 KO: *P = 0.7631*; Extra sum of squares F test). (**E-F**) Comparison of cytosolic Ca^{2+} clearance indicative of PMCA pump activity in WT and TREM2 KO microglia. SOCE was invoked and rate of Ca^{2+} decline was measured after addition of 0 mM Ca^{2+}. (**E**) Average trace showing invoking SOCE with 2 μM TG (left panel). Right panel shows the drop in cytosolic Ca^{2+} following addition of Ca^{2+} free solution as highlighted (pink) in the SOCE trace (**F**) Summary of rate of Ca^{2+} decline after addition of 0 mM Ca^{2+} (n= 8 imaging fields, 142-175 total cells, Mann-Whitney Test). Data shown as mean ± SEM for traces and bar-graphs. *P values* indicated by **ns** for non-significant, ** for *P < 0.01.*

Figure 4-figure supplement 1: ADP-mediated process extension in WT iPSC-microglia. (A) Representative images of a cell (Cell 1) from a time-lapse experiment showing increased branching and extension of processes in GFP-expressing WT iPSC-microglia, at times indicated following addition of 2.5 μM ADP. Bright field DIC images (top row) and GFP images (bottom row) are shown. (**B**) Another example of a cell (Cell 2) showing process extension in the same imaging field. (**C**) A motile cell (Cell 3) in the same imaging field is shown for comparison. Note the lack of displacement in cells that extend their process, and lack of significant process extension in a highly motile cell. Scale bar: 15 μM.

Figure 5-figure supplement 1: Motility analysis in WT and TREM2 KO iPSC-microglia. (**A**) Summary of microglial mean speeds, displacement over 10 min, and track straightness in open-field migration in the absence of any purinergic stimulation (student's t-test). (**B**) Flower plots show similar displacement from origin for WT (left) and TREM2 KO (right) cells. (**C**) Directional Autocorrelation calculated via DiPer excel macro. Due to lack of directional gradient, directional autocorrelation of motility vectors is expected to drop quickly. Time constants for best-fit single exponential curves are indicated, consistent with increased straightness for TREM2 KO cells treated with ADP. (**D**) Directional autocorrelation of WT (grey) and TREM2 KO (green) iPSC-microglia at baseline (open circles) or after ADP addition (filled circles). Mean autocorrelation values in the first 5 min (left panel, one-way ANOVA) and time (min) until autocorrelation

reaches zero (right panel). Data shown as mean ± SEM for the bar-graph in (D), and as violin plots with mean, 25th and 75th percentile in (A). *P values* indicated by **ns** for non-significant, * for *P < 0.05,* and **** for *P < 0.0001*.

Figure 5-figure supplement 2: Comparison of process extension in WT and TREM2 KO Microglia. Branching and process extension in WT and TREM2 KO iPSC-microglia 30 min after addition of ADP in 1 mM (**A, B**) or 0 mM extracellular Ca^{2+} buffer (**C, D**). (**A**) Data displayed as paired-plots showing average branch number per cell in an imaging field (top row) and normalized to pre-ADP values for each imaging field (middle row). Bottom row shows fold change in branching after ADP treatment for WT (grey) and KO (green) iPSC-microglia. (**B**) Changes in process length in the same dataset as **A**. n=151-158 cells, WT; 133-167 cells, KO; 9-10 imaging fields, 3-4 experiments. (**C, D**) Same analysis as **A, B** but with ADP in Ca^{2+} free buffer. n=137-143 cells, 8 imaging fields, 2-3 experiments. (**A-D**) p-values calculated by two-tailed paired Students t-test for the paired-plots, and by unpaired t-test when comparing fold-change in WT and KO cells. Data shown as paired plots and as mean ± SEM for the bar-graphs. *P values* indicated by **ns** for non-significant, * for *P < 0.05, ** for P < 0.01, *** for P < 0.001* and **** for *P < 0.0001*.

Figure 6-figure supplement 1: Tracking cell motility and cytosolic Ca^{2+} using Salsa6f-expressing iPSC cell-line. (**A**) Average change in single cell fluorescence intensity of tdTomato (red trace) and GCaMP6f (green trace) (left Y-axis) in WT Salsa6f microglia over 5 min following ADP treatment, overlaid with corresponding change is cell displacement over time (black trace, right Y-axis) (n=52-79 cells). (**B**) Same as (A) but for cells tracked over a period of 30 min. Data shown as mean ± SEM for average traces.

Figure 6-figure supplement 2: Motility analysis with varying Ca^{2+}. (**A**) Salsa6f Ca^{2+} ratios and microglia motility in WT (top) and KO (bottom) microglia, with ADP added: yellow (0.2 mM Ca^{2+}, TG + ADP), green (2 mM Ca^{2+}, TG + ADP). Cytosolic Ca^{2+} levels indicated by instantaneous single-

718 cell G/R Ratio. Mean of instantaneous speeds, 10 min track displacement and track straightness
719 calculated as before. Students t-test **** $p < 0.0001$; *** $p = 0.0001$. n=164-393 cells. (**B, C**)
720 Ca^{2+} dependence of track displacement length in 0.2 mM Ca^{2+} in WT cells (**B**) and TREM2 KO
721 cells (**C**). Correlation between instantaneous Ca^{2+} and frame-to-frame displacement (left
722 panels). Each dot represents an individual cell for an individual frame. Dotted red line
723 represents displacement of 200 μm^2. Mean square of frame-to-frame displacement of cells
724 binned by instantaneous G/R Ca^{2+} ratio (middle panels, 1-way ANOVA **** $p < 0.0001$). Each
725 data point is calculated for a bin increment of 0.5 G/R ratio. Summary of cells with frame-to-
726 frame square displacement > 200 μm^2 (right panels). WT cells (**B**) displace less than KO cells (**C**).
727 For each cell type, larger displacements are correlated with lower G/R Ca^{2+} ratios. Cells which
728 maintain elevated cytoplasmic Ca^{2+} do not displace as far. For WT: $p < 0.0001$; $r = -0.4778$;
729 number pairs = 5973. For KO: $p < 0.0001$; $r = -0.3699$; number pairs = 5761 (Spearman's
730 correlation). Data shown as mean ± SEM for bar-graphs (B, C) and as violin plots with mean, 25th
731 and 75th percentile (A). *P values* indicated by **ns** for non-significant, *** for *P < 0.001* and ****
732 for *P < 0.0001*.
733
734 **Figure 7-figure supplement 1: TREM2 WT and KO close scratch wound at similar rates.** Scratch
735 closure over 24 hours in WT (grey) and TREM2 KO (green) iPS-microglia with (filled symbols) or
736 without (empty symbols) pre-stimulation of iPSC-microglia with ADP (10 μM, 30 min). N=2
737 wells, 2 images per well. Data shown as mean ± SEM.
738
739
740

Materials and Methods

Key Resources Table

Reagent type (species) or resource	Designation	Source or reference	Identifiers	Additional Information
Cell line (Human)	WT iPSC-microglia	UCI ADRC iPSC Core	ADRC5	iPSC-derived microglial line
Cell line (Human)	TREM2 KO iPSC microglia	Blurton-Jones lab	ADRC5 Clone 28-18	CRISPR-mediated knockout of TREM2 on the WT iPSC line
Cell line (Human)	WT GFP-expressing iPSC-microglia	Coriell	AICS-0036	iPSC-line with GFP tagged to αtubulin. Originally developed by Dr. Bruce Conklin
Cell line (Human)	TREM2 KO GFP-expressing iPSC-microglia	Blurton-Jones lab	GFP Clone 1	CRISPR-mediated knockout of TREM2 on the WT GFP^+ iPSC line
Cell line (Human)	WT RFP-expressing iPSC-microglia	Coriell	AICS-0031-035	iPSC-line with RFP tagged to αtubulin. Originally developed by Dr. Bruce Conklin
Cell line (Human)	TREM2 KO RFP-expressing iPSC-microglia	Blurton-Jones lab	RFP Clone 6	CRISPR-mediated knockout of TREM2 on the WT RFP^+ iPSC line
Cell line (Human)	WT Salsa6f-expressing iPSC-microglia	UCI ADRC iPSC Core	ADRC76 Clone 8	iPSC-line expressing a GCaMP6f-tdTomato fusion construct (Salsa6f)
Cell line (Human)	TREM2 KO Salsa6f-expressing iPSC microglia	Blurton-Jones lab	ADRC76 Clone 8 Clone 98	CRISPR-mediated knockout of TREM2 on the WT $Salsa6f^+$ iPSC line
Cell line (Human)	Orai1 KO iPSC microglia	Blurton-Jones lab	ADRC76	CRISPR-mediated knockout of Orai1 on the WT ADRC76 iPSC line
Plasmid Construct (transgene)	Salsa6f	Addgene	Plasmid# 140188	A genetically encoded Calcium Indicator with tdTomato linked to GCaMP6f by a V5 epitope tag.
Other	DMEM/F12, HEPES, no Phenol red	Thermo Fisher Scientific	11038021	Microglia differentiation cell culture medium
Other	TeSR™-E8™	STEMCELL Technologies	05990	Stem cell culture medium
Other	StemDiff Hematopoietic kit	STEMCELL Technologies	05310	

Peptide/ Recombinant protein	Non-essential amino acids	Gibco	11140035	
Peptide/ Recombinant protein	Glutamax	Gibco	35050061	
Peptide/ Recombinant protein (human)	Insulin	Sigma	I2643	
Peptide/ Recombinant protein	B27	Gibco	17504044	
Peptide/ Recombinant protein	N2	Gibco	A1370701	
Peptide/ Recombinant protein	Insulin-transferrin-selenite	Gibco	41400045	
Peptide/ Recombinant protein (human)	IL-34	Peprotech	200-34	
Peptide/ Recombinant protein (human)	TGFβ1	Peprotech	100-21	
Peptide/ Recombinant protein (human)	M-CSF	Peprotech	300-25	
Peptide/ Recombinant protein	CX3CL1	Peprotech	300-31	
Peptide/ Recombinant protein	CD200	Novoprotein	C311	
Peptide/ Recombinant protein	Fibronectin	STEMCELL Technologies	07159	
Other	Matrigel	Corning	356231	
Other	ReLeSR	STEMCELL Technologies	5872	Human pluripotent stem cell selection and passing reagent
Other	Goat Serum	Thermo Fisher Scientific	10000C	
Other	fluorescent beta-amyloid 1-42 (647)	Anaspec	AS64161	
Other	pHrodo tagged zymosan A beads	Thermo Fisher Scientific	P35364	

Other	pHrodo tagged S. Aureus	Thermo Fisher Scientific	A10010	
Other	Human Stem Cell Nucleofector kit 2	Lonza	VPH-5022	
Other	Alt-R CRISPR-Cas9 tracrRNA	IDTDNA	107253	
Other	Alt-R HiFi Cas9 Nuclease	IDTDNA	1081061	
Antibody	Anti-human IBA1	Wako	019-19741	
Antibody	Goat anti-rabbit 555	Thermo Fisher Scientific	A21429	Secondary antibody
Other	Human TruStain FcX	Biolegend	Cat # 422301	Fc Blocking Solution
Antibody	Brilliant Violet 421 antihuman P2RY12	Biolegend	clone 16001E	Primary antibody
Antibody	Brilliant Violet 421 mouse IgG2a	Biolegend	Clone MOPC-173	κ Isotype control
Chemical compound, drug	Fluo-4 AM	Thermo Fisher Scientific	F14201	
Chemical compound, drug	Fura-red AM	Thermo Fisher Scientific	F3021	
Chemical compound, drug	Pluronic F-127	Thermo Fisher Scientific	P3000MP	
Chemical compound, drug	Cal-520 AM	AAT Bioquest	21130	
Chemical compound, drug	Cal-590 AM	AAT Bioquest	20510	
Chemical compound, drug	ci-IP3/PM	SiChem	6210	Caged-inositol triphosphate analog
Chemical compound, drug	Hoeschst	Thermo Fisher Scientific	R37165	
Chemical compound, drug	ADP	Sigma-Aldrich	A2754	
Chemical compound, drug	ATP	Sigma-Aldrich	A9187	
Chemical compound, drug	UTP	Sigma-Aldrich	U1006	
Chemical compound, drug	PSB 0739	Tocris	3983	
Chemical compound, drug	MRS 2211	Tocris	2402	
Chemical compound, drug	Synta66	Sigma-Aldrich	SML1949	Orai channel inhibitor
Chemical compound, drug	2-APB	Sigma-Aldrich	D9754	
Chemical	Gadolinium	Sigma-Aldrich	G7532	

compound, drug				
Chemical compound, drug	EGTA	Sigma-Aldrich	E8145	
Chemical compound, drug	1-thioglycerol	Sigma-Aldrich	M6145	
Chemical compound, drug	CloneR	STEMCELL Technologies	05888	Defined supplement for single-cell cloning of human iPS cells
Chemical compound, drug	Thiazovivin	STEMCELL Technologies	72252	ROCK inhibitor
Other	35mm glass-bottom dish	MatTek	P35G-1.5-14-C	1.5 coverslip, 14mm glass diameter
Other	Incubation perfusion Lid for 35mm dishes	Tokai Hit	LV200-D35FME	Perfusion lid with inlet and outlet
Other	Laser Scanning Confocal Microscope	Olympus	FV3000	Equipped with Resonant Scanner, IX3-ZDC2 Z-drift compensator, 40x silicone oil objective, 20x air objective
Other	Stage Top Incubation System	Tokai Hit	STXG	Temperature and humidity control for FV3000 microscope stage
Other	Nikon Eclipse T*i* microscope system	Nikon		Equipped with a 40x oil immersion objective (N.A.: 1.3; Nikon) and an Orca Flash 4.0LT CMOS camera (Hamamatsu)
Other	Chemotaxis Assay Chamber	Hansang Cho Lab		
Other	IncuCyte S3 Live-Cell Analysis System	Sartorius		
Other	Essen Incucyte WoundMaker	Sartorius	4493	
Software, algorithm	GraphPad Prism 9.1.0			Data analysis, statistical analysis
Software, algorithm	Fiji (Image J)			Image analysis
Software, algorithm	Incucyte 2020C			Image acquisition and analysis
Software, algorithm	IMARIS 9.7.0			Cell tracking and image analysis
Software, algorithm	Flika			Image analysis
Software, algorithm	DiPer Excel Macros		PMID: 25033209	Data analysis, directional persistence

Generation of iPSCs from human fibroblasts: Human induced pluripotent stem cell lines were generated by the University of California, Irvine Alzheimer's Disease Research Center (UCI ADRC) Induced Pluripotent Stem Cell Core from subject fibroblasts under approved Institutional Review Boards (IRB) and human Stem Cell Research Oversight (hSCRO) committee protocols. Informed consent was received from all participants who donated fibroblasts. Reprogramming was performed with non-integrating sendai virus in order to avoid integration effects. To validate new iPSC lines, cells were karyotyped by G-banding and tested for sterility. Pluripotency was verified by Pluritest Array Analysis and trilineage in vitro differentiation. Additional GFP- and RFP-αtubulin expressing iPSC lines (AICS-0036 and AICS-0031-035) were purchased from Coriell and originally generated by Dr. Bruce Conklin. iPSCs were grown antibiotic free on Matrigel (Corning) in complete mTeSR1 or TeSR-E8 medium (STEMCELL Technologies) in a humidified incubator (5% CO_2, 37° C). All lines will be available upon request to the corresponding author.

CRISPR-mediated knockout of TREM2 and ORAI1: Genome editing to delete TREM2 was performed as in McQuade et al. 2020[41]. Briefly, iPSCs were nucleofected with Ribonucleoprotien complex targeting the second exon of TREM2 and allowed to recover overnight. Transfected cells were dissociated with pre-warmed Accutase then mechanically plated to 96-well plates for clonal expansion. Genomic DNA from each colony was amplified and sequenced at the cut site. The amplification from promising clones was transformed via TOPO cloning for allelic sequencing. Knockout of TREM2 was validated by western blotting

(AF1828, R&D) and HTRF (Cisbio) [41]. A similar strategy was used to delete ORAI1 using an RNP complex of Cas9 protein coupled with a guide RNA (5' CGCTGACCACGACTACCCAC) targeting the second exon of ORAI1. All iPSC lines were confirmed to be sterile and exhibiting a normal Karyotype via Microarray-based Comparative Genomic Hybridization (aCGH, Cell Line Genetics).

iPSC-microglia differentiation: iPSC-microglia were generated as described in [50,51]. Briefly, iPSCs were directed down a hematopoetic lineage using the STEMdiff Hematopoesis kit (STEMCELL Technologies). After 10-12 days in culture, CD43+ hematopoteic progenitor cells are transferred into a microglia differentiation medium containing DMEM/F12, 2× insulin-transferrin-selenite, 2× B27, 0.5× N2, 1× Glutamax, 1× non-essential amino acids, 400 µM monothioglycerol, and 5 µg/mL human insulin. Media was added to cultures every other day and supplemented with 100 ng/mL IL-34, 50 ng/mL TGF-β1, and 25 ng/mL M-CSF (Peprotech) for 28 days. In the final 3 days of differentiation 100 ng/mL CD200 (Novoprotein) and 100 ng/mL CX3CL1 (Peprotech) were added to culture.

Confocal Laser Scanning Microscopy: Unless otherwise stated, cells were imaged on an Olympus FV3000 confocal laser scanning inverted microscope equipped with high-speed resonance scanner, IX3-ZDC2 Z-drift compensator, 40x silicone oil objective (NA 1.25) and a Tokai-HIT stage top incubation chamber (STXG) to maintain cells at 37°C. To visualize Salsa6f, 488 nm and 561 nm diode lasers were used for sequential excitation of GCaMP6f (0.3% laser power, 450V channel voltage, 494-544nm detector width) and TdTomato (0.05% laser power, 450V channel voltage, 580-680nm detector width), respectively. Fluo-4 and Fura-red were both excited using a 488 nm diode laser (0.07% laser power, 500V channel voltage, 494-544nm

detector width for Fluo-4; 0.07% laser power, 550V channel voltage, 580-680nm detector for Fura-Red). Two high-sensitivity cooled GaAsP PMTs were used for detection in the green and red channels respectively. GFP was excited using the same settings as GCaMP6f. Other image acquisition parameters unique to Ca^{2+} imaging, microglia process and cell motility analysis are indicated in the respective sections.

Measurement of intracellular Ca^{2+}:

Cell preparation: iPSC-microglia were plated on fibronectin-coated (5 µg/mL) glass-bottom 35 mm dishes (MatTek, P35G-1.5-14-C) overnight at 60 % confluence. Ratiometric Ca^{2+} imaging was done using Fluo-4 AM and Fura-Red AM dyes as described previously[41]. Briefly, cells were loaded in microglia differentiation medium with 3 µM Fluo-4 AM and 3 µM Fura-Red AM (Molecular Probes) in the presence of Pluronic Acid F-127 (Molecular Probes) for 30 min at room temperature (RT). Cells were washed with medium to remove excess dye and 1 mM Ca^{2+} Ringer's solution was added to the 35 mm dish before being mounted on the microscope for live cell imaging. We note that iPSC-microglia are sensitive to shear forces and produce brief Ca^{2+} signals in response to solution exchange that are dependent on extracellular Ca^{2+}, and that these are more prominent at 37^{o} C. To minimize these confounding effects, cells were imaged at RT and perfusion was performed gently. Salsa6f-expressing iPSC-microglia were prepared for Ca^{2+} imaging in the same way as conventional microglia, but without the dye loading steps. The following buffers were used for Ca^{2+} imaging: (1) 1 or 2 mM Ca^{2+} Ringer solution comprising 155 mM NaCl, 4.5 mM KCl, 1 mM $CaCl_2$, 0.5 mM $MgCl_2$, 10 mM glucose, and 10 mM HEPES (pH adjusted to 7.4 with NaOH), (2) Ca^{2+}-free Ringer solution containing: 155 mM NaCl, 4.5 mM KCl,

1.5 mM $MgCl_2$, 10 mM glucose, 1 mM EGTA, 10 mM HEPES, pH 7.4. Live cell imaging was performed as described earlier. Cells were treated with ADP as indicated in the results section.

Data acquisition: Time-lapse images were acquired in a single Z-plane at 512 x 512 pixels (X = 318.2 µm and Y = 318.2 µm) and at 2-3 sec time intervals using Olympus FV3000 software. Images were time averaged over 3 frames to generate a rolling average and saved as .OIR files.

Data analysis: Time-lapse videos were exported to Fiji- ImageJ (https://imagej.net/Fiji), converted to tiff files (16-bit) and background subtracted. Single-cell analysis was performed by drawing ROIs around individual cells in the field and average pixel intensities in the green and red channels were calculated for each ROI at each time-point. GCaMP6f/ TdTomato (G/R Ratio) and Fluo-4/Fura-Red ratio was then obtained to further generate traces showing single-cell and average changes in cytosolic Ca^{2+} over time. Single-cell ratio values was used to calculate Peak Ca^{2+} signal and responses at specific time points after agonist application as previously reported[60]. Peak Ca^{2+} signal for each cell was baseline subtracted, which was calculated as an average of 10 minimum ratio values before application of agonist. SOCE rate was calculated as Δ(Ratio)/ Δt (sec^{-1}) over a 10-sec time frame of maximum initial rise after Ca^{2+} add-back. Area under the curve (AUC) was calculated using the AUC function in GraphPad Prism.

Microglia process extension analysis:

Data acquisition: GFP-expressing iPSC-microglia were plated overnight on 35 mm glass bottom dishes at 40-50% confluence. Cells were imaged by excitation of GFP on the confocal microscope at 37^{o} C as described earlier. To study process extension in response to ADP, two sets of GFP images were obtained for each field of view across multiple dishes: before addition of ADP (baseline) and 30 min after application of ADP. Images were acquired as a Z-stack using

the Galvo scanner at Nyquist sampling. Adjacent fields of view were combined using the Stitching function of the Olympus FV3000 Software and saved as .OIR files.

Process Analysis: The basic workflow for microglia process analysis was adapted from Morrison et al, Sci. Rep, 2017 [72]. Image stacks (.OIR files) were exported to Fiji- Image J and converted into 16-bit Tiff files using the Olympus Viewer Plugin (https://imagej.net/OlympusImageJPlugin). Maximum intensity projection (MIP) image from each Z-stack was used for further processing and analysis. MIP images were converted to 8-bit grey scale images, to which a threshold was applied to obtain 8-bit binary images. The same threshold was used for all sets of images, both before and after ADP application. Noise reduction was performed on the binary images using the Process -> Noise -> Unspeckle function. Outlier pixels were eliminated using Process -> Noise -> Outliers function. The binary images were then skeletonized using the Skeletonize2D/3D Plugin for Image J (https://imagej.net/plugins/skeletonize3d). Sparingly, manual segmentation was used to separate a single skeleton that was part of two cells touching each other. The Analyze Skeleton Plugin (https://imagej.net/plugins/analyze-skeleton/) was then applied to the skeletonized images to obtain parameters related to process length and number of branches for each cell in the imaging field. Processes were considered to be skeletons > 8 µm. The data was summarized as average process length and number of branches, before and after ADP application for a specific imaging field, normalized to the number of cells in the field which allowed for pairwise comparison. Additionally, single cell data across all experiments were also compared in some instances.

IP_3 uncaging: Whole-field uncaging of i-IP_3, a poorly metabolized IP_3 analog, was performed as previously described [73] with minor modifications. Briefly, iPSC-microglia were loaded for 20 min at 37° C with either Cal520 AM or Cal590 AM (5 µM, AAT Bioquest), and the cell permeable, caged i-IP_3 analog ci-IP_3/PM (1 µM, SiChem) plus 0.1% Pluronic F-127 in Microglia Basal Medium. Cells were washed and incubated in the dark for further 30 min in a HEPES-buffered salt solution (HBSS) whose composition was (in mM): 135 NaCl, 5.4 KCl, 1.0 MgCl2, 10 HEPES, 10 glucose, 2.0 $CaCl_2$, and pH 7.4. Intracellular Ca^{2+} ($[Ca^{2+}]_i$) changes were imaged by employing a Nikon Eclipse T*i* microscope system (Nikon) equipped with a 40x oil immersion objective (N.A.: 1.3; Nikon) and an Orca Flash 4.0LT CMOS camera (Hamamatsu). Cal520 or Cal590 were excited by a 488 or a 560 nm laser light source (Vortran Laser Technologies), respectively. i-IP3 uncaging was achieved by uniformly exposing the imaged cells to a single flash of ultraviolet (UV) light (350-400 nm) from a Xenon arc lamp. UV flash duration, and thus the amount of released i-IP_3, was set by an electronically controlled shutter.

Image acquisition was performed by using Nikon NIS (Nikon) software. After conversion to stack tiff files, image sequences were analyzed with Flika, a custom-written Python-based imaging analysis software (https://flika-org.github.io/; [74]). After background subtraction, either Cal520 or Cal590 fluorescence changes of each cell were expressed as $\Delta F/F_0$, where F_0 is the basal fluorescence intensity and ΔF the relative fluorescence change ($F_x - F_0$). Data are reported as superplots [75] of at least three independent replicates. Experiments were reproduced with two independent lines. Comparisons were performed by unpaired non-parametric t-test.

Immunocytochemistry: Cells were fixed with 4 % paraformaldehyde for 7 min and washed 3x with 1X PBS. Blocking was performed at room temp for 1 hr in 5 % Goat Serum, 0.1 % Triton5 X-

100. Primary antibodies were added at 1:200 overnight 4° C (IBA1, 019-19741, FUJIFILM Wako). Plates were washed 3x before addition of secondary antibodies (Goat anti-Rabbit 555, ThermoFisher Scientific) and Hoechst (ThermoFisher Scientific). Images were captured on an Olympus FV3000RS confocal microscope with identical laser and detection settings. Images were analyzed with IMARIS 9.7.0 software.

Flow Cytometry iPSC-derived microglia were seeded on fibronectin-coated 12-well plates at 200,000 cells/well. Cells were harvested and centrifuged in FACS tubes at 300 xG for 5 min at 4° C. The cell pellet was subsequently resuspended in FACS buffer (1X PBS + 0.5% FBS). Fc receptors were blocked with a blocking buffer (Bio-legend TruStain FcX in 1X PBS + 10% FCS). Cells were then incubated with Brilliant Violet 421-labelled anti-human $P2Y_{12}$ receptor antibody (clone S16001E, Biolegend, Cat# 392106) or with IgG2a isotype control antibody (clone MOPC-173, Biolegend, Cat# 400260) for 30 min at 4° C. Cells were washed, pelleted, and then resuspended in FACS buffer. Clone S16001E binds to the extracellular domain of the $P2Y_{12}$ and permits labeling of plasma membrane $P2Y_{12}$ receptors. Data were acquired using Novocyte Quanteon flow cytometer (Agilent) and analyzed using FlowJo analysis software (FlowJo v10.8.1 LLC Ashland, Oregon).

Scratch wound assay: Nondirectional motility was analyzed using Essen Incucyte WoundMaker. iPSC-microglia were plated on fibronectin (STEMCELL Technologies) at 90% confluence. Scratches were repeated 4x to remove all cells from the wound area. Scratch wound confluency was imaged every hour until scratch wound was closed (15 hrs). Confluence of cells within the original wound ROI was calculated using IncuCyte 2020C software.

IMARIS Cell Tracking: For motility assays, iPSC-microglia were tracked using a combination of manual and automatic tracking in IMARIS 9.7.0 software. For videos of GFP lines, cells were tracked using spot identification. For videos of Salsa6f lines, surface tracking was used to determine ratiometric Ca^{2+} fluorescence and motility per cell. In both conditions, tracks were defined by Brownian motion with the maximum distance jump of 4 microns and 10 frame disturbance with no gap filling. Tracks shorter than 3 minutes in length were eliminated from analysis. After automated track formation, tracks underwent manual quality control to eliminate extraneous tracks, merge falsely distinct tracks, and add missed tracks. After export, data was plotted in Prism 9.1.0 or analyzed in excel using DiPer macros for Plot_At_Origin (translation of each trajectory to the origin) and mean squared distance (MSD) MSD(t)=4D(t-P(1-e^(-t/P))) where D is the diffusion coefficient, t is time, and P represents directional persistence time (time to cross from persistent directionality to random walk)[62]. From IMARIS, speed was calculated as instantaneous speed of the object (μm/s) as the scalar equivalent to object velocity. These values were transformed to μm /min as this time scale is more relevant for the changes we observed. Mean track speed represents the mean of all instantaneous speeds over the total time of tracking. 10 min displacement is calculated by (600) * (TDL/TD), where TDL = track displacement length (distance between the first and last cell position) represented as TDL= p(n) - p(1) for all axes where the vector p is the distance between the first and last object position along the selected axis and TD = track duration represented as TD = T(n) - T(1), where T is the timepoint of the first and final timepoint within the track. Frame-to-frame displacement is calculated as p(n) – p(n-1) for all the different frames in a cell track. Track straightness is defined as TDL/TL where TDL = track displacement as described above and TL =

track length representing the total length of displacements within the track TL= sum from t=2 to n of |p(t)-p(t-1)|.

Generation of Salsa6f-expressing iPSC lines: iPSCs were collected following Accutase enzymatic digestion for 3 min at 37° C. 20,000 cells were resuspended in 100 µL nucleofection buffer from Human Stem Cell Nucleofector™ Kit 2 (Lonza). Salsa6f-AAVS1 SHL plasmid Template (2 µg; Vector Builder) and RNP complex formed by incubating Alt-R® S.p. HiFi Cas9 Nuclease V3 (50 µg; IDTDNA) was fused with crRNA:tracrRNA (IDTDNA) duplex for 15 min at 23° C. This complex was combined with the cellular suspension and nucleofected using the Amaxa Nucleofector program B-016. To recover, cells were plated in TeSR™-E8™ (STEMCELL Technologies) media with 0.25 µM Thiazovivin (STEMCELL Technologies) and CloneR™ (STEMCELL Technologies) overnight. The following day, cells were mechanically replated to 96-well plates in TeSR™-E8™ media with 0.25 µM Thiazovivin and CloneR™ supplement for clonal isolation and expansion. Plates were screened visually with a fluorescence microscope to identify TdTomato^{+} clones. Genomic DNA was extracted from positive clones using Extracta DNA prep for PCR (Quantabio) and amplified using Taq PCR Master Mix (Thermo Fisher Scientific) to confirm diallelic integration of the Salsa6f cassette. A clone confirmed with diallelic Salsa6f integration in the AAVS1 SHL was then retargeted as previously described[41] to knock-out Trem2.

Phagocytosis assay: Phagocytosis of transgenic iPSC-microglia was validated using IncuCyte S3 Live-Cell Analysis System (Sartorius) as in McQuade et al. 2020[41]. Microglia were plated at 50% confluency 24 hours before substrates were added. Cells were treated with 50 µg/mL pHrodo tagged human AD synaptosomes (isolated as described in McQuade et al. 2020), 100 ng/mL pHrodo tagged zymosan A beads (Thermo Fisher Scientific), 100 ng/mL pHrodo tagged S.

Aureus (Thermo Fisher Scientific), or 2 µg/mL fluorescent beta-amyloid (Anaspec). Image masks for fluorescence area and phase were generated using IncuCyte 2020C software.

Chemotaxis assay: iPSC-microglia were loaded into the angular chamber (2-5K cells/device) to test activation and chemotaxis towards the central chamber containing either ADP (100 ng/mL or 234 nM) or vehicle. When noted, PSB 0739 (10 µM) was added to both the central and angular chamber to inhibit $P2Y_{12}$ receptors. To characterize motility, we monitored the number of recruited microglia in the central chamber for 4 days under the fully automated Nikon TiE microscope (10× magnification; Micro Device Instruments, Avon, MA, USA).

Statistical Analysis

GraphPad Prism (Version 6.01 and 8.2.0) was used to perform statistical tests and generate P values. We used standard designation of P values throughout the Figures (**ns**, not significant or *P ≥ 0.05*; * *P < 0.05*; ** *P < 0.01*; *** *P < 0.001*; **** *P < 0.0001*). Traces depicting average changes in cytosolic Ca^{2+} over time are shown as mean ± SEM (Standard Error of Mean). Accompanying bar-graphs with bars depicting mean ± SEM (Standard Error of Mean) provide a summary of relevant parameters (Amplitude of Ca^{2+} response, degree of store-release, rate of Ca^{2+} influx etc) as indicated. Details of number of replicates and the specific statistical test used are provided in the individual figure legends.

Acknowledgements

The authors would like to thank Dr. Andy Yeromin for the development of Excel macros to analyze IMARIS cell tracking. The authors would also like to thank Morgan Coburn for sharing python scripts that aided in the organization of IMARIS output files. This work was supported by

T32 NS082174 and ARCS foundation (A.M.); the European Union's Horizon 2020 research and innovation program under the Marie Sklodowska-Curie grant agreement iMIND – No. 84166 (A.G.); NIH R01 NS14609 and AI121945 (M.D.C.); NIH U01 AI160397 (S.O.); NRF 2020R1A2C2010285, 2020M3C7A1023941, and NIH AG059236-01A1 (H.C.); NIH AG048099, AG056303, and AG055524 (M.B.J.); RF1DA048813 (M.B.J. and S.G.); UCI Sue & Bill Gross Stem Cell Research Center Seed Grant (S.G.); and a generous gift from the Susan Scott Foundation (M.B.J.). iPSC lines were generated by the UCI-ADRC iPS cell core funded by NIH AG066519. Experiments using the GFP-expressing iPSC line AICS-0036 were made possible through the Allen Cell Collection, available from Coriell Institute for Medical Research.

Declaration of interest: M.B.J. is a co-inventor of patent application WO/2018/160496, related to the differentiation of pluripotent stem cells into microglia. M.B.J and S.P.G. are co-founders of NovoGlia Inc.

Ethics: Human iPSC lines were generated by the University of California Alzheimer's Disease Research Center (UCI ADRC) stem cell core. Subject fibroblasts were collected under approved Institutional Review Boards (IRB) and human Stem Cell Research Oversight (hSCRO) committee protocols. Informed consent was received for all participants.

Data Availability: RNA sequencing data referenced in Figure 1- figure supplement 2 is available through Gene Expression Omnibus: GSE157652. Any additional data presented in this paper will be available from the authors upon request.

References

1. Andersen, M. S. *et al.* Heritability Enrichment Implicates Microglia in Parkinson's Disease Pathogenesis. *Annals of Neurology* **89**, 942–951 (2021).
2. Crotti, A. *et al.* Mutant Huntingtin promotes autonomous microglia activation via myeloid lineage-determining factors. *Nat Neurosci* **17**, 513–521 (2014).
3. Fahira, A., Li, Z., Liu, N. & Shi, Y. Prediction of causal genes and gene expression analysis of attention-deficit hyperactivity disorder in the different brain region, a comprehensive integrative analysis of ADHD. *Behav Brain Res* **364**, 183–192 (2019).
4. Jansen, I. E. *et al.* Genome-wide meta-analysis identifies new loci and functional pathways influencing Alzheimer's disease risk. *Nat. Genet.* (2019) doi:10.1038/s41588-018-0311-9.
5. McQuade, A. & Blurton-Jones, M. Microglia in Alzheimer's disease: Exploring how genetics and phenotype influence risk. *J Mol Biol* **431**, 1805–1817 (2019).
6. Pimenova, A. A. *et al.* Alzheimer's-associated PU.1 expression levels regulate microglial inflammatory response. *Neurobiol Dis* 105217 (2020) doi:10.1016/j.nbd.2020.105217.
7. Tan, L. *et al.* Association of GWAS-linked loci with late-onset Alzheimer's disease in a northern Han Chinese population. *Alzheimers Dement* **9**, 546–553 (2013).
8. Davalos, D. *et al.* ATP mediates rapid microglial response to local brain injury in vivo. *Nat. Neurosci.* **8**, 752–758 (2005).
9. De Simone, R. *et al.* TGF-β and LPS modulate ADP-induced migration of microglial cells through P2Y1 and P2Y12 receptor expression. *J. Neurochem.* **115**, 450–459 (2010).
10. Honda, S. *et al.* Extracellular ATP or ADP Induce Chemotaxis of Cultured Microglia through Gi/o-Coupled P2Y Receptors. *J. Neurosci.* **21**, 1975–1982 (2001).

11. Koizumi, S. *et al.* UDP acting at P2Y6 receptors is a mediator of microglial phagocytosis. *Nature* **446**, 1091–1095 (2007).

12. Haynes, S. E. *et al.* The P2Y12 receptor regulates microglial activation by extracellular nucleotides. *Nat Neurosci* **9**, 1512–1519 (2006).

13. Yegutkin, G. G. Nucleotide- and nucleoside-converting ectoenzymes: Important modulators of purinergic signalling cascade. *Biochim Biophys Acta* **1783**, 673–694 (2008).

14. Dissing-Olesen, L. *et al.* Activation of neuronal NMDA receptors triggers transient ATP-mediated microglial process outgrowth. *J Neurosci* **34**, 10511–10527 (2014).

15. Madry, C. & Attwell, D. Receptors, ion channels, and signaling mechanisms underlying microglial dynamics. *J Biol Chem* **290**, 12443–12450 (2015).

16. Zhang, Y. *et al.* An RNA-Sequencing Transcriptome and Splicing Database of Glia, Neurons, and Vascular Cells of the Cerebral Cortex. *J. Neurosci.* **34**, 11929–11947 (2014).

17. Prakriya, M. & Lewis, R. S. Store-Operated Calcium Channels. *Physiol Rev* **95**, 1383–1436 (2015).

18. McLarnon, J. G. Microglial Store-operated Calcium Signaling in Health and in Alzheimer's Disease. *Curr Alzheimer Res* **17**, 1057–1064 (2020).

19. Mizuma, A. *et al.* Microglial Calcium Release-Activated Calcium Channel Inhibition Improves Outcome from Experimental Traumatic Brain Injury and Microglia-Induced Neuronal Death. *J Neurotrauma* **36**, 996–1007 (2019).

20. Gilbert, D. F. *et al.* Store-Operated Ca2+ Entry (SOCE) and Purinergic Receptor-Mediated Ca2+ Homeostasis in Murine bv2 Microglia Cells: Early Cellular Responses to ATP-Mediated Microglia Activation. *Front Mol Neurosci* **9**, 111 (2016).

1026 21. Hasselmann, J. *et al.* Development of a Chimeric Model to Study and Manipulate Human
1027 Microglia In Vivo. *Neuron* (2019) doi:10.1016/j.neuron.2019.07.002.
1028 22. Keren-Shaul, H. *et al.* A Unique Microglia Type Associated with Restricting Development
1029 of Alzheimer's Disease. *Cell* **0**, (2017).
1030 23. Krasemann, S. *et al.* The TREM2-APOE Pathway Drives the Transcriptional Phenotype of
1031 Dysfunctional Microglia in Neurodegenerative Diseases. *Immunity* **47**, 566-581.e9 (2017).
1032 24. Olah, M. *et al.* Single cell RNA sequencing of human microglia uncovers a subset associated
1033 with Alzheimer's disease. *Nature Communications* **11**, 6129 (2020).
1034 25. Sala Frigerio, C. *et al.* The Major Risk Factors for Alzheimer's Disease: Age, Sex, and
1035 Genes Modulate the Microglia Response to Aβ Plaques. *Cell Rep* **27**, 1293-1306.e6 (2019).
1036 26. Weisman, G. A., Woods, L. T., Erb, L. & Seye, C. I. P2Y receptors in the mammalian
1037 nervous system: pharmacology, ligands and therapeutic potential. *CNS Neurol Disord Drug*
1038 *Targets* **11**, 722–738 (2012).
1039 27. Cserép, C. *et al.* Microglia monitor and protect neuronal function through specialized
1040 somatic purinergic junctions. *Science* **367**, 528–537 (2020).
1041 28. Suzuki, T. *et al.* Extracellular ADP augments microglial inflammasome and NF-κB
1042 activation via the P2Y12 receptor. *European Journal of Immunology* **50**, 205–219 (2020).
1043 29. Wu, Y. *et al.* Aberrant expression of long noncoding RNAs in the serum and myocardium of
1044 spontaneous hypertensive rats. *Mol Biol Rep* **46**, 6399–6404 (2019).
1045 30. Eyo, U. B. *et al.* Neuronal hyperactivity recruits microglial processes via neuronal NMDA
1046 receptors and microglial P2Y12 receptors after status epilepticus. *J Neurosci* **34**, 10528–
1047 10540 (2014).

1048 31. Lou, N. *et al.* Purinergic receptor P2RY12-dependent microglial closure of the injured
1049 blood–brain barrier. *PNAS* **113**, 1074–1079 (2016).
1050 32. Bisht, K. *et al.* Capillary-associated microglia regulate vascular structure and function
1051 through PANX1-P2RY12 coupling in mice. *Nat Commun* **12**, 5289 (2021).
1052 33. Leissring, M. A. *et al.* Capacitative calcium entry deficits and elevated luminal calcium
1053 content in mutant presenilin-1 knockin mice. *J Cell Biol* **149**, 793–798 (2000).
1054 34. Brawek, B. *et al.* Impairment of in vivo calcium signaling in amyloid plaque-associated
1055 microglia. *Acta Neuropathol* **127**, 495–505 (2014).
1056 35. Demuro, A., Parker, I. & Stutzmann, G. E. Calcium Signaling and Amyloid Toxicity in
1057 Alzheimer Disease. *J Biol Chem* **285**, 12463–12468 (2010).
1058 36. Mustaly, S., Littlefield, A. & Stutzmann, G. E. Calcium Signaling Deficits in Glia and
1059 Autophagic Pathways Contributing to Neurodegenerative Disease. *Antioxid. Redox Signal.*
1060 (2018) doi:10.1089/ars.2017.7266.
1061 37. Eichhoff, G., Brawek, B. & Garaschuk, O. Microglial calcium signal acts as a rapid sensor of
1062 single neuron damage in vivo. *Biochim Biophys Acta* **1813**, 1014–1024 (2011).
1063 38. Irino, Y., Nakamura, Y., Inoue, K., Kohsaka, S. & Ohsawa, K. Akt activation is involved in
1064 P2Y12 receptor-mediated chemotaxis of microglia. *J Neurosci Res* **86**, 1511–1519 (2008).
1065 39. Milior, G. *et al.* Distinct P2Y Receptors Mediate Extension and Retraction of Microglial
1066 Processes in Epileptic and Peritumoral Human Tissue. *J Neurosci* **40**, 1373–1388 (2020).
1067 40. Cheng-Hathaway, P. J. *et al.* The Trem2 R47H variant confers loss-of-function-like
1068 phenotypes in Alzheimer's disease. *Mol Neurodegener* **13**, 29 (2018).

41. McQuade, A. *et al.* Gene expression and functional deficits underlie TREM2-knockout microglia responses in human models of Alzheimer's disease. *Nature Communications* **11**, 5370 (2020).

42. Ulrich, J. D. *et al.* Altered microglial response to Aβ plaques in APPPS1-21 mice heterozygous for TREM2. *Mol Neurodegener* **9**, 20 (2014).

43. Andrews, S. J., Fulton-Howard, B. & Goate, A. Interpretation of risk loci from genome-wide association studies of Alzheimer's disease. *Lancet Neurol* (2020) doi:10.1016/S1474-4422(19)30435-1.

44. Karch, C. M. *et al.* Expression of Novel Alzheimer's Disease Risk Genes in Control and Alzheimer's Disease Brains. *PLOS ONE* **7**, e50976 (2012).

45. Cheng, Q. *et al.* TREM2-activating antibodies abrogate the negative pleiotropic effects of the Alzheimer's disease variant Trem2R47H on murine myeloid cell function. *J. Biol. Chem.* **293**, 12620–12633 (2018).

46. Gratuze, M. *et al.* Impact of TREM2^{R47H} variant on tau pathology–induced gliosis and neurodegeneration. *J Clin Invest* **130**, 4954–4968 (2020).

47. Götzl, J. K. *et al.* Opposite microglial activation stages upon loss of PGRN or TREM2 result in reduced cerebral glucose metabolism. *EMBO Mol Med* **11**, e9711 (2019).

48. Griciuc, A. *et al.* TREM2 Acts Downstream of CD33 in Modulating Microglial Pathology in Alzheimer's Disease. *Neuron* **103**, 820-835.e7 (2019).

49. Abud, E. M. *et al.* iPSC-Derived Human Microglia-like Cells to Study Neurological Diseases. *Neuron* **94**, 278-293.e9 (2017).

50. McQuade, A. *et al.* Development and validation of a simplified method to generate human microglia from pluripotent stem cells. *Molecular Neurodegeneration* **13**, 67 (2018).

1092 51. McQuade, A. & Blurton-Jones, M. Human Induced Pluripotent Stem Cell-Derived Microglia
1093 (hiPSC-Microglia). *Methods Mol Biol* (2021) doi:10.1007/7651_2021_429.
1094 52. Andreone, B. J. *et al.* Alzheimer's-associated PLCγ2 is a signaling node required for both
1095 TREM2 function and the inflammatory response in human microglia. *Nature Neuroscience*
1096 1–12 (2020) doi:10.1038/s41593-020-0650-6.
1097 53. Cosker, K. *et al.* Microglial signalling pathway deficits associated with the patient derived
1098 R47H TREM2 variants linked to AD indicate inability to activate inflammasome. *Sci Rep*
1099 **11**, 13316 (2021).
1100 54. Konttinen, H. *et al.* PSEN1ΔE9, APPswe, and APOE4 Confer Disparate Phenotypes in
1101 Human iPSC-Derived Microglia. *Stem Cell Reports* (2019)
1102 doi:10.1016/j.stemcr.2019.08.004.
1103 55. Piers, T. M. *et al.* A locked immunometabolic switch underlies TREM2 R47H loss of
1104 function in human iPSC-derived microglia. *FASEB J.* (2019) doi:10.1096/fj.201902447R.
1105 56. You, Y. *et al.* Human neural cell type-specific extracellular vesicle proteome defines disease-
1106 related molecules associated with activated astrocytes in Alzheimer's disease brain. *J*
1107 *Extracell Vesicles* **11**, e12183 (2022).
1108 57. Michaelis, M., Nieswandt, B., Stegner, D., Eilers, J. & Kraft, R. STIM1, STIM2, and Orai1
1109 regulate store-operated calcium entry and purinergic activation of microglia. *Glia* **63**, 652–
1110 663 (2015).
1111 58. Visentin, S., Nuccio, C. D. & Bellenchi, G. C. Different patterns of Ca^{2+} signals are induced
1112 by low compared to high concentrations of P2Y agonists in microglia. *Purinergic Signal* **2**,
1113 605–617 (2006).

59. Dong, T. X. *et al.* T-cell calcium dynamics visualized in a ratiometric tdTomato-GCaMP6f transgenic reporter mouse. *eLife* **6**, e32417 (2017).

60. Jairaman, A. & Cahalan, M. D. Calcium Imaging in T Lymphocytes: a Protocol for Use with Genetically Encoded or Chemical Ca2+ Indicators. *Bio Protoc* **11**, e4170 (2021).

61. Borges, P. A. *et al.* Adenosine Diphosphate Improves Wound Healing in Diabetic Mice Through P2Y12 Receptor Activation. *Front. Immunol.* **12**, (2021).

62. Gorelik, R. & Gautreau, A. Quantitative and unbiased analysis of directional persistence in cell migration. *Nature Protocols* **9**, 1931–1943 (2014).

63. Negulescu, P. A., Krasieva, T. B., Khan, A., Kerschbaum, H. H. & Cahalan, M. D. Polarity of T cell shape, motility, and sensitivity to antigen. *Immunity* **4**, 421–430 (1996).

64. Liang, C.-C., Park, A. Y. & Guan, J.-L. In vitro scratch assay: a convenient and inexpensive method for analysis of cell migration in vitro. *Nat Protoc* **2**, 329–333 (2007).

65. Park, J. *et al.* A 3D human triculture system modeling neurodegeneration and neuroinflammation in Alzheimer's disease. *Nat. Neurosci.* **21**, 941–951 (2018).

66. Meilandt, W. J. *et al.* Trem2 deletion reduces late-stage amyloid plaque accumulation, elevates the Aβ42:Aβ40 ratio, and exacerbates axonal dystrophy and dendritic spine loss in the PS2APP Alzheimer's mouse model. *J. Neurosci.* (2020) doi:10.1523/JNEUROSCI.1871-19.2019.

67. Ilina, O. & Friedl, P. Mechanisms of collective cell migration at a glance. *J Cell Sci* **122**, 3203–3208 (2009).

68. Lim, H. M. *et al.* UDP-Induced Phagocytosis and ATP-Stimulated Chemotactic Migration Are Impaired in STIM1-/- Microglia In Vitro and In Vivo. *Mediators Inflamm* **2017**, 8158514 (2017).

1137 69. S, P. *et al.* Loss of TREM2 Function Increases Amyloid Seeding but Reduces Plaque-
1138 Associated ApoE. *Nature neuroscience* vol. 22
1139 https://pubmed.ncbi.nlm.nih.gov/30617257/?from_single_result=30617257&expanded_searc
1140 h_query=30617257 (2019).
1141 70. Alector Inc. *A Phase 2 Randomized, Double-Blind, Placebo-Controlled, Multicenter Study to*
1142 *Evaluate the Efficacy and Safety of AL002 in Participants With Early Alzheimer's Disease*.
1143 https://clinicaltrials.gov/ct2/show/NCT04592874 (2021).
1144 71. Wang, S. *et al.* Anti-human TREM2 induces microglia proliferation and reduces pathology
1145 in an Alzheimer's disease model. *J Exp Med* **217**, (2020).
1146 72. Morrison, H., Young, K., Qureshi, M., Rowe, R. K. & Lifshitz, J. Quantitative microglia
1147 analyses reveal diverse morphologic responses in the rat cortex after diffuse brain injury. *Sci*
1148 *Rep* **7**, 13211 (2017).
1149 73. Lock, J. T., Parker, I. & Smith, I. F. Communication of Ca(2+) signals via tunneling
1150 membrane nanotubes is mediated by transmission of inositol trisphosphate through gap
1151 junctions. *Cell Calcium* **60**, 266–272 (2016).
1152 74. Ellefsen, K. L., Settle, B., Parker, I. & Smith, I. F. An algorithm for automated detection,
1153 localization and measurement of local calcium signals from camera-based imaging. *Cell*
1154 *Calcium* **56**, 147–156 (2014).
1155 75. Lord, S. J., Velle, K. B., Mullins, R. D. & Fritz-Laylin, L. K. SuperPlots: Communicating
1156 reproducibility and variability in cell biology. *J Cell Biol* **219**, (2020).
1157
1158

1159 **Insert Figures with captions (not complete legends) here for the pdf file.**

Figure 1

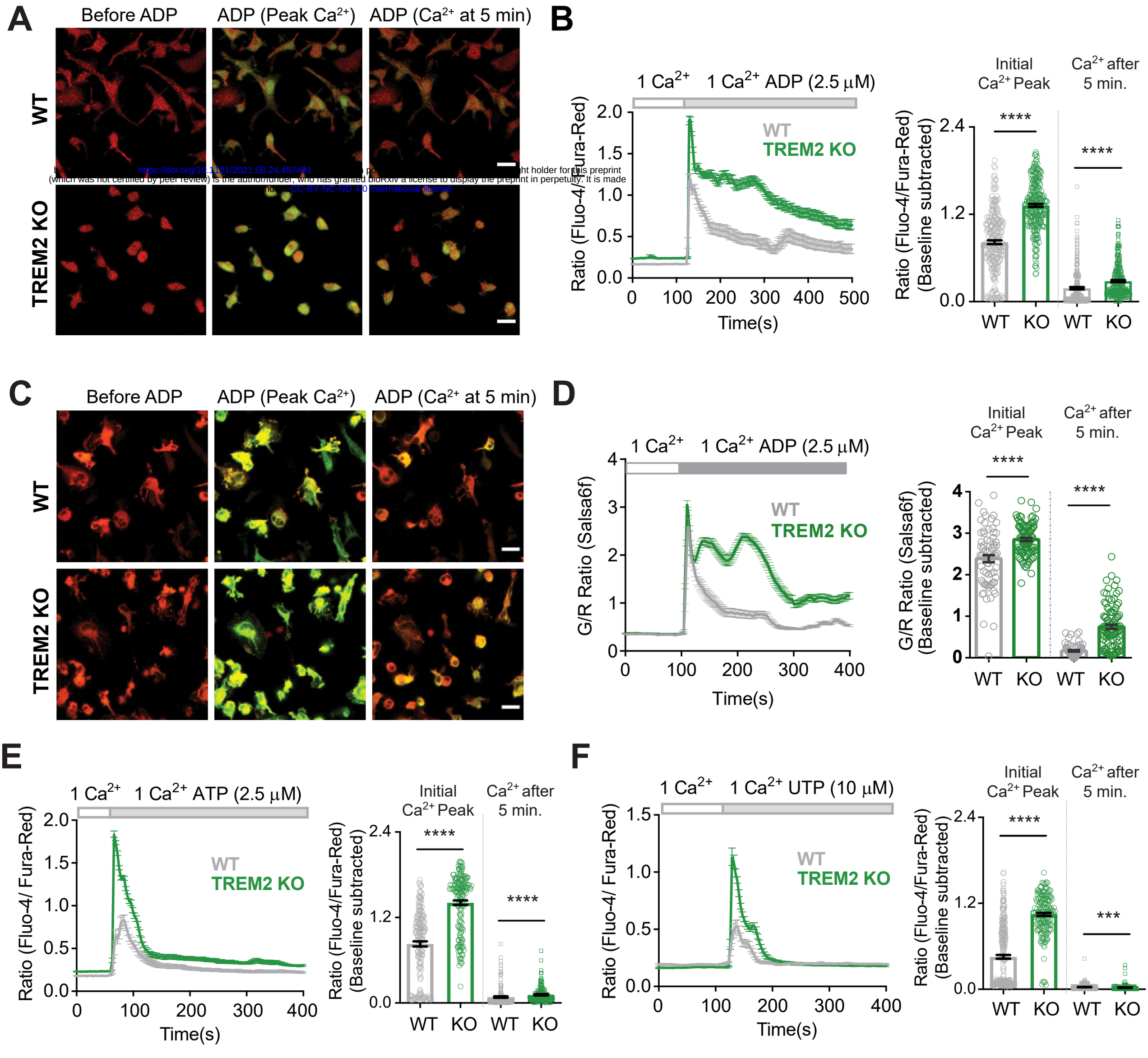

Figure 1-figure supplement 1

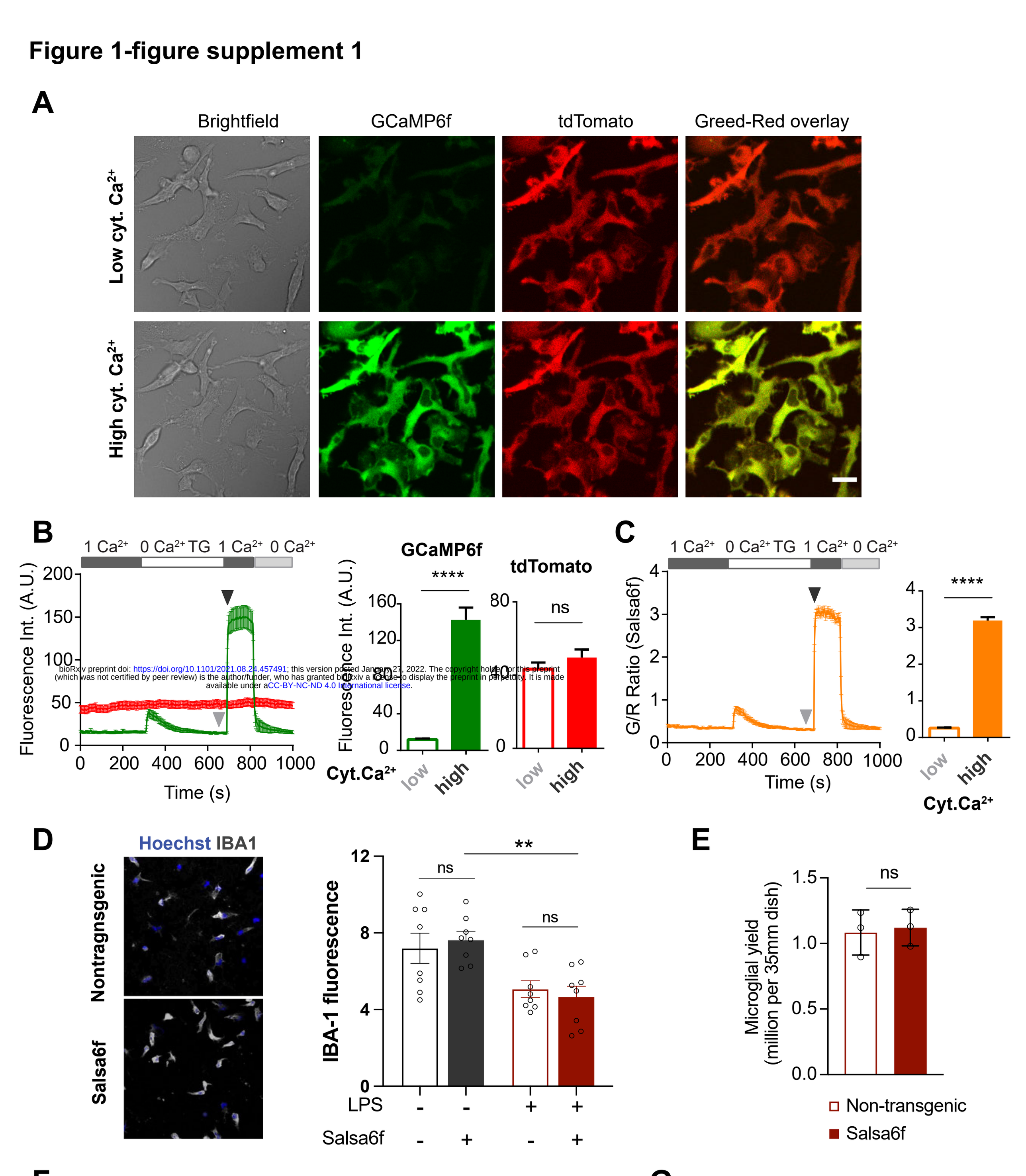

Figure 1-figure supplement 2

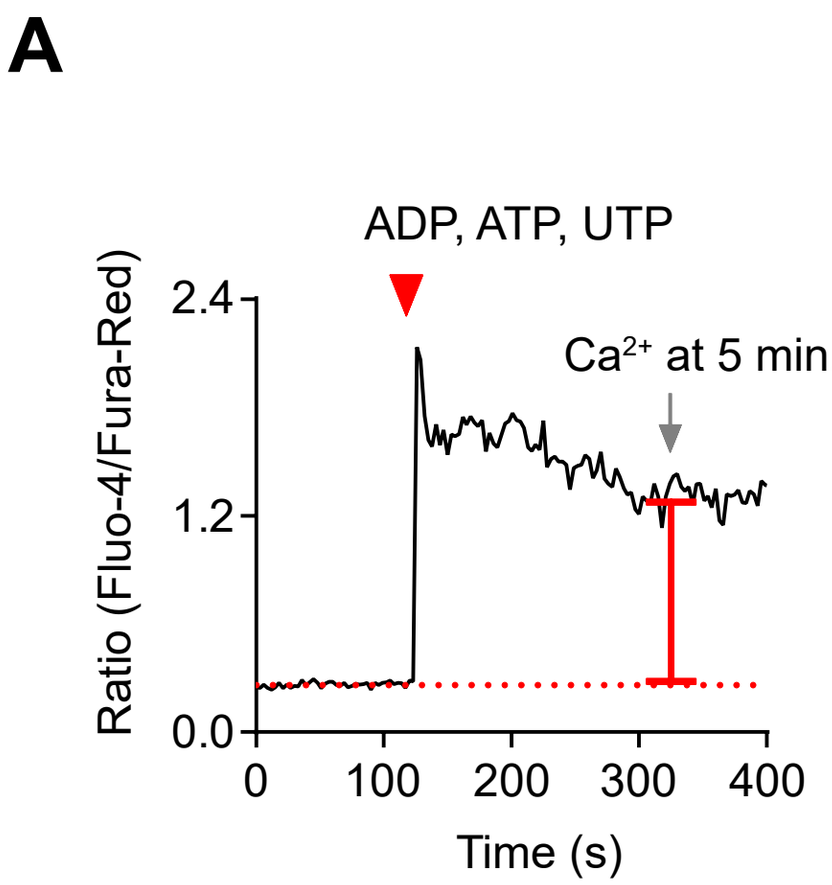

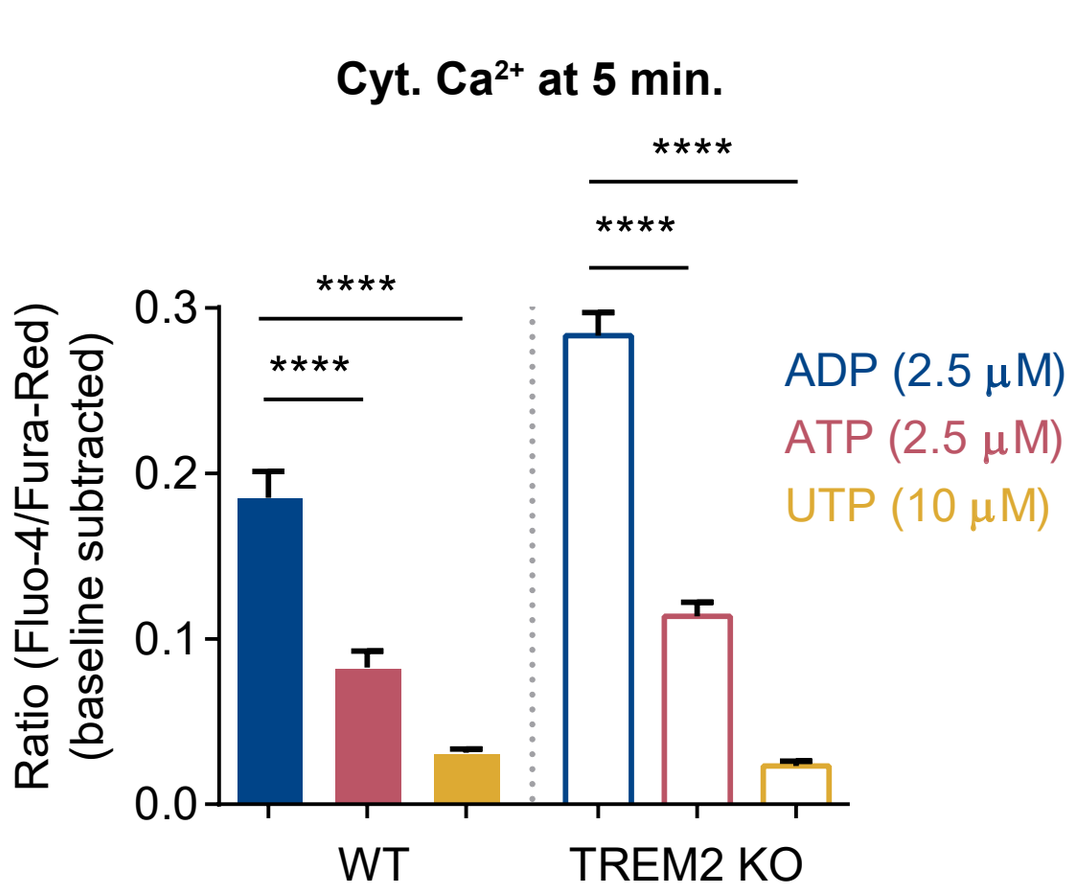

Figure 2

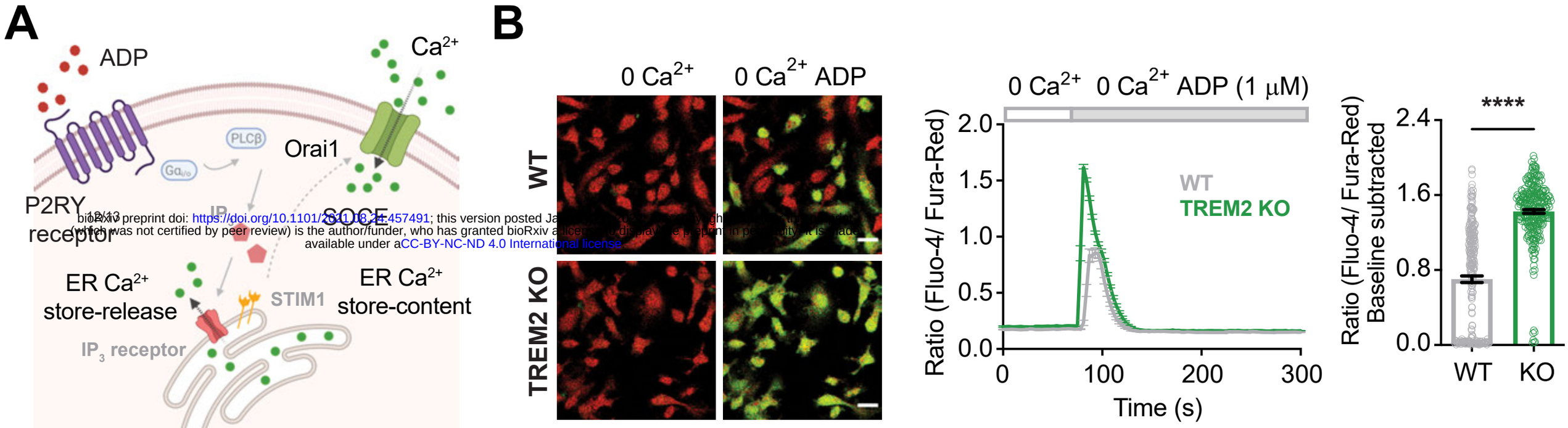

Dose Curve: WT TREM2 KO

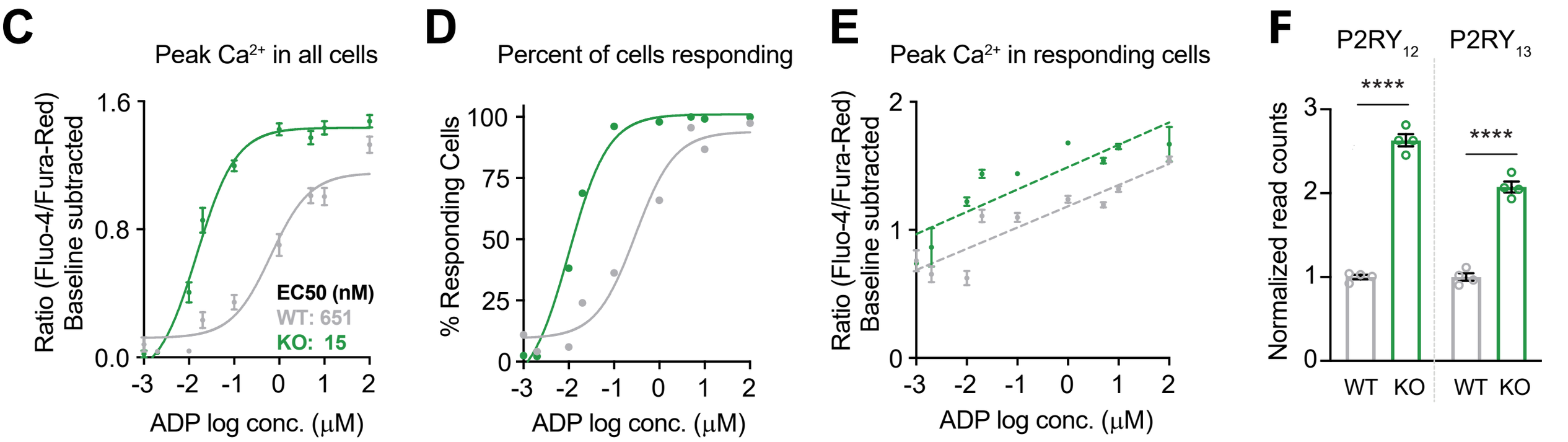

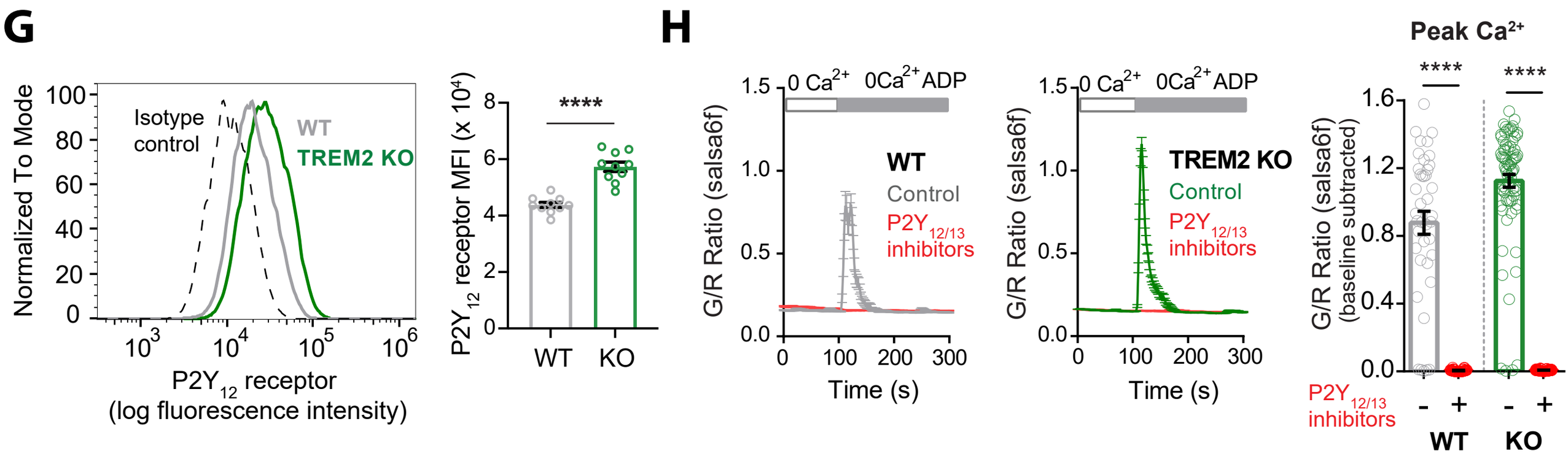

Figure 2-figure supplement 1

Figure 3

Figure 3-figure supplement 1

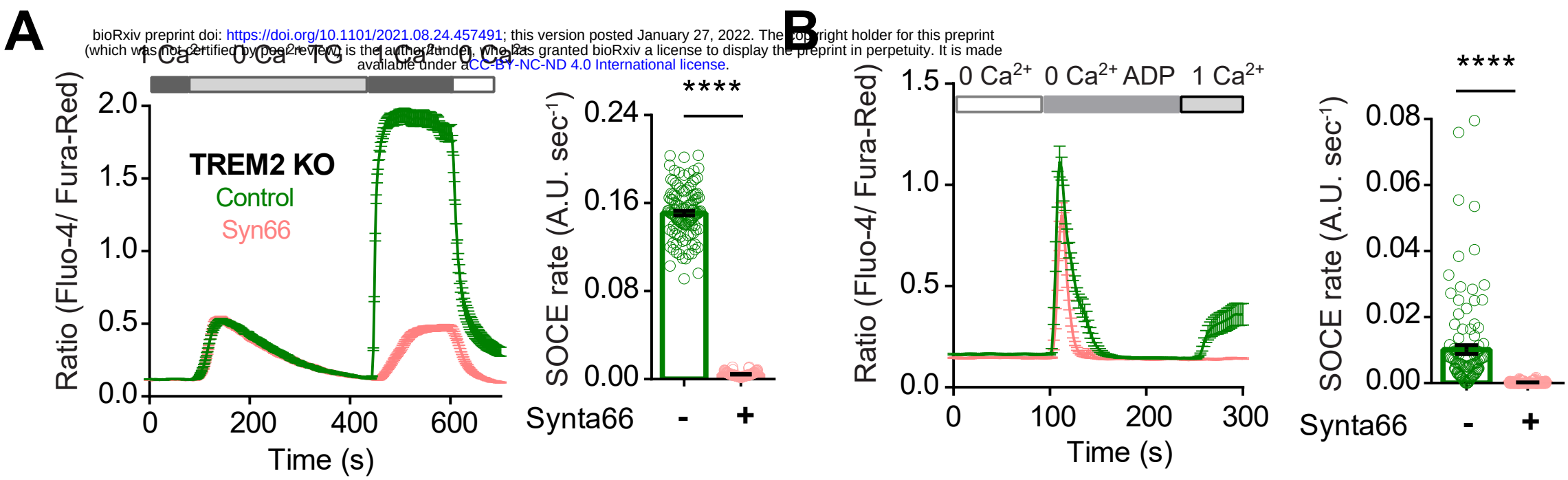

Figure 3-figure supplement 2

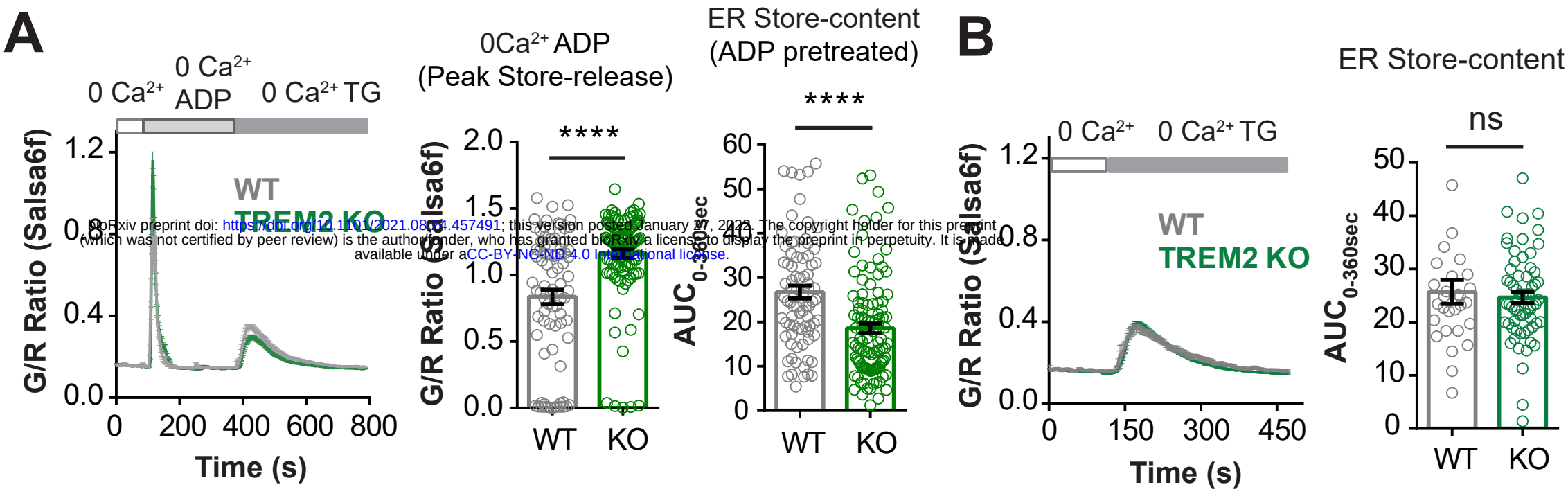

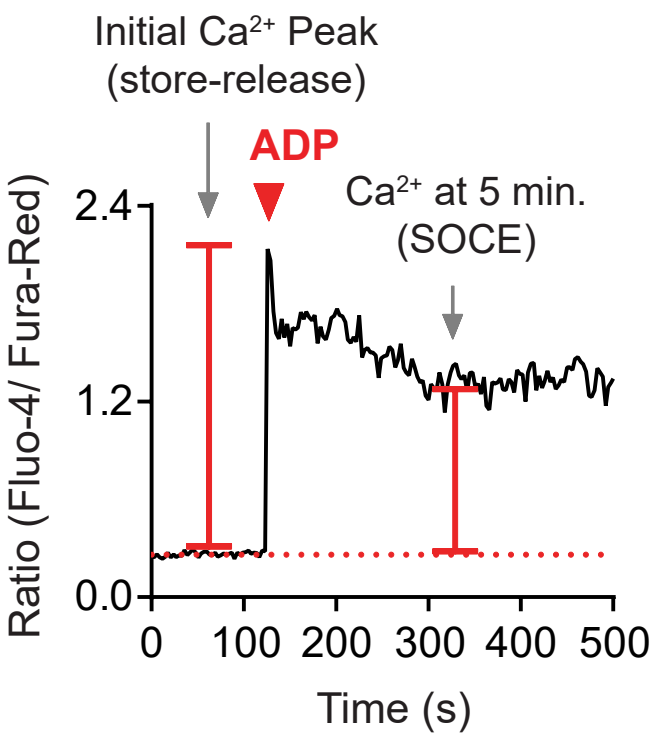

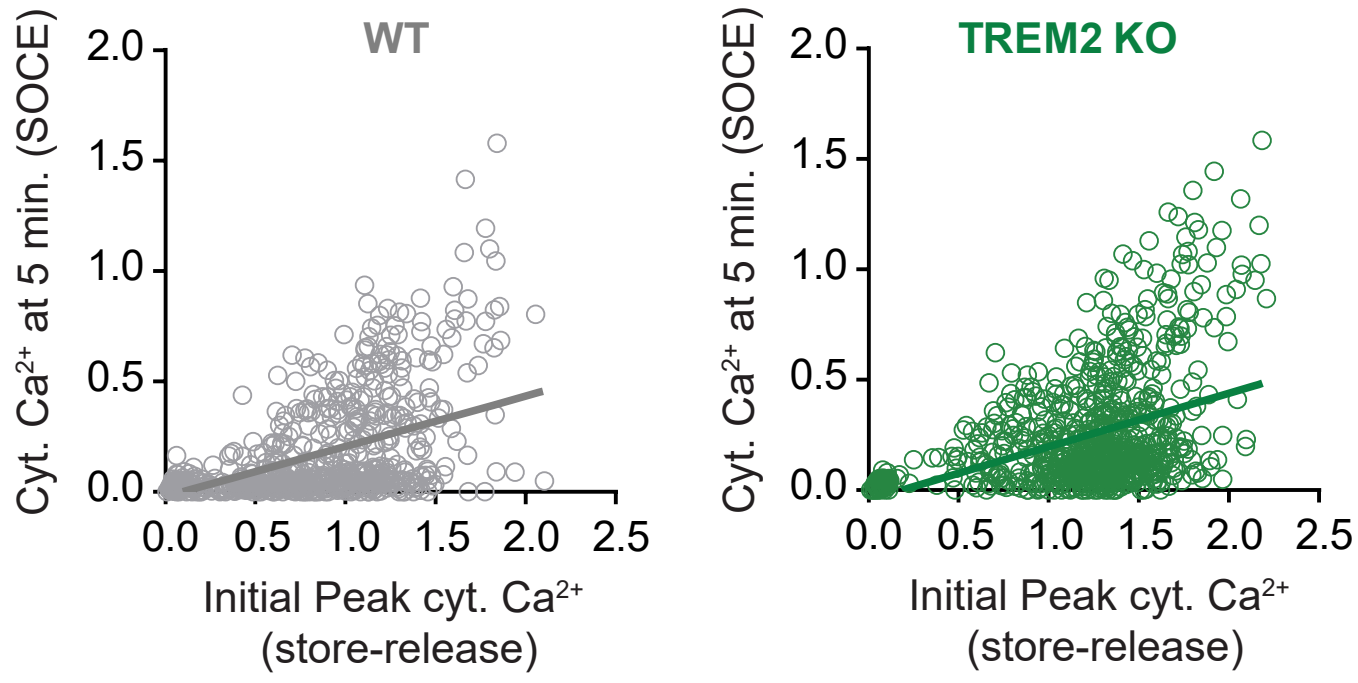

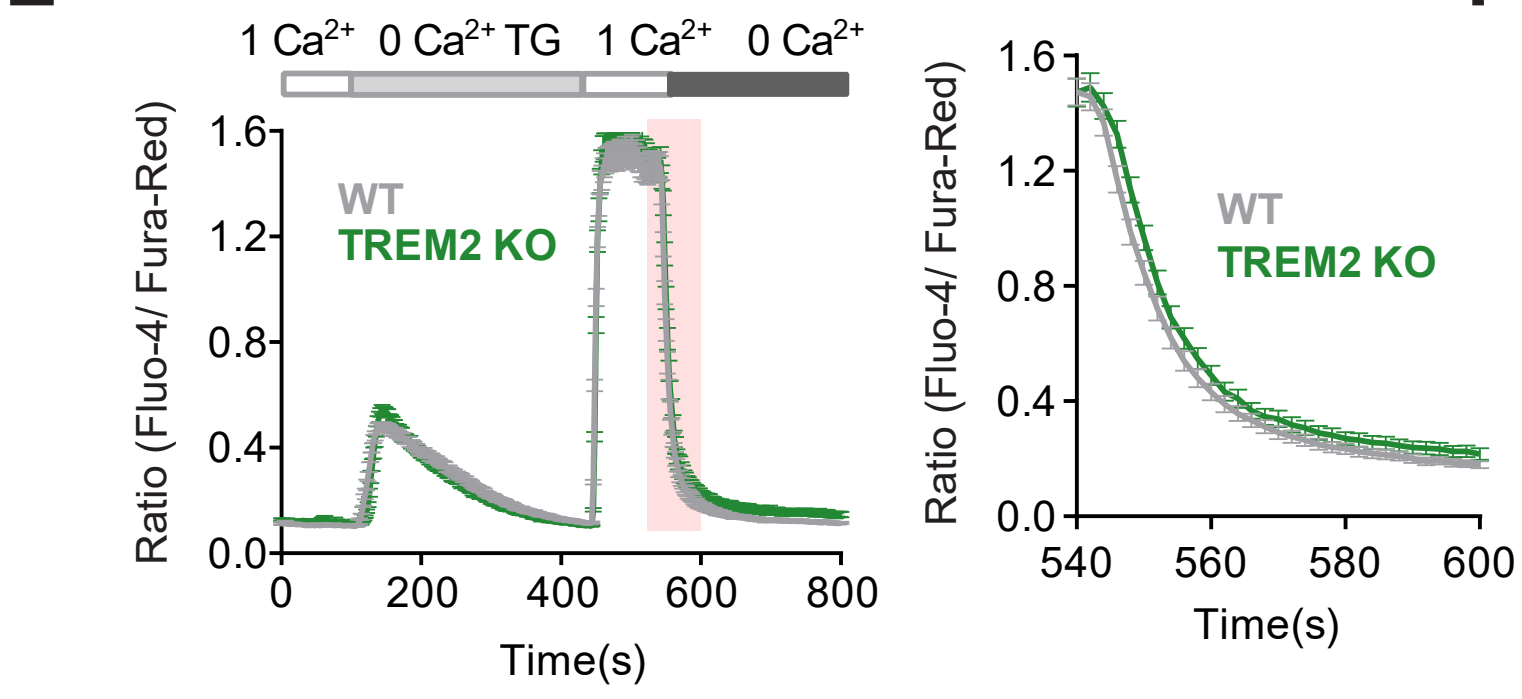

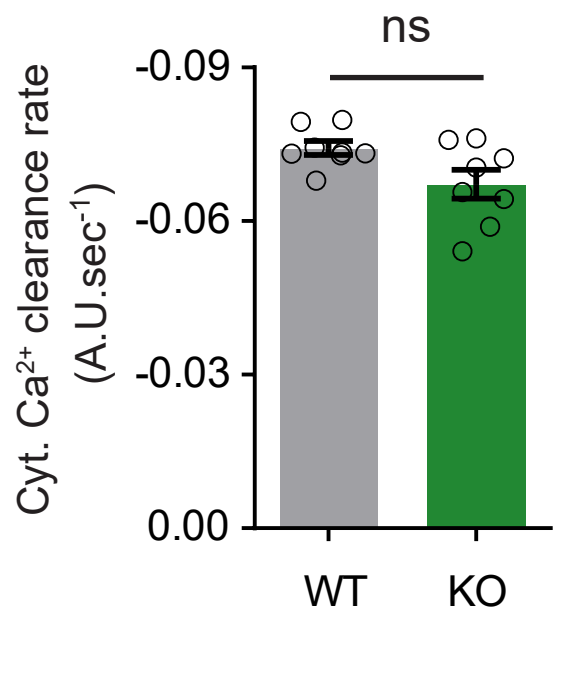

Figure 4

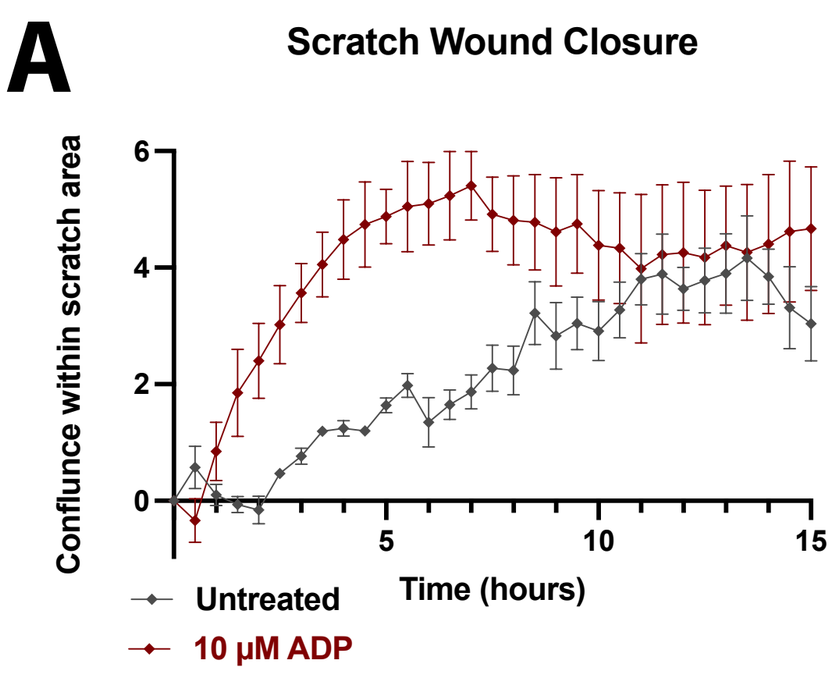

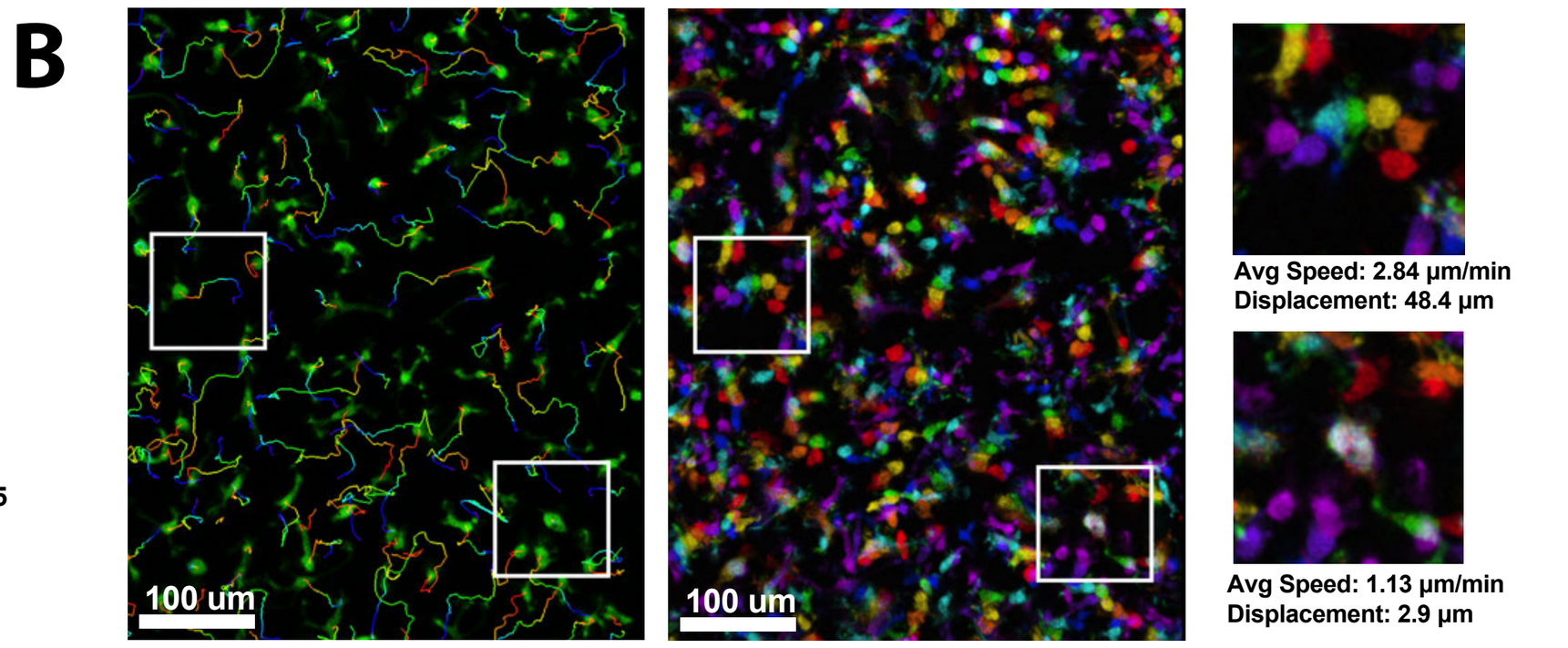

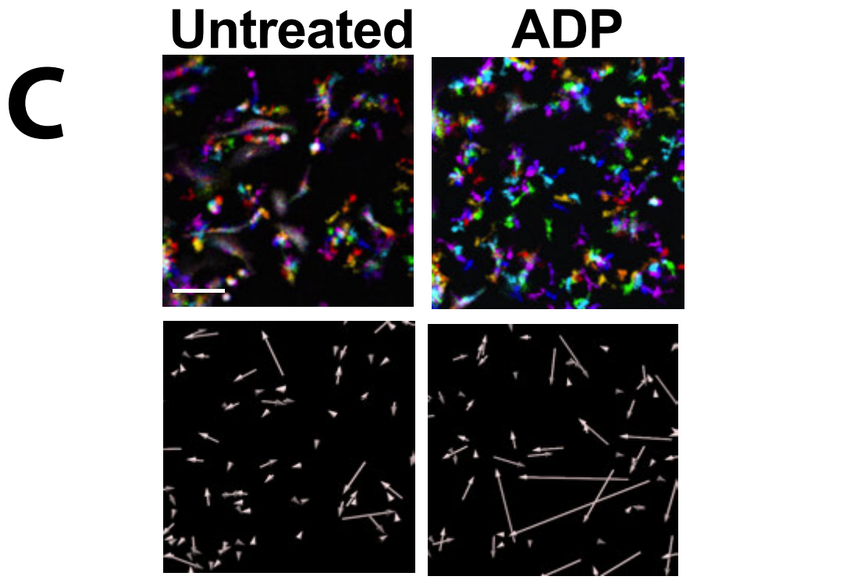

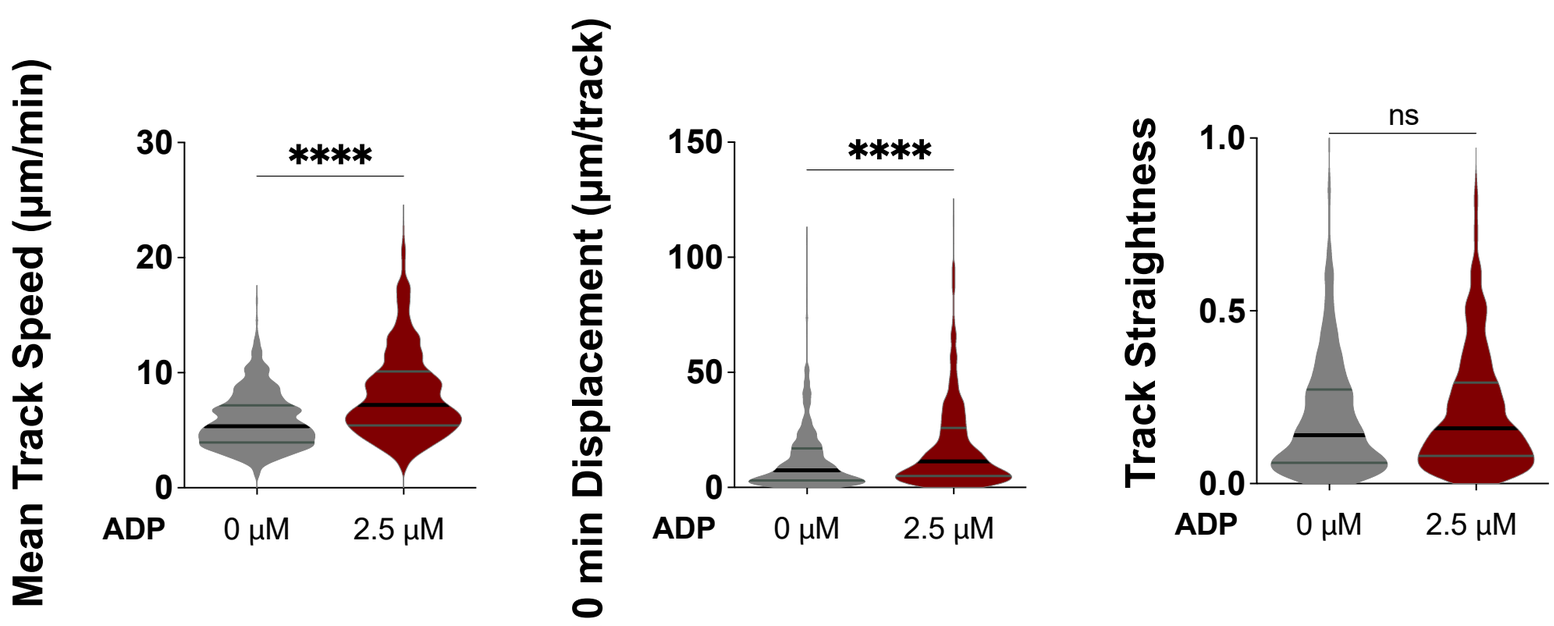

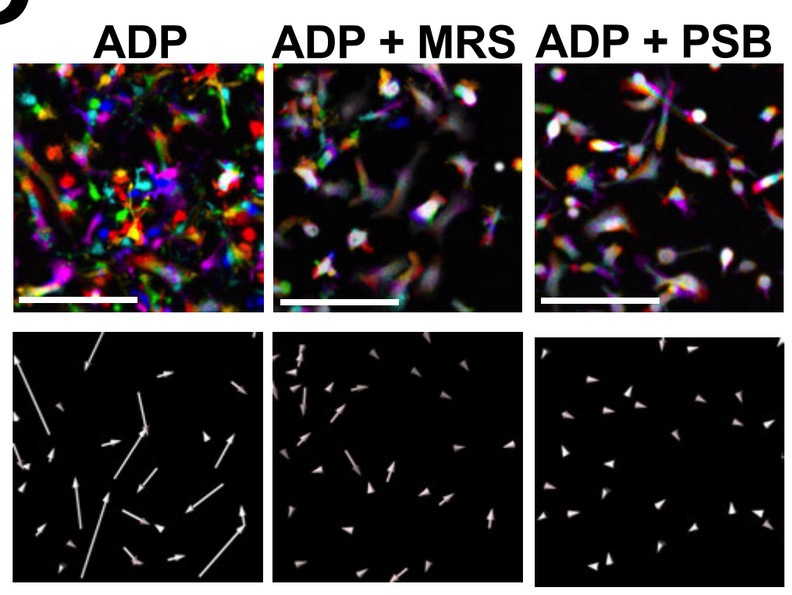

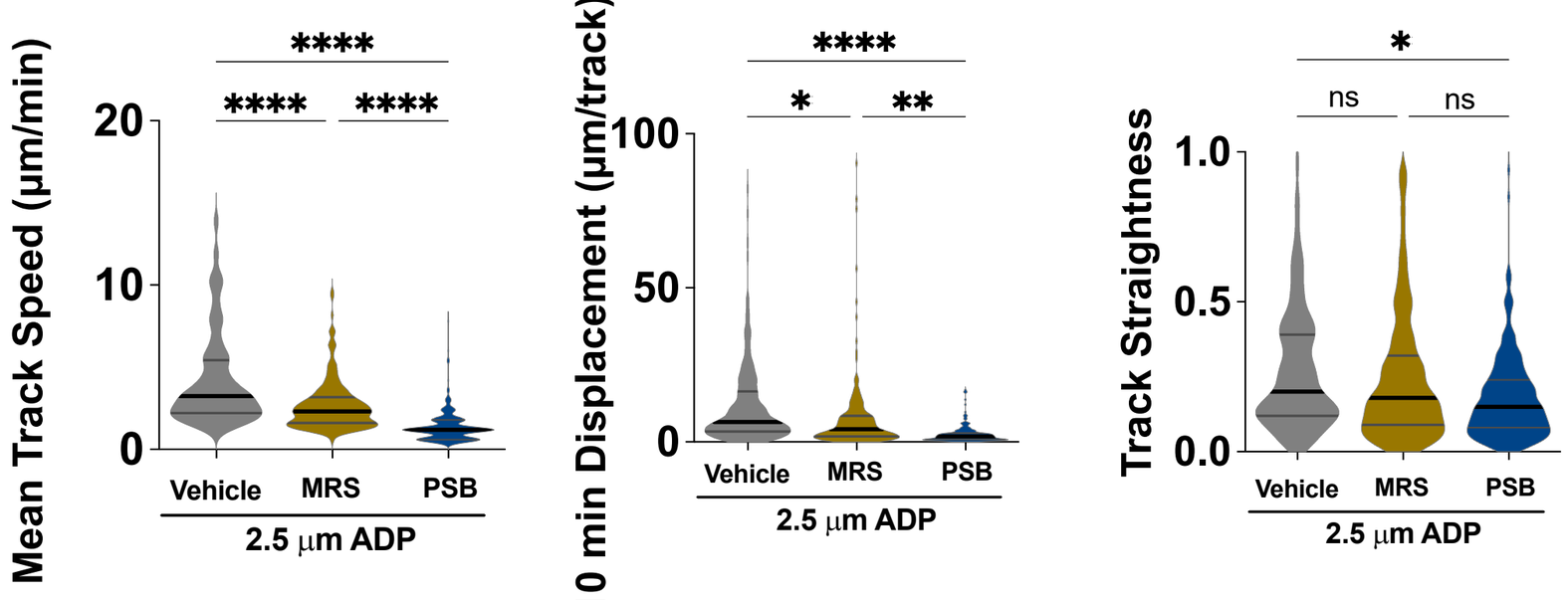

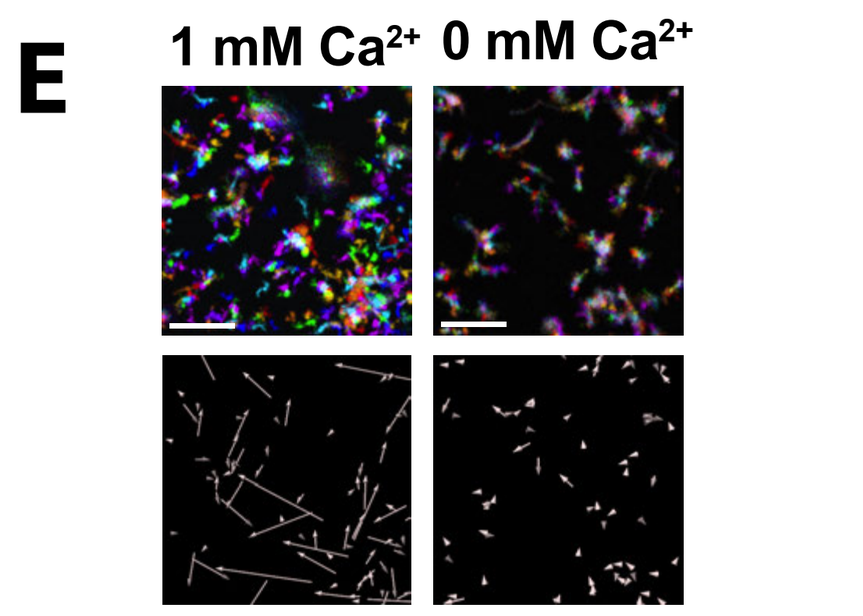

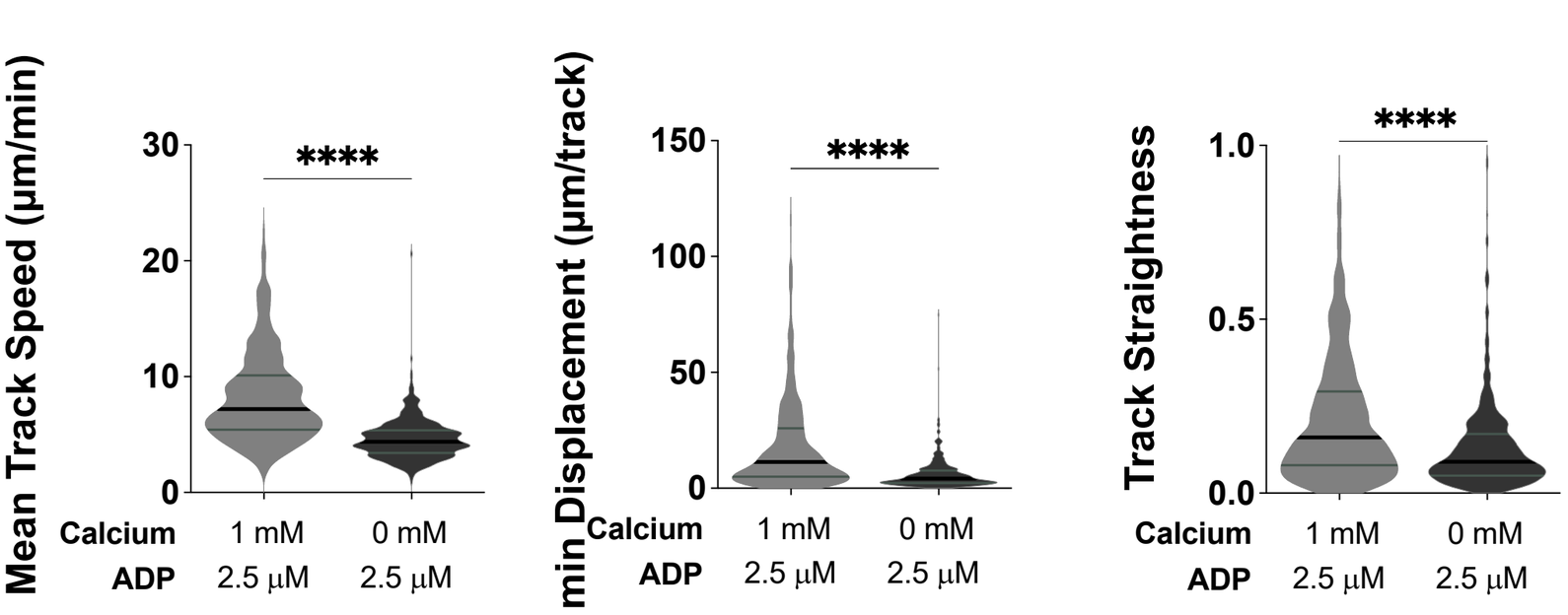

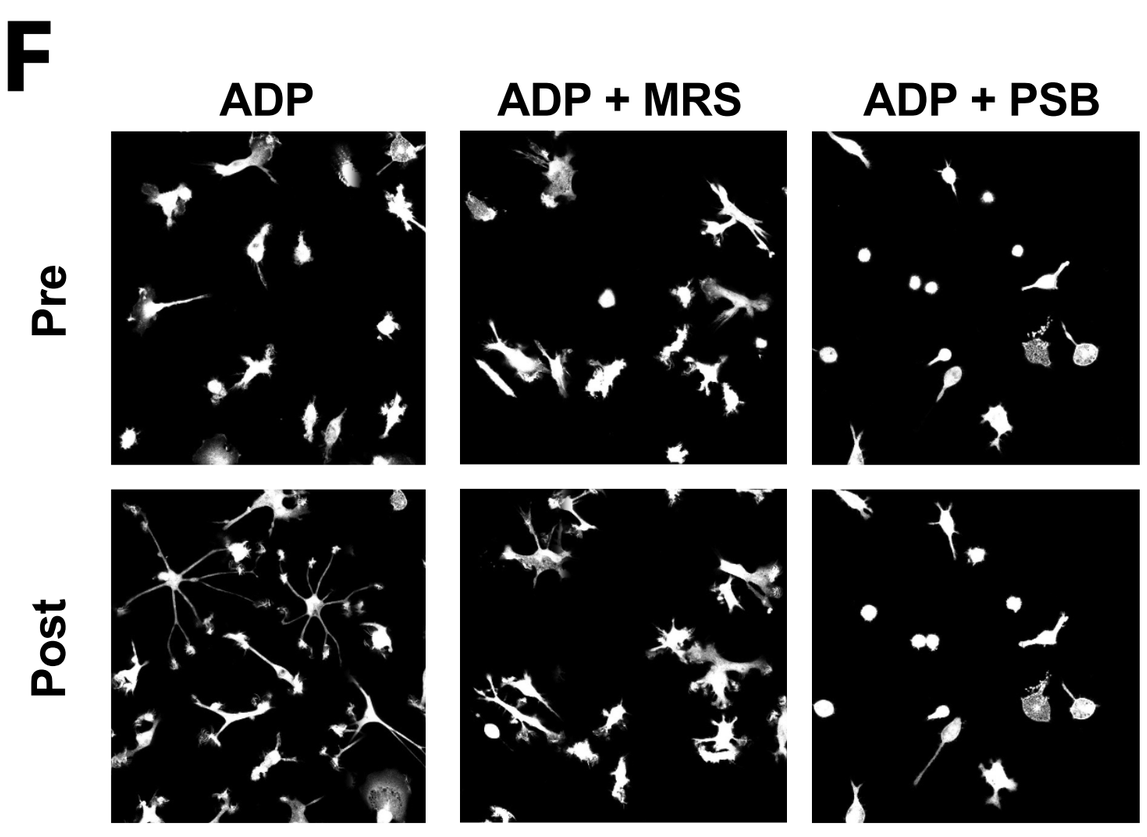

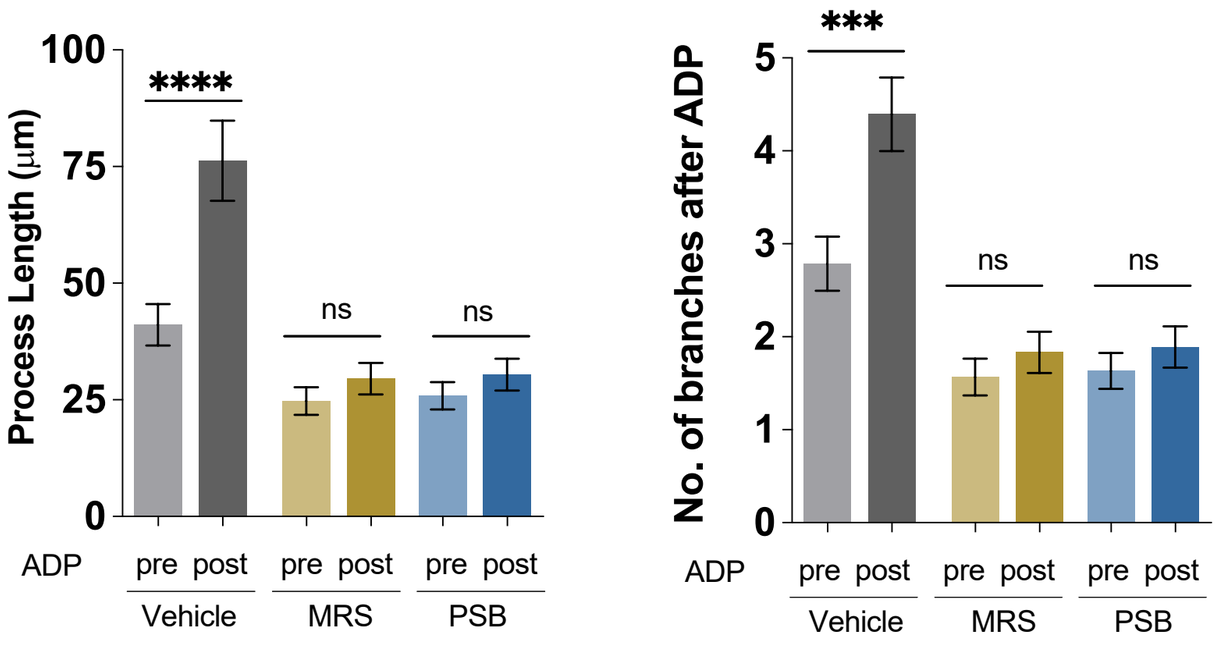

Figure 4- figure supplement 1

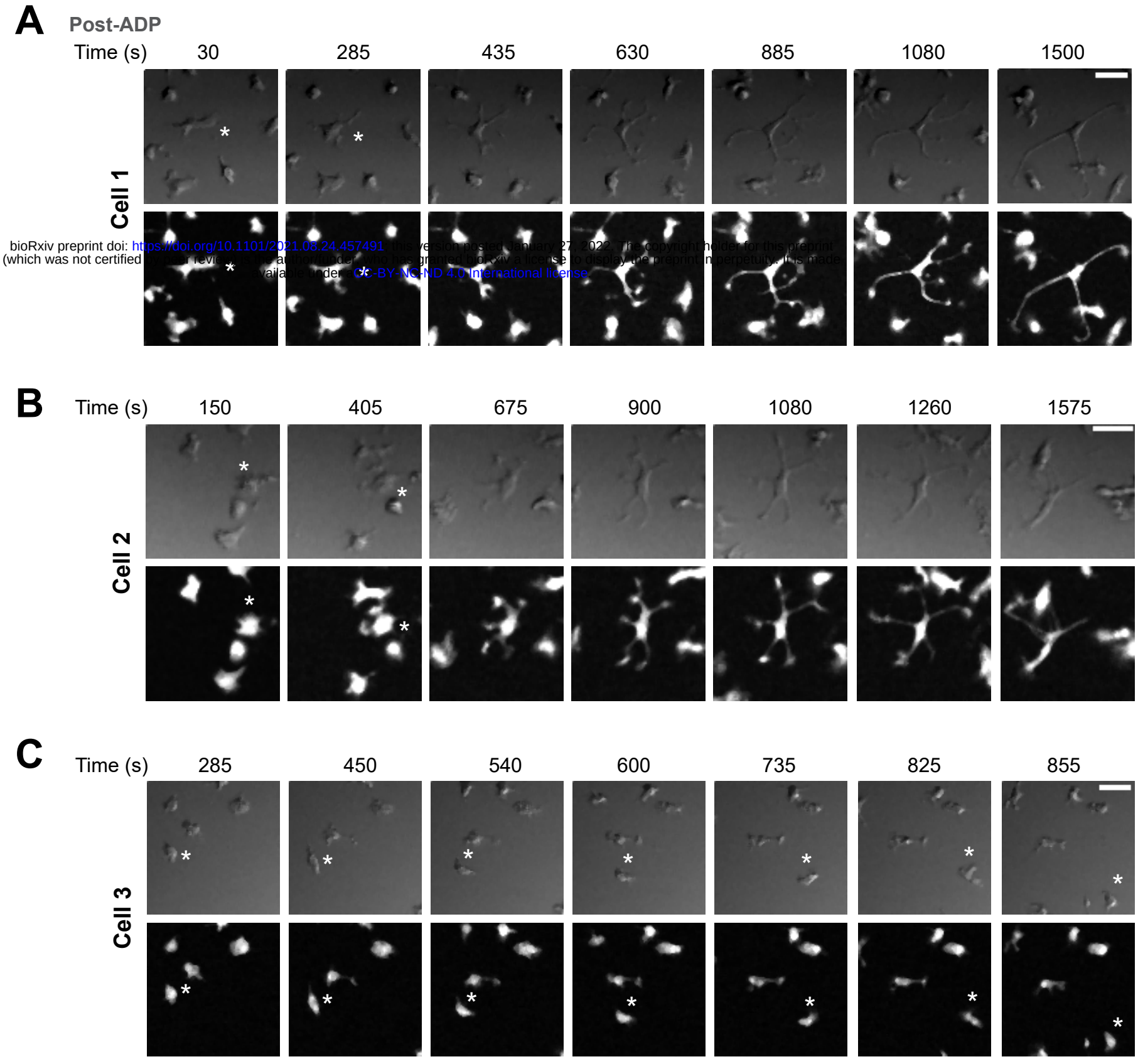

Figure 5

1 mM Calcium 2.5 µM ADP **Motility**

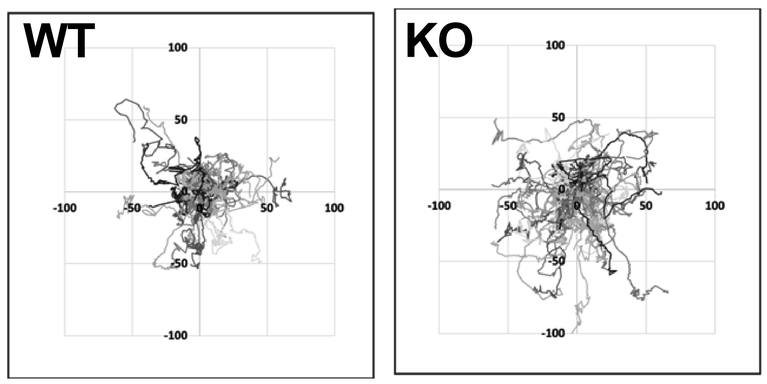

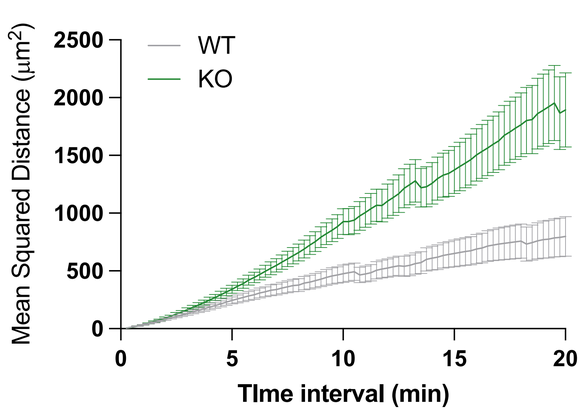

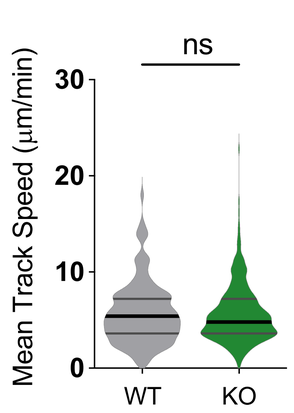

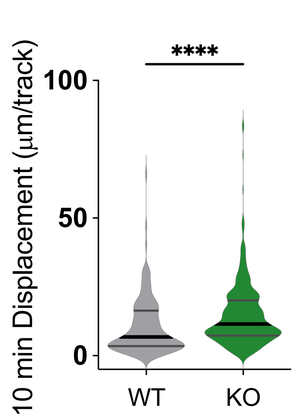

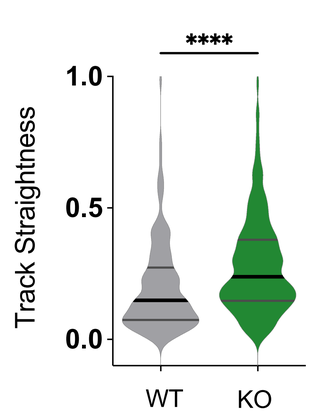

0 mM Calcium 2.5 µM ADP **Motility**

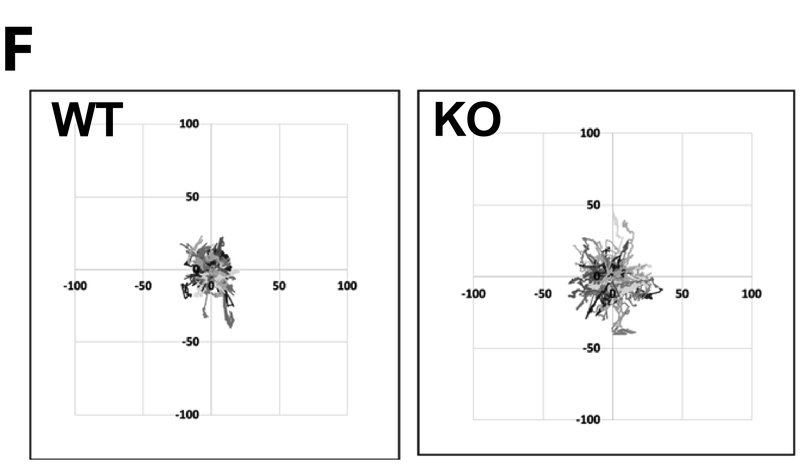

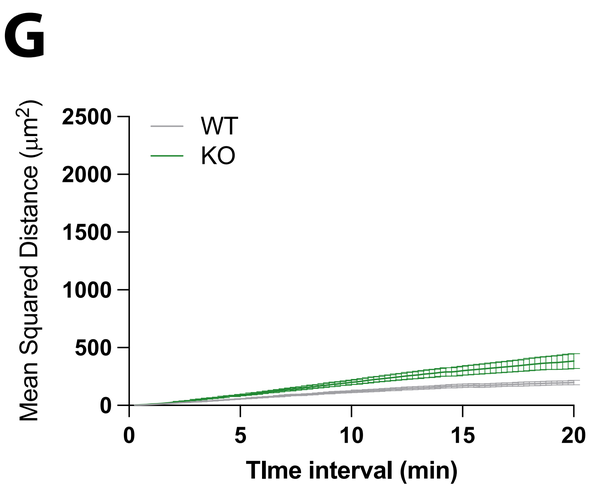

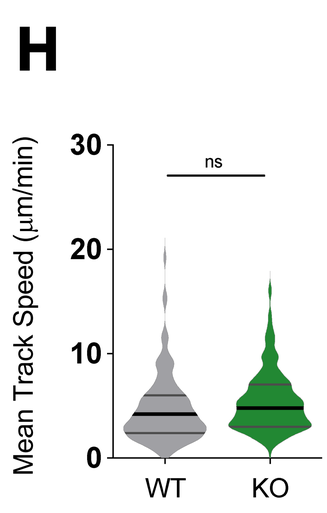

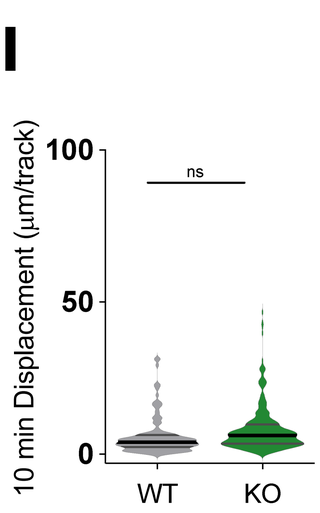

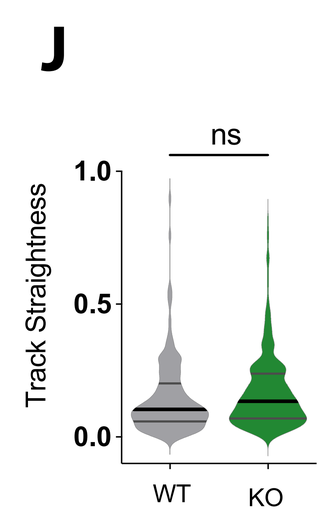

1 mM Calcium 2.5 µM ADP **Process Extension**

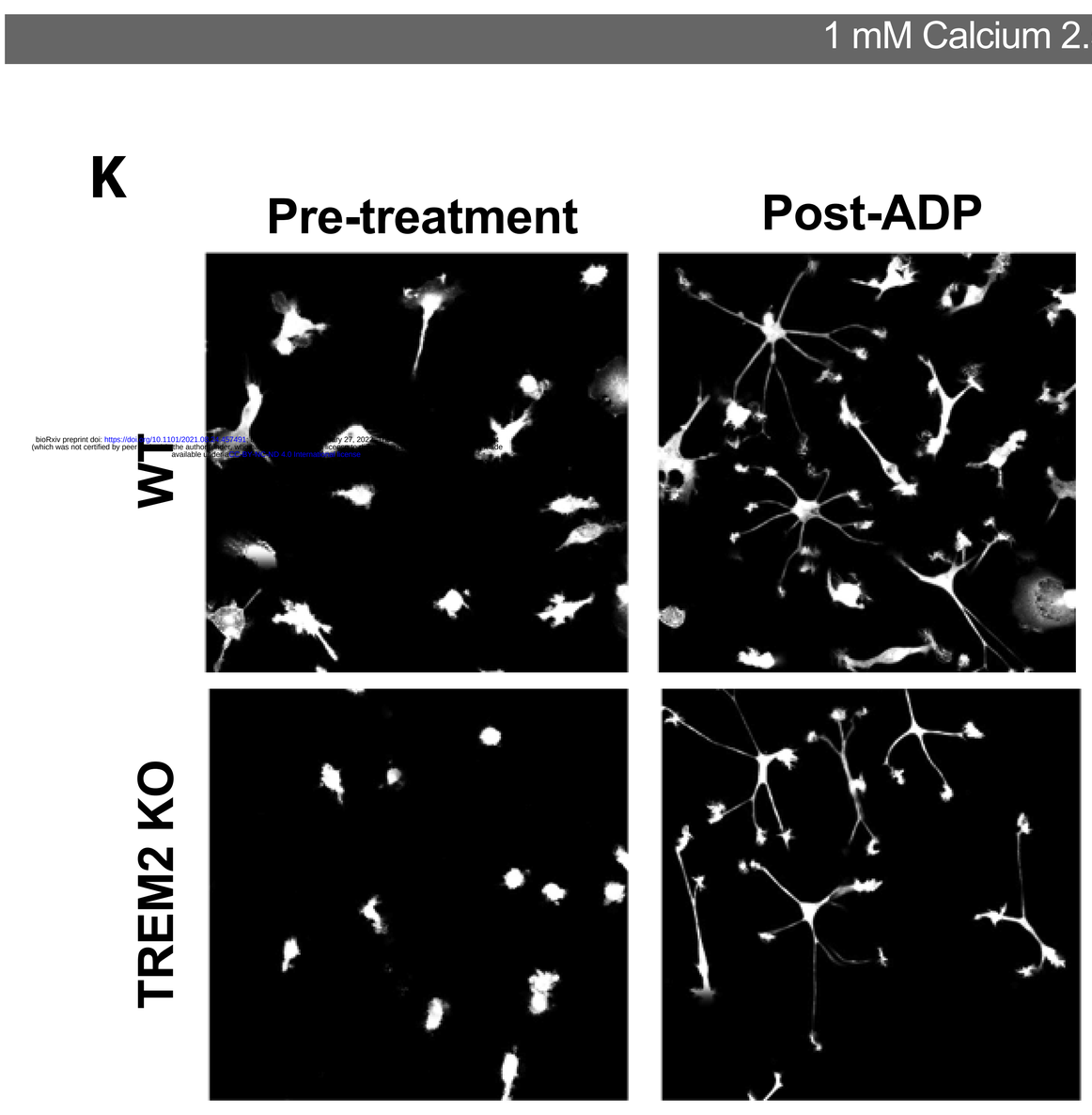

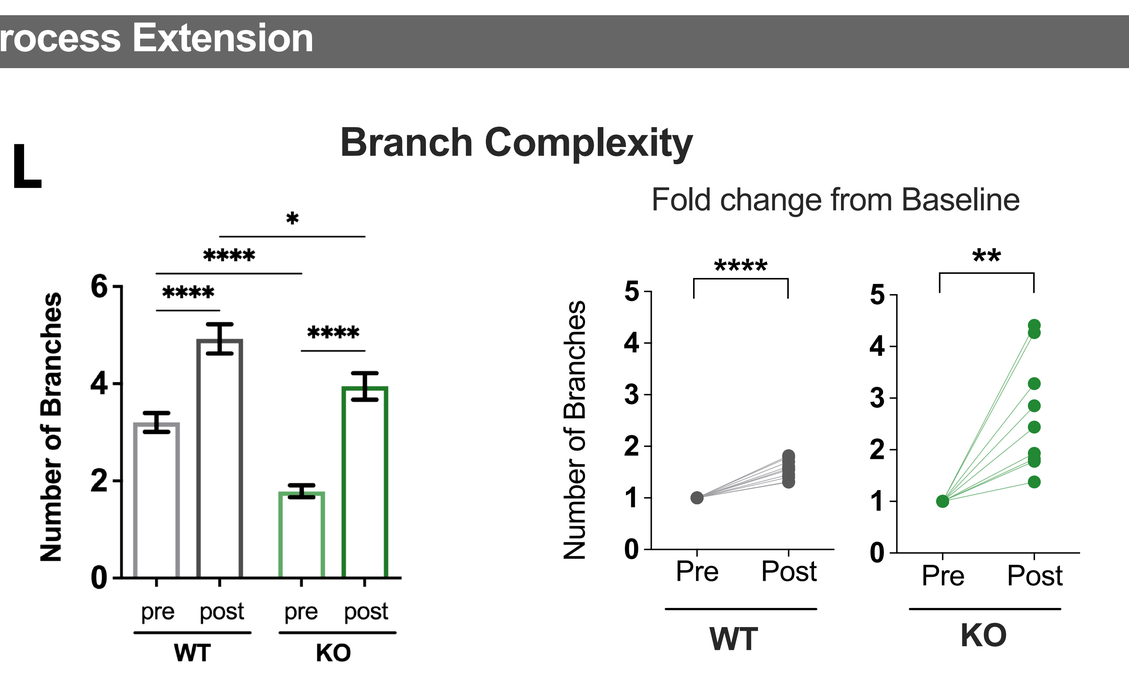

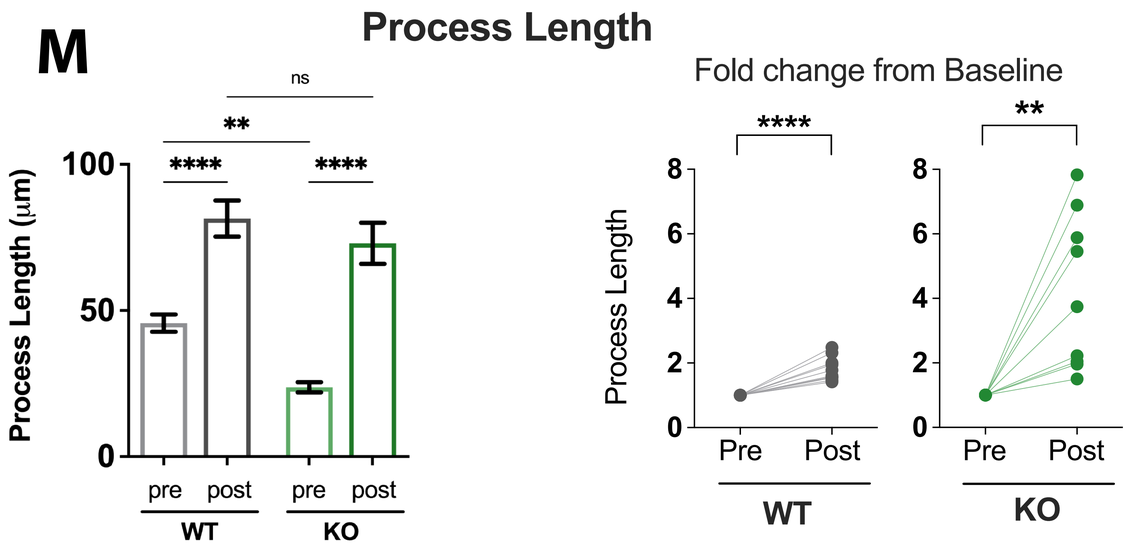

Figure 5-figure supplement 1

A

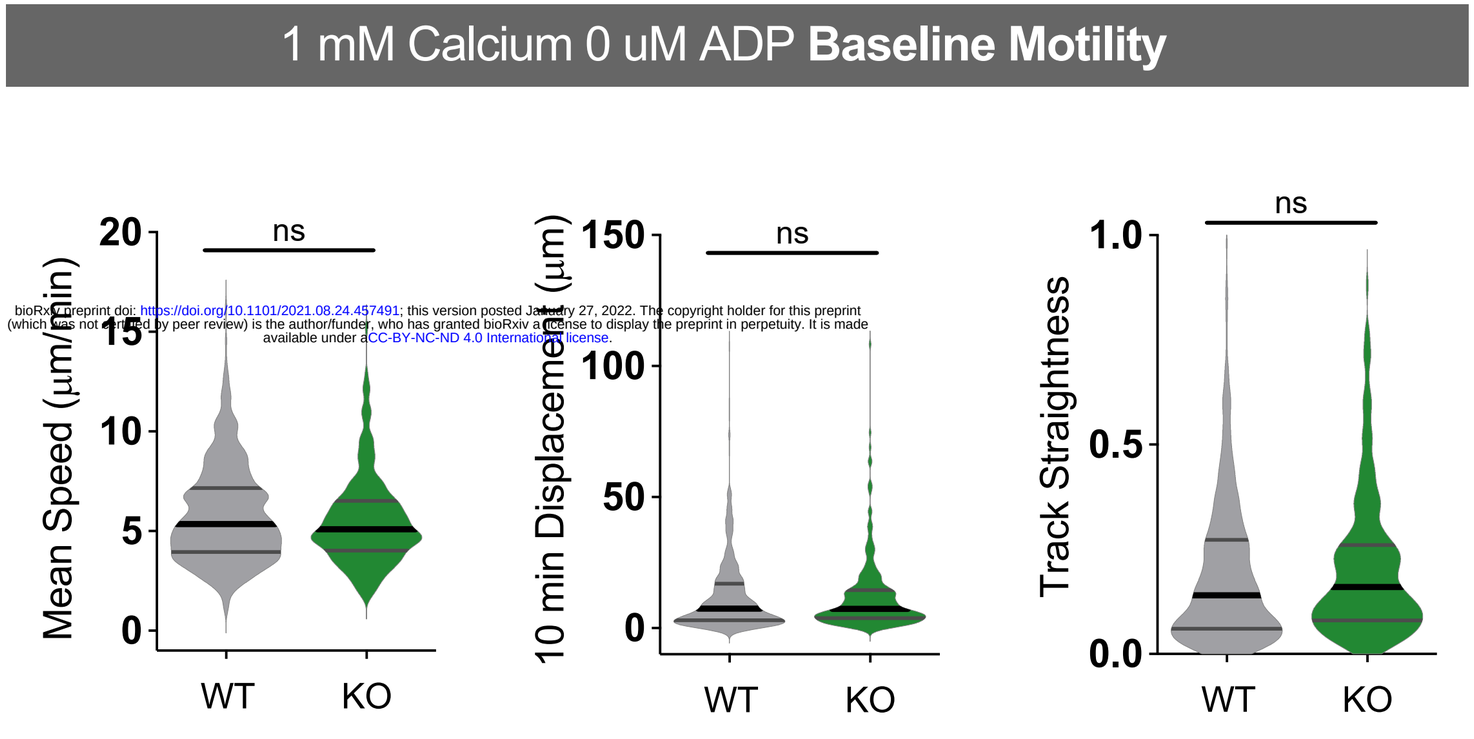

B

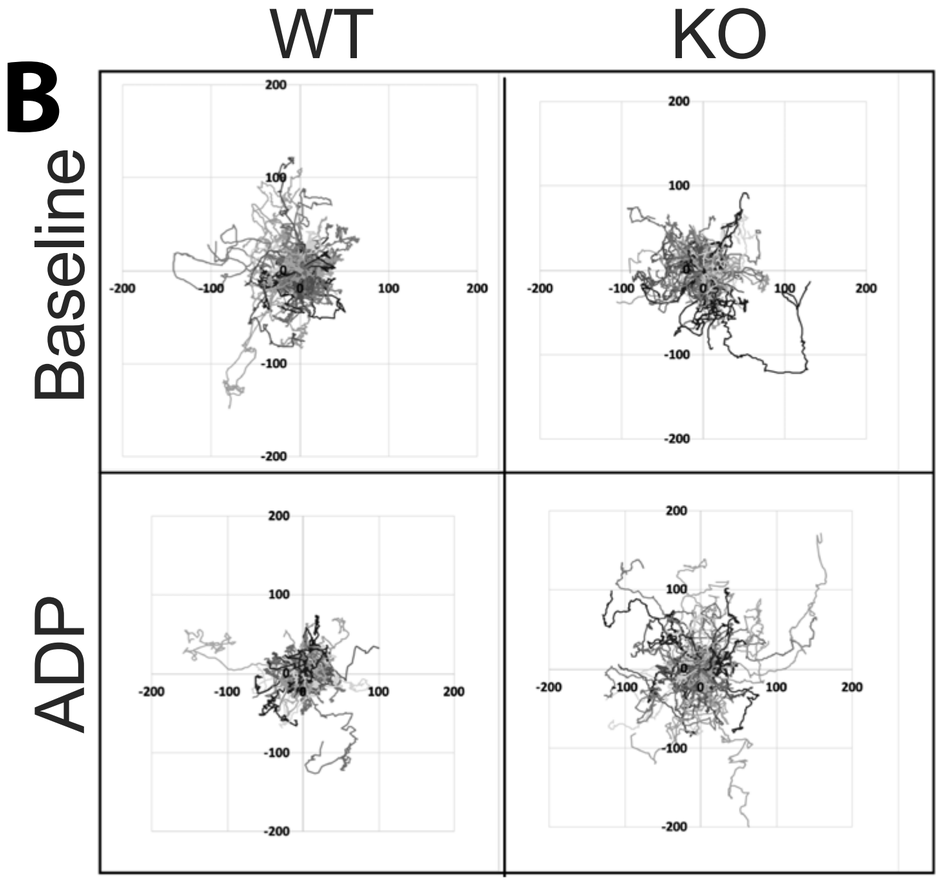

Directional Autocorrelation

C

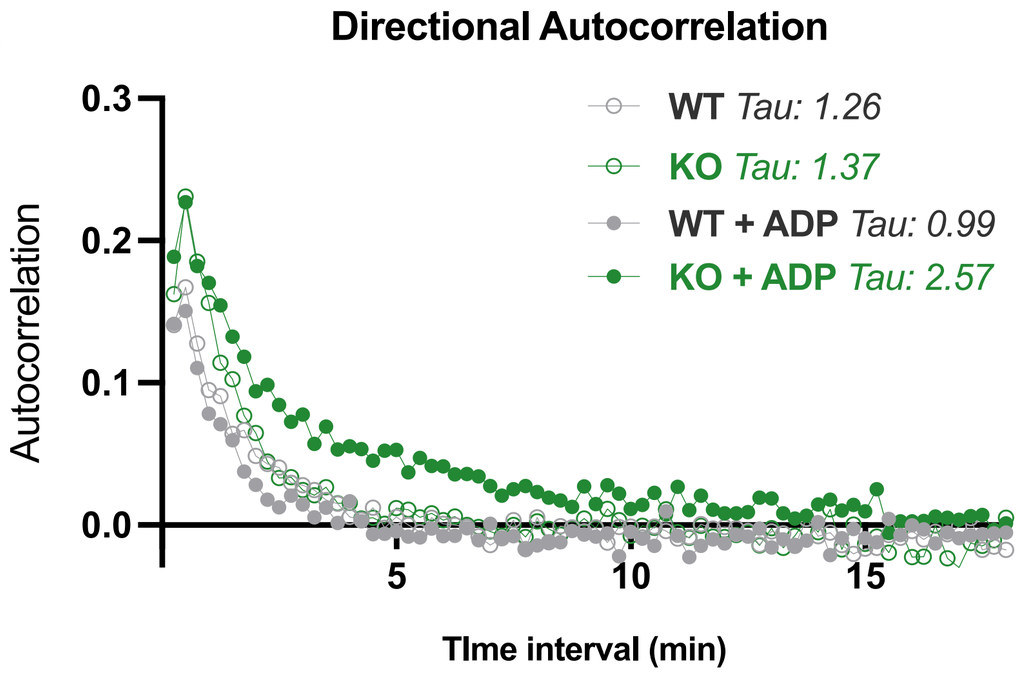

D

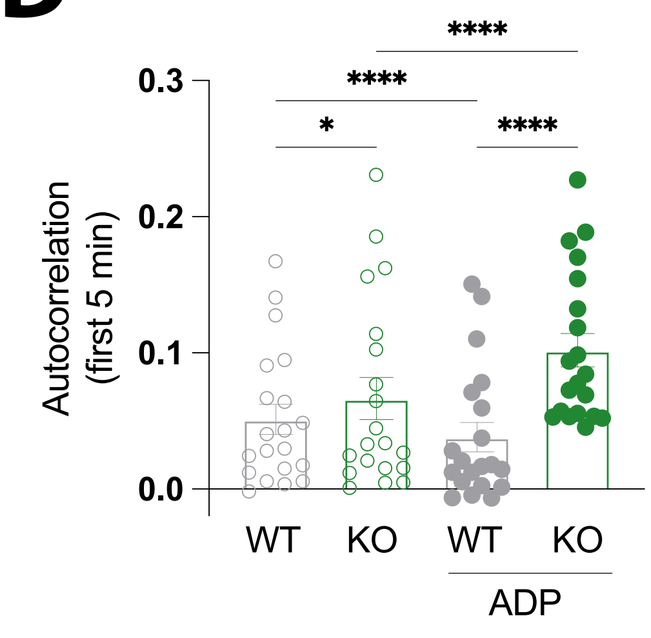

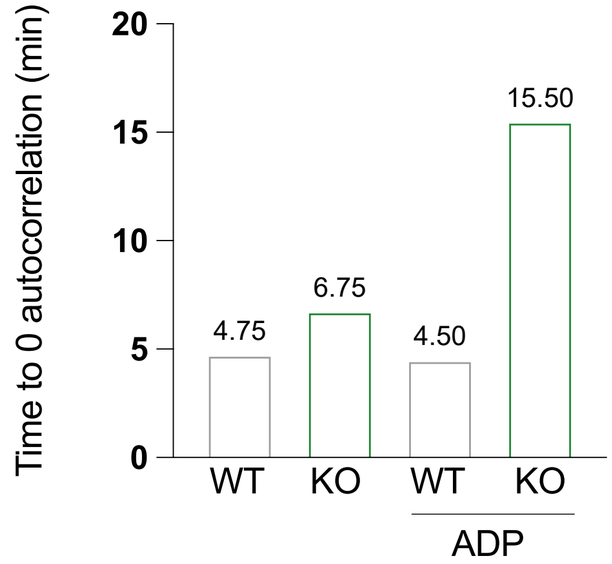

Figure 5-figure supplement 2

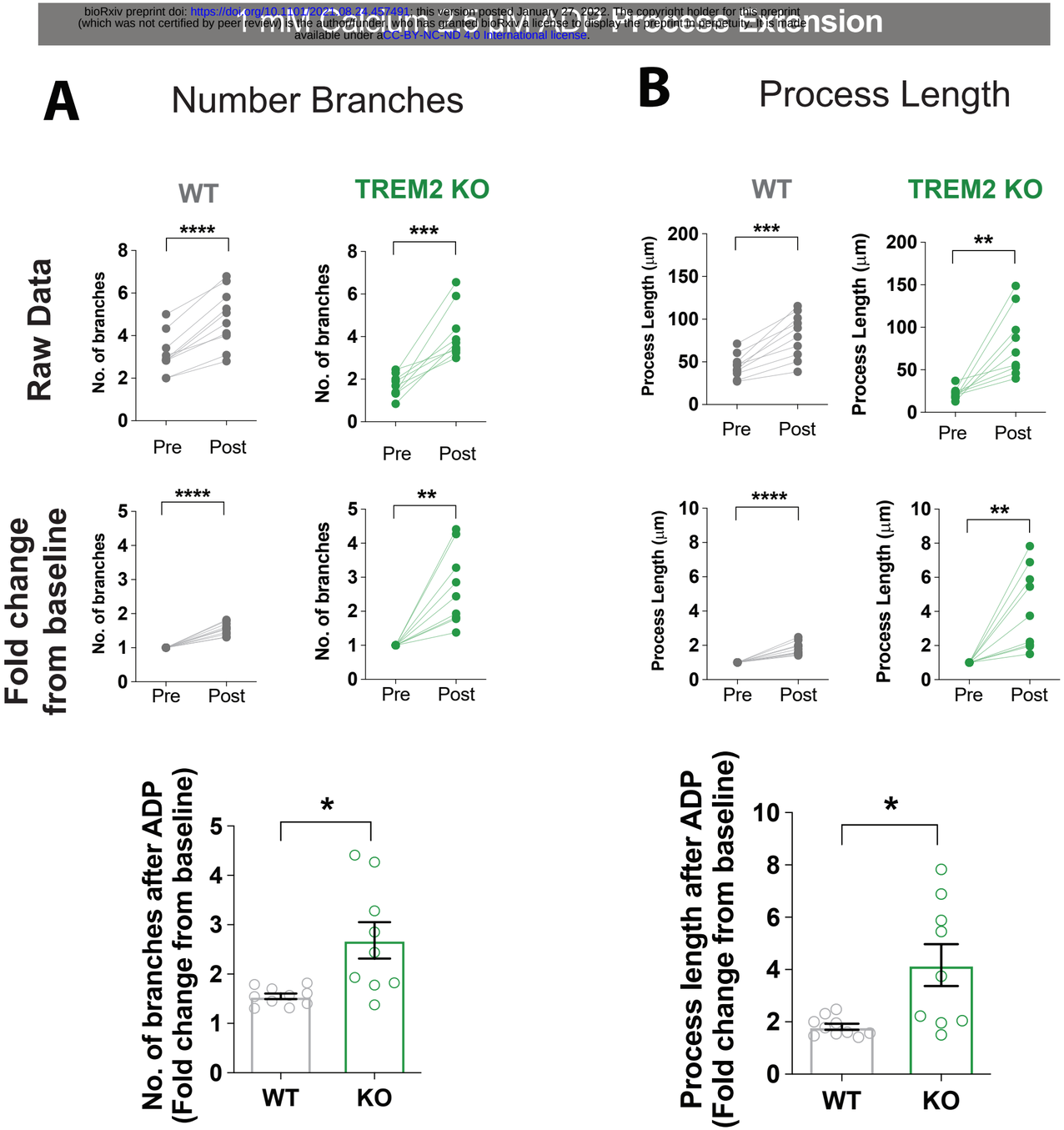

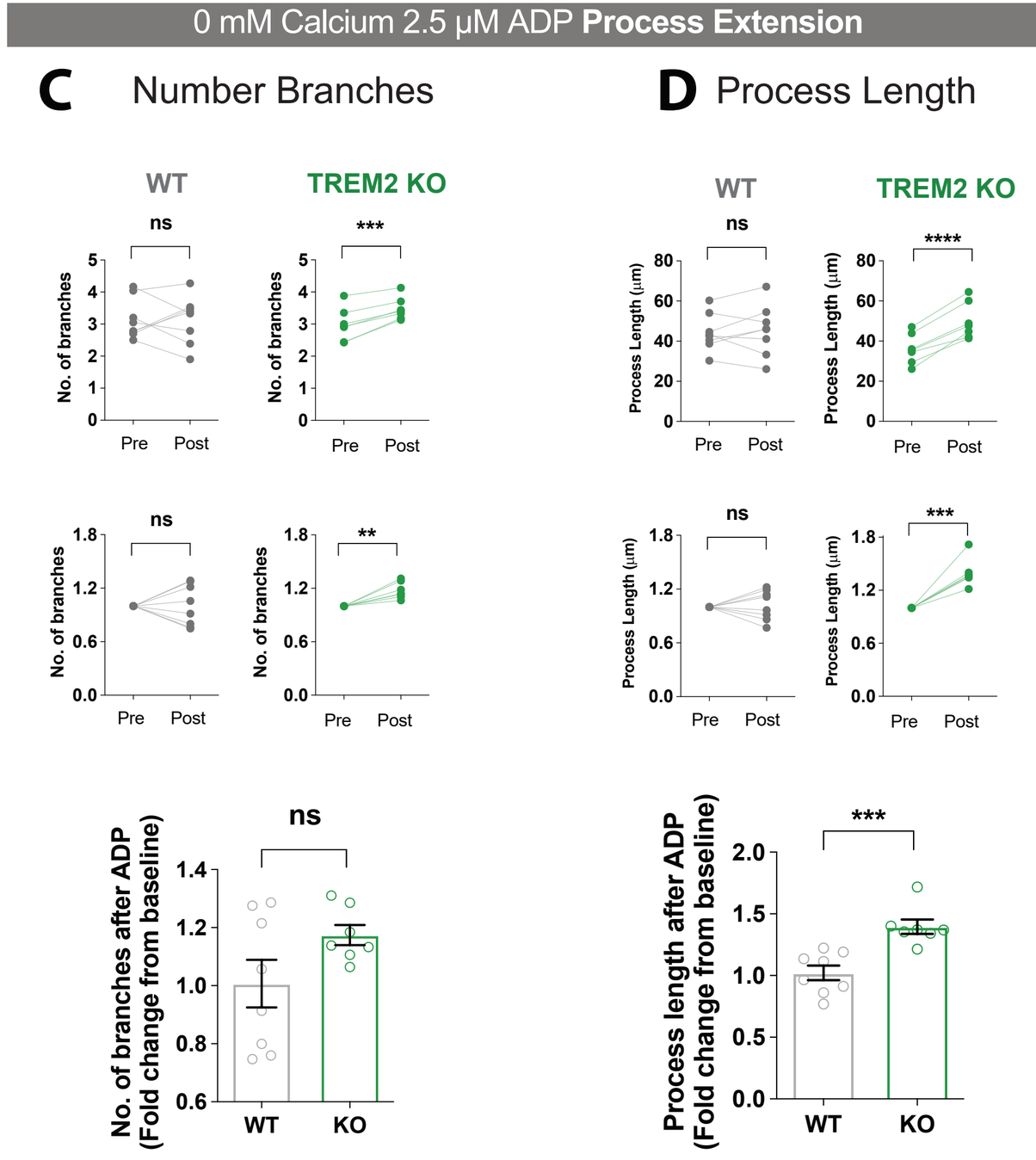

Figure 6

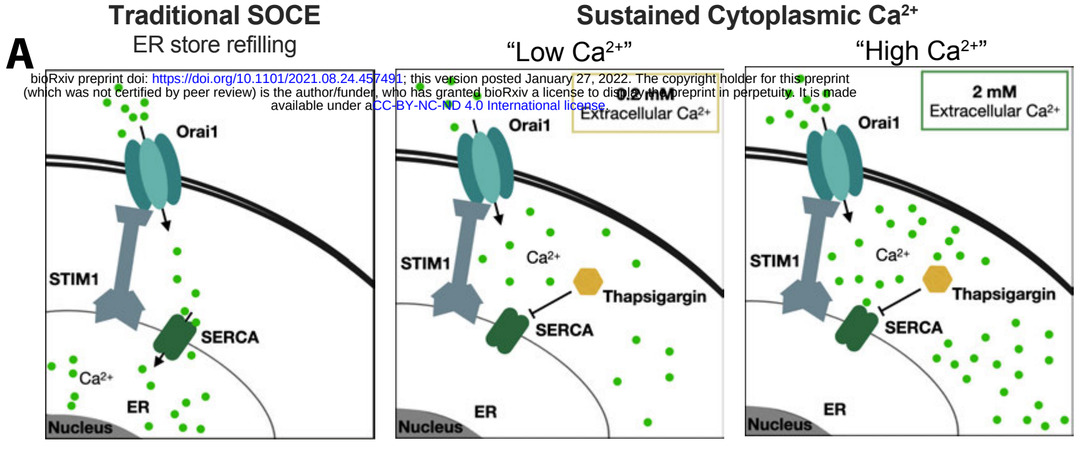

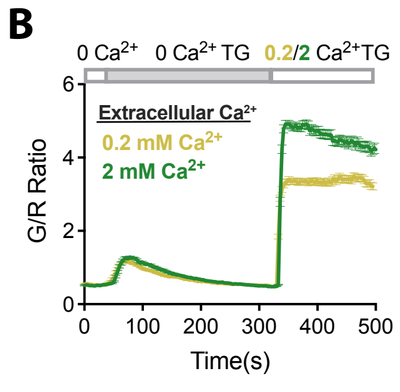

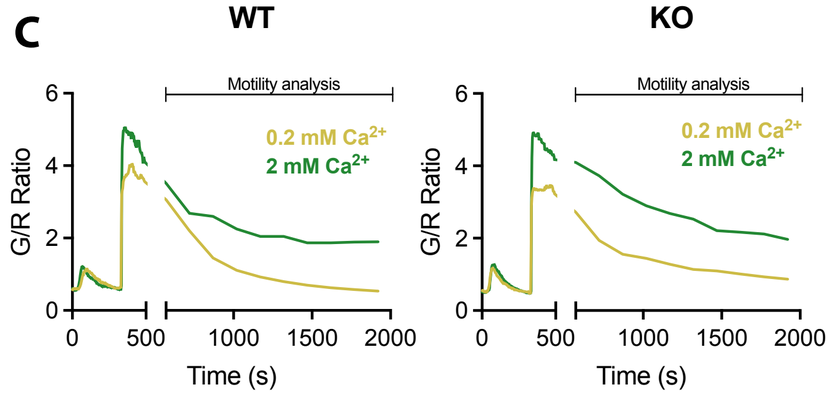

0.2 mM Calcium 0.2 µM Thapsigargin

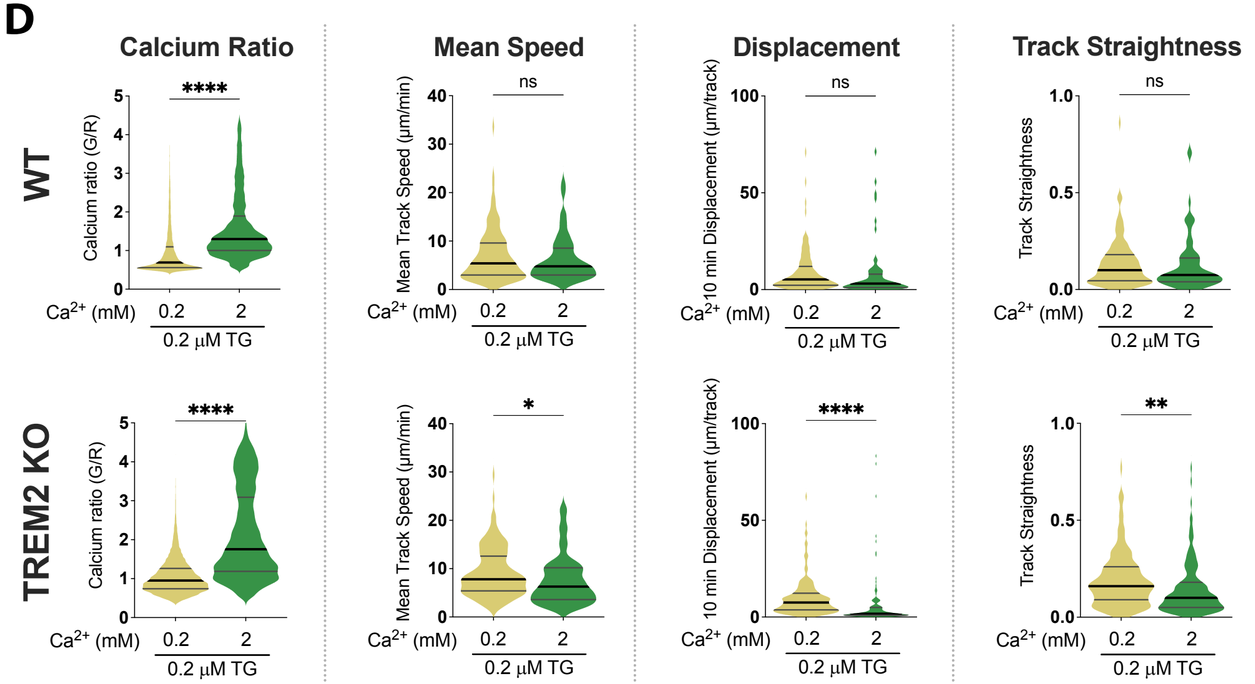

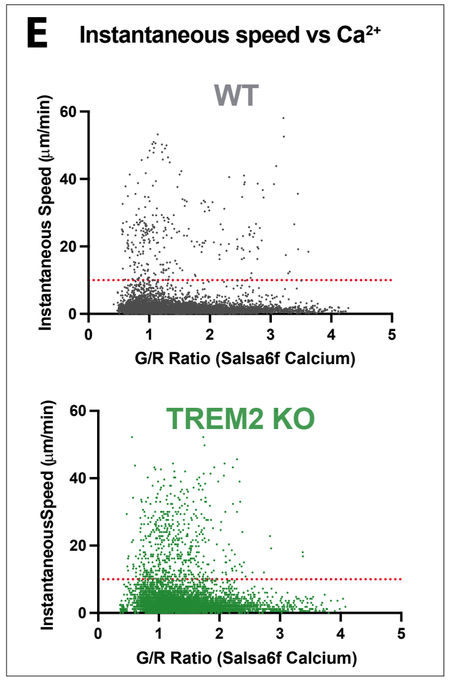

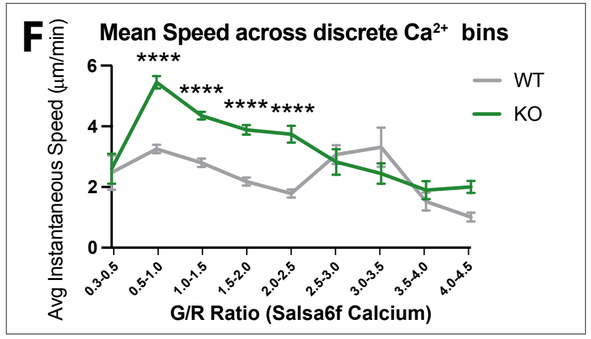

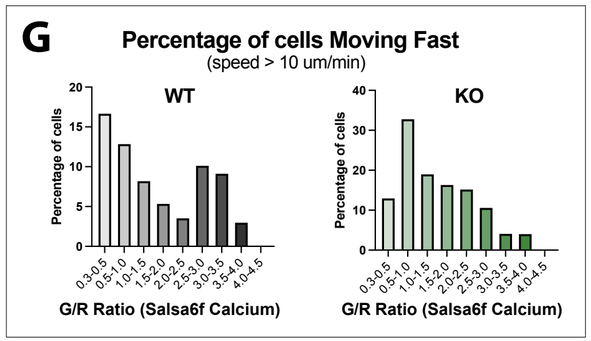

Figure 6-figure supplement 1

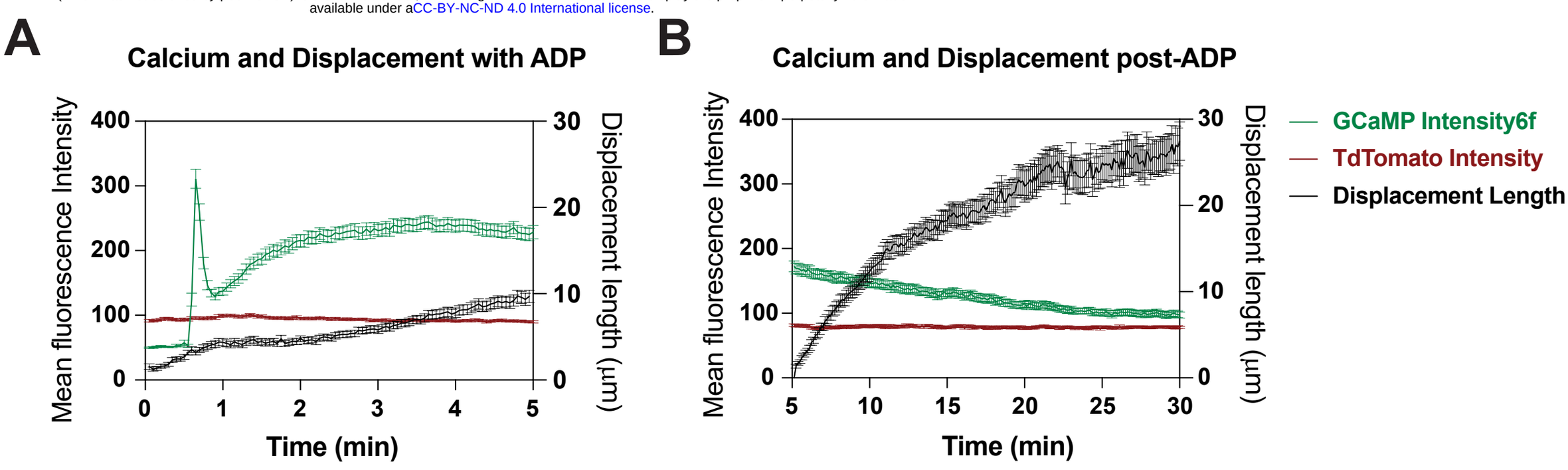

Figure 6-figure supplement 2

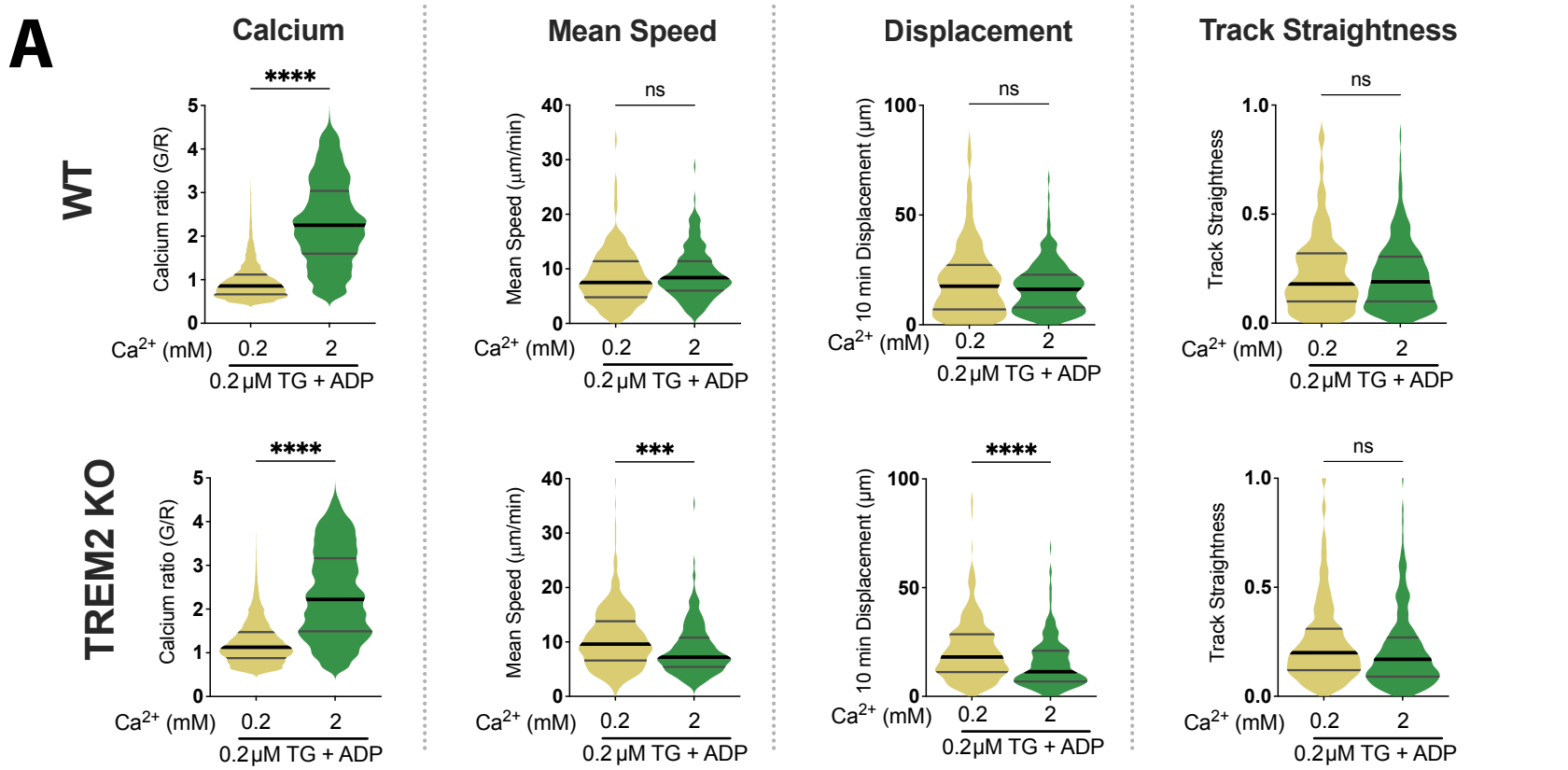

0.2 mM Calcium 0.2 μM Thapsigargin **Displacement**

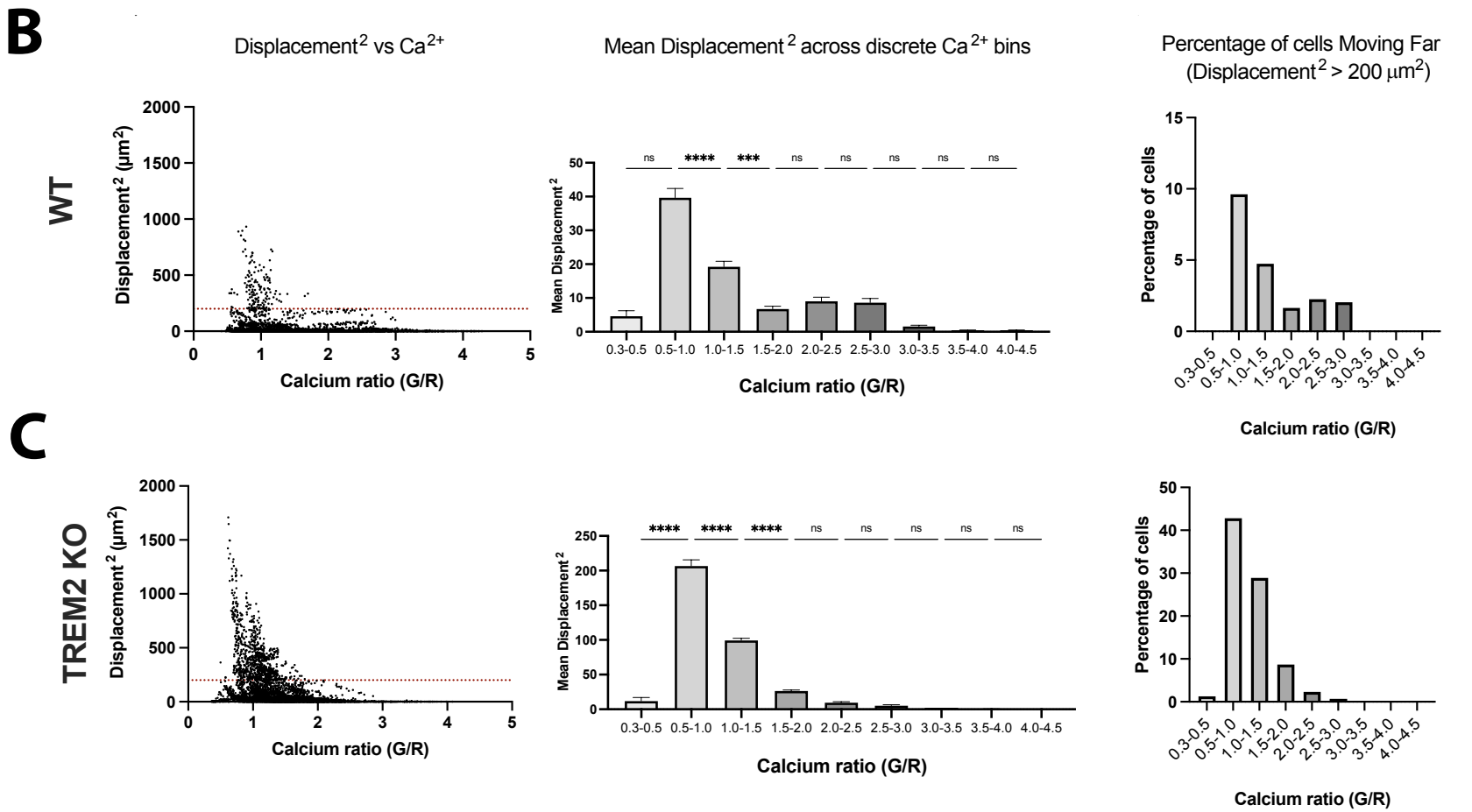

Figure 7

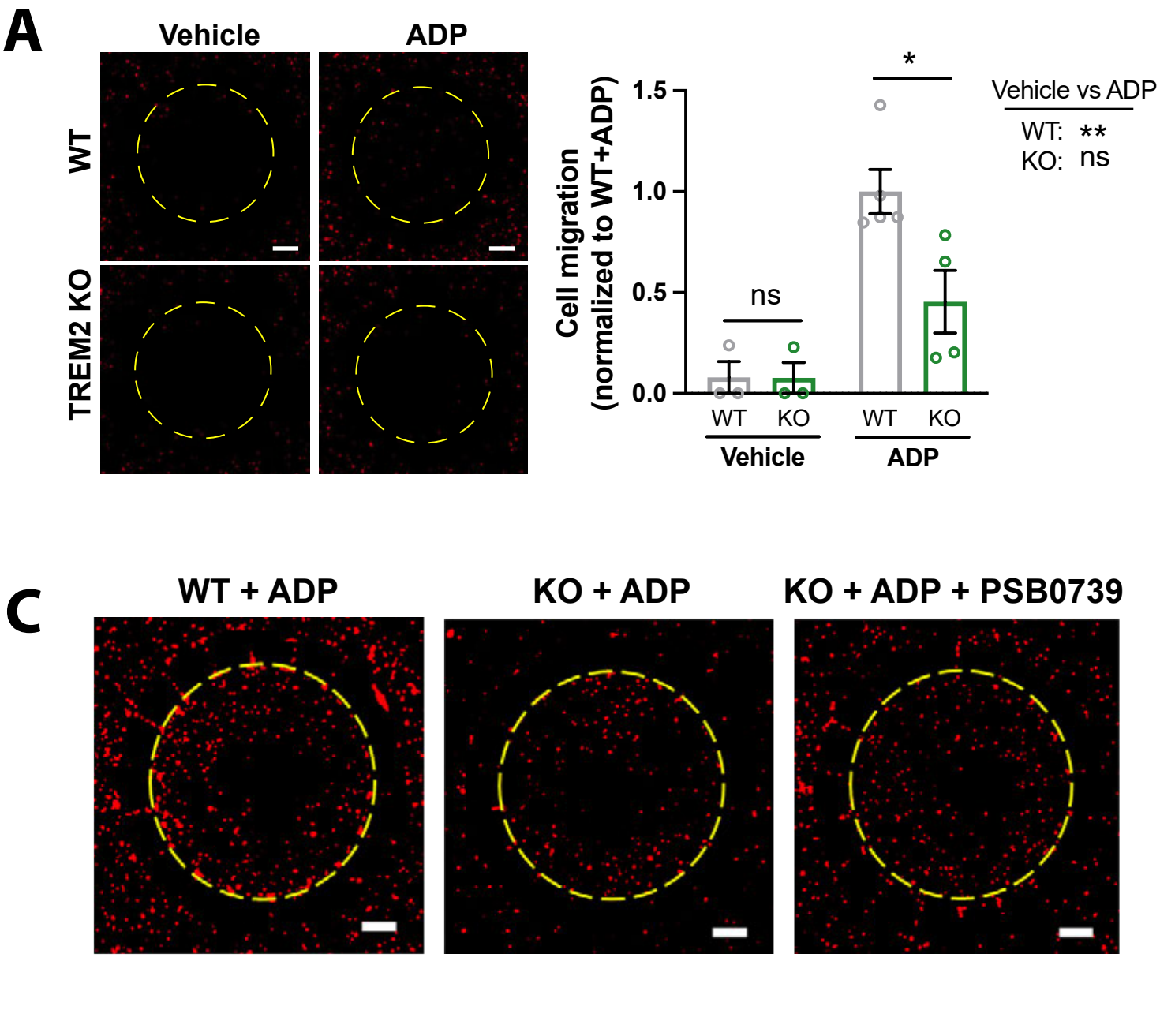
A
Vehicle
ADP
WT
TREM2 KO
Cell migration (normalized to WT+ADP)
1.5
1.0
0.5
0.0
*
ns
Vehicle vs ADP
WT: **
KO: ns
WT
KO
WT
KO
Vehicle
ADP
B
****
****
****
Fluo-4/ Fura-Red Ratio (Peak - Baseline)
2
1
0
WT
KO
KO
ADP + + +
PSB 0739 - - +
C
WT + ADP
KO + ADP
KO + ADP + PSB0739
ns
*
**
Cell migration (normalized to WT+ADP)
1.5
1.0
0.5
0.0
WT
KO
KO
ADP + + +
PSB 0739 - - +

Figure 7-figure supplement 1